

Modeling of intraplate strike slip faulting and
shear zone evolution in the lower crust based on
nonlinear rheological laws

非線形流動則に基づく内陸横ずれ断層運動と下部地殻剪断帯発達
のモデル化

張 学磊
(ZHANG, Xuelei)

A dissertation for the degree of Doctor of Science
Department of Earth and Environmental Sciences,
Graduate School of Environmental Studies, Nagoya University

(名古屋大学大学院 環境学研究科 地球環境科学専攻 学位論文 博士(理学))

January 2019

Abstract

Intraplate earthquakes occurring at active faults are highly hazardous. But physical mechanisms of their occurrences are still not well understood. In order to tackle this problem, I investigate mechanical processes regarding tectonic loading of intraplate vertical strike slip faults and associated structural developments such as localized shear zone in the lower crust in terms of numerical simulations.

In the lower crust under interplate and intraplate strike slip faults, existence of localized deformation has been suggested by geophysical and geological studies. Several different shear strain concentration mechanisms such as shear and frictional heating, power law creep, and grain size reduction have been proposed to explain the formation and maintenance of the shear zone under an interplate strike slip fault such as the San Andreas fault. However, since intraplate strike slip faults have small slip rates less than 1 cm/yr, the controlling mechanisms of shear strain concentration in the lower crust may be different from the one for the interplate fault. To better understand the mechanism and boundary conditions that influence the deformation of the lower crust, two-dimensional numerical experiments are conducted for the deformation of the lower crust under an intraplate strike slip fault based on laboratory-derived power law rheologies considering the effects of grain size and water.

The result shows that the power law rheology is the most important mechanism controlling the deformation of the lower crust. Compared to the case with a linear-rheology, the degree of the shear strain localization in the cases with nonlinear rheology is significantly higher. The maximum value of the shear strain rate in the nonlinear case is ~ 2 times larger than the linear case. On the other hand, there is almost no difference between the case with constant and non-constant grain size. In the case with non-constant grain size, as a result of competing effects of grain size reduction and grain growth, characteristic spatial distribution of the grain size appears as a function of depth and distance from the fault. This grain size distribution plays a role of maintaining the shear localization under the fault. In the previous studies for interplate strike slip fault, effective viscosity reduction due to thermal weakening has been considered to play a central role to develop shear zone in the lower crust. On the other hand, in the case of intraplate strike slip fault, owing to the slow slip rate (1 mm/yr), shear and frictional heating has negligible effects on the deformation of the shear zone. The heat production rate depends weakly on the rock rheology; the maximum temperature increase over 3 Myr is only about several tens of degrees.

Unlike the lower crust where aseismic plastic deformation occurs, elastic deformation and brittle fracture occur in the upper crust. Mechanical interaction between different parts of the crust is important to understand crustal deformation and seismogenic processes around crustal faults. Therefore, I further investigate the evolution of tectonic background stress, elastic as well as the inelastic strain in a crust-upper mantle system around an infinitely long vertical strike slip fault. Based on the previous

results, I assume that both the crust and the upper mantle are composed of nonlinear viscoelastic materials whose effective viscosity is controlled by power law rheologies. In this model, stress evolution is simulated starting from an initial stress-free condition, and stress accumulates due to a constant far-field loading at 50 km away from the fault. As the stress accumulates, brittle fractures occur in the upper crust. Also, recurrence of earthquakes is modeled based on the Coulomb failure criterion. The frictional cohesive strength is assumed to be 5 MPa.

In the early stage of stress evolution, deformation of the crust and the upper mantle is dominated by a uniform simple shear. Shear localization in the lower crust starts when coseismic rupture extends to the entire brittle upper crust. Together with this transition, the earthquake recurrence interval decreases by an order of magnitude from ~ 16 to ~ 1.6 kyrs. A basal drag originated from the localized plastic flow of the lower crust plays an important role in tectonic loading of the crustal faults by increasing the stressing rate from ~ 300 to ~ 3000 kPa/yr. The recurrence interval and the maximum stressing rate after the start of regular cycle depend on the degree of strain localization in the lower crust which is correlated with the crustal rheologies.

After the localized deformation is fully developed in the lower crust, the fault slip rate catches up with the far field velocity and earthquakes start to occur periodically. In the case of an intraplate strike slip fault, such a steady state can be reached in a several hundred thousand years from the beginning. A shear zone with large cumulative strain needs few million years to develop under an intraplate strike slip fault, which is much longer than the time for shear strain rate to be localized. The shear strain in the shear

zone under the fault linearly depends on the cumulative fault offset at the surface. Under a strike slip fault with a cumulative offset longer than few kilometers, a shear zone with large shear strain is likely to exist in the lower crust and it can be observed by geophysical means.

The model successfully reproduced evolution of intraplate strike slip faulting, development of a shear zone in the lower crust under the fault, and tectonic stress build-up in the bulk of the crust around an intraplate strike slip fault. The results of this model provide important clues to understand the problems associated with the intraplate strike slip faulting such as the degree of the shear strain concentration in the lower crust under the fault and the discrepancy between geodetic and geologic fault slip rates. The model demonstrates the importance of considering the whole mechanical system of the crust in which rheological properties, thermal structure, and fault activities are interactive one another for better understanding of crustal seismogenesis.

Acknowledgement

First and foremost I want to thank my advisor, Professor Takeshi Sagiya, for his fundamental role in my study. He provide me with every bit of guidance and assistance that I needed during my first few semesters; then, when I felt ready to venture into new research ares, he gave me the freedom to create the new models and test the new ideas, at the same time continuing to contribute valuable feedback, advice, and encouragement. His guidance helped me in all the time of research and writing of this thesis. I could not have imagined having a better advisor and mentor for my study.

Besides my advisor, I would like to thank Professor Takeo Ito. His detailed and thoughtful review of my research helped me a lot. He also provide me with the world's most powerful CPU and GPU and my calculation speed was significantly improved. I cannot thank him enough for all the help he's given me.

My sincere thanks also goes to all teachers and researchers in the Earth and Planetary Dynamics Department for their comments and advice. Your knowledge inspires me a lot. I would like to thank my fellow students for their feedback, cooperation and of course friendship. In particular, I am grateful to Dr. Ryohei Sasajima, Dr. Angela Meneses, Dr. Kenji Yasuda and Mr. Shuhei Tsuji for enlightening me on various aspects of my research.

I am grateful to the Ministry of Education, Culture, Sports, Science and Technology of Japan for sponsoring my stay in Japan. This study was supported by JSPS KAKENHI Grant 26109003.

Last but not least, I would like to express my deepest gratitude to mom and dad, who supported me both financially and emotionally throughout my time study in Japan. They always encourage me to pursue my dreams. This dissertation would not have been possible without their warm love, continued patience, and endless support. They are the most important people in my world and I dedicate this dissertation to them.

Contents

1	Introduction	15
2	Shear strain concentration mechanisms in the lower crust under an intraplate strike slip fault based on rheological laws of rocks	23
2.1	Introduction	24
2.2	Model description	26
2.2.1	Model Geometry	26
2.2.2	Rheology	28
2.2.3	Initial and boundary conditions	32
2.2.4	Thermo-mechanical coupling model	35
2.2.5	Calculation method	36
2.3	Results	37
2.3.1	Shear stress distribution	37
2.3.2	Grain size distribution	41
2.3.3	Temperature increase	42
2.3.4	Effective viscosity structure	44
2.4	Discussion	48

2.4.1	Comparison with thermo-mechanical model in previous studies	48
2.4.2	Possible shear strain concentration mechanisms for shear zone under intraplate strike slip fault	50
2.4.3	Implication to the deformation of the lower crust	52
2.5	Conclusions	53
3	Evolution of intraplate strike slip fault and the shear zone under the fault	55
3.1	Introduction	55
3.2	Model description	58
3.2.1	Model geometry	58
3.2.2	Temperature structure	59
3.2.3	Rheologies	61
3.2.4	Earthquake cycle model	62
3.3	Results	67
3.3.1	Shear stress evolution	68
3.3.2	Evolution of effective viscosity	70
3.3.3	Evolution of the plastic deformation rate	72
3.3.4	Evolution of shear strain	73
3.3.5	Evolution of the fault behavior	76
3.3.6	Effect of model configurations	79
3.4	Discussion	85
3.4.1	Stage of the fault evolution	85
3.4.2	Development of a ductile shear zone development	87

3.4.3	Implication to the discrepancy between Geodetic and Geological fault slip rate	91
3.4.4	Mechanical model comparison	93
3.5	Conclusions	96
4	Discussions	98
4.1	Effect of off-fault plastic deformation on the evolution of intraplate strike slip fault	99
4.1.1	Model settings	101
4.1.2	Shear stress evolution process	102
4.1.3	Evolution of plastic deformation in the upper crust	104
4.1.4	Effect of the plastic strength on the off-fault plastic deformation	108
4.1.5	Effect of off-fault plastic deformation on fault evolution and recurrence interval	110
4.1.6	Effect of off-fault plastic deformation on the geological slip rate	113
4.2	Can the mantle flow load the continental crust ?	116
4.3	Deformation around a small intraplate strike slip fault	119
4.4	Implication for the earthquake activities	121
5	Conclusions	123

List of Figures

1	Long-term deformation (c) is a summation of interseismic displacement (a) and coseismic displacement (b). S is coseismic slip on the surface and D is the locking depth.	16
2	Screw dislocation in an elastic half-space model used to fit the interseismic geodetic measurements across strike slip faults (<i>Savage and Burford, 1973</i>).	17
3	Geometry for model 1 (<i>Zhang and Sagiya, 2017</i>).	28
4	Contours of equilibrium grain size (L_e) as a function of temperature (T) and stress (τ_s), assuming wet anorthite rheology (<i>Zhang and Sagiya, 2017</i>).	31
5	(a) Fault slip velocity (v) and (b) shear stress on the bilateral symmetry line in the lower crust for model W1E. τ_s is the second deviatoric stress invariant; τ_{yx} and τ_{yz} are the yx and yz components of shear stress, respectively; and the straight broken line is based on Byerlee's law. The gray broken lines indicates the bottom of the BDTZ (<i>Zhang and Sagiya, 2017</i>).	34

6	Contours of the horizontal (a, τ_{yx}) and the vertical (b, τ_{yz}) shear stress in the lower crust as a function of depth and distance from the fault for model W1E. The gray broken lines indicates the bottom of the BDTZ (<i>Zhang and Sagiya, 2017</i>).	38
7	Contours of shear stress (τ_s) in the lower crust as a function of depth and distance from the fault for models (a) W1E, (b) D1E, (c) W30E,(f) W1C,(e) D1C, and (f) W30C. The thickness of the lower crust and the depth of the bottom of the BDTZ are dependent on the assumed rheology and far-field velocity (v_0). The gray broken lines indicate the bottom of the BDTZ (<i>Zhang and Sagiya, 2017</i>).	40
8	Contours of equilibrium grain size distribution as a function of depth and distance from the fault, calculated from case W1E (a) and D1E (b). The <i>gray broken lines</i> indicate the depth of the bottom of the BDTZ (<i>Zhang and Sagiya, 2017</i>).	43
9	Temperature anomaly produced by shear and frictional heating versus depth and distance from the fault for models (a) W1E,(b) D1E and (c) W30E after 3 Myr of fault sliding. \times shows the location of maximum temperature increase; numbers indicate the magnitude of maximum temperature increase (<i>Zhang and Sagiya, 2017</i>).	44
10	Surface heat flow for simulation of interplate (Dotted line) and intraplate(Solid line) strike slip fault, Sharp peak on top of the fault is created by fault frictional heating (<i>Zhang and Sagiya, 2017</i>).	45

11	Effective viscosities versus depth and distance from fault for equilibrium grain size(a~c) and constant grain size(d~f). Broken line in d~f indicates the location where diffusion and dislocation creep has same shear strain rate (<i>Zhang and Sagiya, 2017</i>).	47
12	Shear strain rate changed by increased temperature for (a)W1E and (b)W30E, broken contour lines shows the shear strain rate with temperature field of 1-D geothermal gradient and solid contour lines shows the shear strain rate with temperature field from a 3Myr simulation (<i>Zhang and Sagiya, 2017</i>).	49
13	Shear strain rate for (a)W1E, (b)W1C (c)linear (d)D1E and (e)D1C. The grain size of linear case is a constant of 215 μm , minimum grain size in model W1E (<i>Zhang and Sagiya, 2017</i>).	51
14	Geometry for model 2. Mohorovičić discontinuity (Moho) is a horizontal boundary at the depth of 35 km (<i>Zhang and Sagiya, 2018</i>).	59
15	Temperature structure used in model 1 (broken line) and model 2 (Solid blue line). Geothermal gradient near Earth’s surface are same in the model 1 and model 2. By considering the upward migration of the radiologic elements, in model 2, the temperature is lower in the deeper part of the crust compared to model 1.	60
16	The algorithm for calculation of the earthquake cycle, both interseismic and coseismic stress change is solved using stress equilibrium equation (eq. 2.14) (<i>Zhang and Sagiya, 2018</i>).	62

17	Stress concentration at the crack tip can be eliminated by several iterations. Time does not proceed in these iterations. The dark blue line is the stress on the fault before the first earthquake. Other solid lines are the shear stress on the fault after each iteration (<i>Zhang and Sagiya, 2018</i>).	66
18	Shear stress τ_{yx} evolution in the model of Q1W, each figure is plotted right before an earthquake, the number of earthquake cycle is shown in each figure and the elapsed time is shown on the top of each figure (<i>Zhang and Sagiya, 2018</i>).	68
19	The effective viscosity η_{eff} evolution in the model of Q1W, each figure is plotted right before an earthquake, the number of earthquake cycle is shown in each figure and the elapsed time is shown on the top of each figure (<i>Zhang and Sagiya, 2018</i>).	71
20	The viscous shear strain rate $\dot{\epsilon}_{yx}$ evolution in the model of Q1W, each figure is plotted right before an earthquake, the number of earthquake cycle is shown in each figure and the elapsed time is shown on the top of each figure (<i>Zhang and Sagiya, 2018</i>).	74
21	The cumulative shear strain ϵ_{yx} in the model of Q1W, each figure is plotted right before an earthquake, the number of earthquake cycle is shown in each figure and the elapsed time is shown on the top of each figure (<i>Zhang and Sagiya, 2018</i>).	75

22	<p>Stress change rate averaged over an earthquake cycle (a), coseismic offset (b) and shear stress on fault plane right before an earthquake (c). Lines with different colors indicate the result from earthquakes at different time. The gray broken lines indicate the depth of BDTZ (<i>Zhang and Sagiya, 2018</i>).</p>	77
23	<p>Shear stress(a-e), effective viscosity(f-j) and viscous shear strain rate(k-o) distributions of intraplate cases after regular recurrence is reached. Figures are plotted at the end of an interseismic period right before an earthquake. Each row shows the results of a case and the name of the case is shown on the top of the row. White broken lines indicate the location where viscous shear strain rate is not changed from the shear strain rate of uniformly distributed simple shear which is about $3.17 \times 10^{-16} \text{ s}^{-1}$ in intraplate cases. The gray broken lines indicate the depth of BDTZ (<i>Zhang and Sagiya, 2018</i>).</p>	80

24	Shear stress(a and b), effective viscosity(c and d) and viscous shear strain rate(e and f) distributions of interplate cases after regular recurrence is reached. Figures are plotted at the end of an interseismic period right before an earthquake. Each column shows the result of a case and name of the case is shown at the end of the column. White broken lines indicate the location where viscous shear strain rate is not changed from the shear strain rate of uniformly distributed simple shear which is about $9.51 \times 10^{-15} \text{ s}^{-1}$ in interplate cases. The gray broken lines indicate the depth of BDTZ (<i>Zhang and Sagiya, 2018</i>).	83
25	Time evolution of coseismic offset on the surface in each earthquakes (a), recurrence interval (b) and (c) fault tip depth for model Q1W. Each rhombus dots in (a) represents an earthquake (<i>Zhang and Sagiya, 2018</i>).	86
26	Cumulative fault slip (a) and Geological slip rate (b) from the case of Q1W (<i>Zhang and Sagiya, 2018</i>).	89
27	Shear strain(a) and Shear strain rate(b) and under the fault in the lower crust, example taken from case Q1W (<i>Zhang and Sagiya, 2018</i>).	90
28	Geometry for the model consider the plastic deformation in the upper crust	101
29	Shear stress τ_{yx} evolution in the model of Q1W_VEP_10, each figure is plotted right before an earthquake, the number of earthquake cycle is shown in each figure and the elapsed time is shown on the top of each figure.	103

30	Plastic shear strain (ϵ_{yx}) accumulated in an earthquake cycle in the model with 10 MPa off-fault cohesive strength, the number of earthquake cycle and the elapsed time is shown in each figure. The red arrows indicate the depth of the fault tip and the white dot lines indicate the boundaries of the BDTZ	104
31	Evolution of the plastic shear strain rate ($\dot{\epsilon}_{yx}^p$) in an earthquake cycle in the case of Q1W_VEP_10 after the regular cycle is reached, the elapsed time in an interseismic period is shown in each figure.	107
32	Distribution of plastic strain in the case of Q1W_VEP_10 (a), Q1W_VEP_15 (b) and Q1W_VEP_20 (c) at 1.5 Myrs. The white dot lines indicate the boundaries of the BDTZ.	109
33	Stress change rate averaged over an earthquake cycle (a), coseismic offset (b) and shear stress on fault plane right before an earthquake. Lines with different colors indicate the result from earthquakes at different time. The gray broken lines indicate the depth of BDTZ.	111
34	Time evolution of coseismic offset on the surface in each earthquakes (a) and recurrence interval (b) for case Q1W_VEP_10 (Red rhombus dots and lines) and Q1W (Blue rhombus dots and lines). Each rhombus dots in (a) represents an earthquake.	112
35	Cumulative fault slip from the case of Q1W (Black line), Q1W_VEP_10 (Orange line), Q1W_VEP_15 (Blue line) and Q1W_VEP_20 (Red line).	114

36 Shear stress (a) τ_{yx} and (b) τ_{yz} in the crust after 20 kyrs of loading from upper mantle. Wet quartz rheology (Table 4) is assumed in this calculation. 116

37 Effective viscosity in the crust after 20 kyrs of loading from upper mantle. Wet quartz rheology (Table 4) is assumed in this calculation. . . 118

38 Shear stress (a) τ_{yx} and (b) τ_{yz} in the crust after 440 kyrs of loading from upper mantle. Dry Anorthite rheology (Table 2) is assumed in this calculation. 119

List of Tables

1	Model configurations for the evaluation of shear strain concentration mechanisms	27
2	Rheological Properties of Rocks From Laboratory Measurements (<i>Rybacki et al., 2006</i>).	30
3	Thermal and mechanical parameters	35
4	Rheological properties of rocks from laboratory measurements	61
5	Model configurations for the fault evolution process	64
6	Model properties after regular recurrence starts	79
7	Model properties after regular recurrence starts	110

Chapter 1

Introduction

Horizontal displacements in strike slip faults represent one of the fundamental modes of deformation in the Earth's crust which accommodates the relative motion of tectonic plates. In the plate tectonics theory, to a first-order approximation, the interplate strike slip deformation zone is a narrow region along the plate boundaries and the plate interior is assumed to be rigid. Along the interplate strike slip fault, such as the San Andreas fault (SAF) in California, United States, many earthquakes occurred in the past (e.g. *Smith and Sandwell, 2006*). One of the most intensively studied interplate strike slip earthquake was the 1906 San Francisco earthquake. Detailed geodetic observations before and after this earthquakes reveal the general character of the crustal deformation around the fault between the earthquakes. These observations show that deformations related to the earthquake are concentrated near the fault (Figure 1a) . Based on these observations, *Reid (1910)* proposed the elastic rebound theory, which explains the strain in the crust around the fault is accumulated elastically by the constant relative motion in the far field and accumulated strain is released by a sudden rupture along the fault.

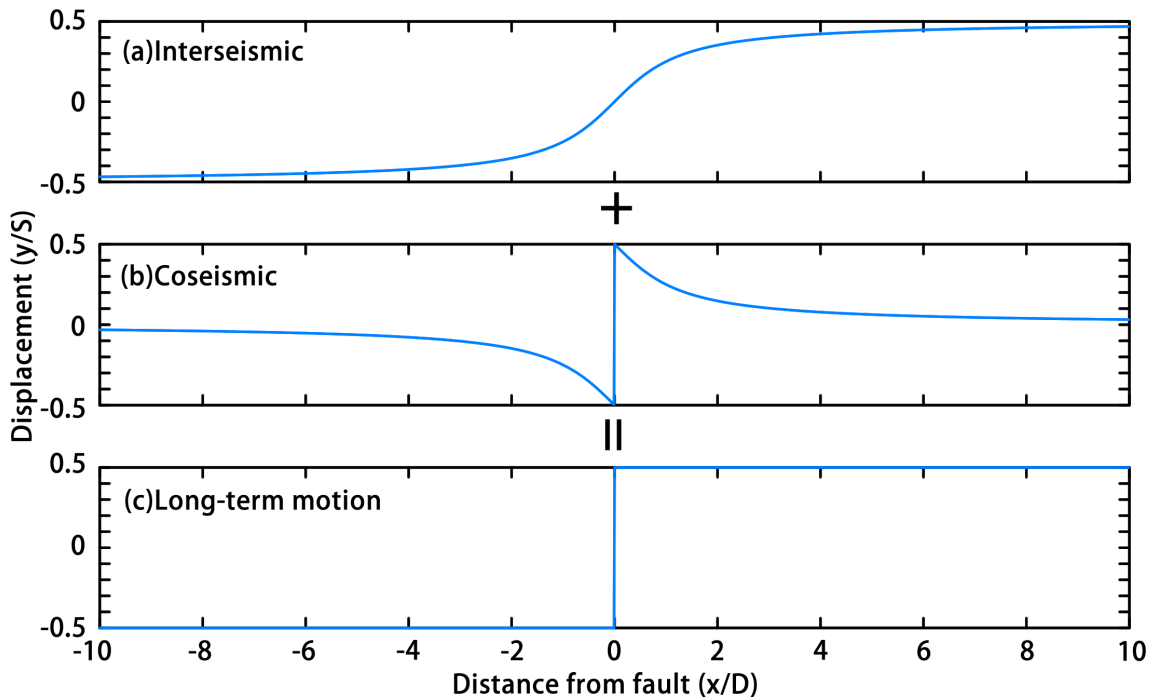


Figure 1: Long-term deformation (c) is a summation of interseismic displacement (a) and coseismic displacement (b). S is coseismic slip on the surface and D is the locking depth.

Although the observed surface deformation can be well described by the elastic rebound theory, the mechanisms of the localized deformation around the strike slip fault was not well understood until the introduction of the buried screw dislocation model of interseismic deformation for long strike slip faults (Figure 2) in *Savage and Burford (1973)*. This model has been commonly used in the studies for interplate as well as the intraplate strike slip fault (e.g. *Johnson and Segall, 2004*; *Ohzono et al., 2011*; *Yamasaki et al., 2014*). A simple kinematic model with a screw dislocation at depth in an elastic half space can provide a fairly good fit to the observed velocity field and can be used to estimate the total relative velocity across the fault, as well as the fault locking depth. Despite the success of the elastic screw dislocation model in matching the observed interseismic deformation, the mechanisms of the localized

steady slip at depth under the fault was not well understood. In contrast, according to the rheological experiments, crustal rocks under the fault considered to be deformed by distributed plastic flow under high temperature/pressure condition in the lower crust (e.g. *Kohlstedt et al., 1995*).

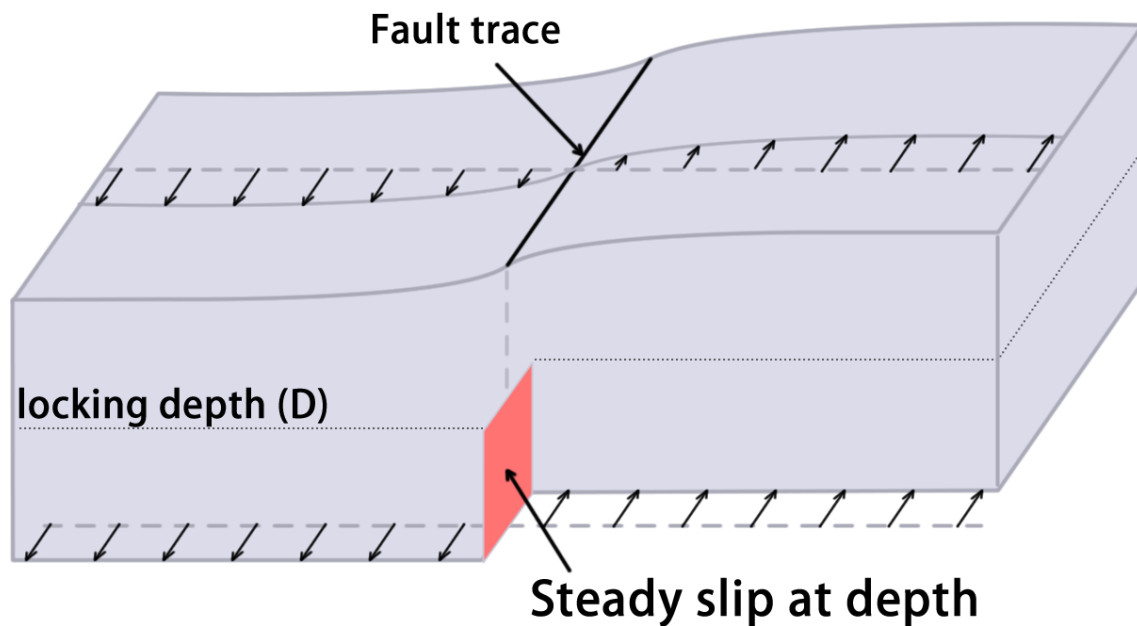


Figure 2: Screw dislocation in an elastic half-space model used to fit the interseismic geodetic measurements across strike slip faults (*Savage and Burford, 1973*).

Deformation processes in the lower crust have been inferred based on various geophysical as well as geological studies, which suggest the existence of a localized shear zone under the fault. The direct evidence of the localized shear zone are shown by the geological studies. Highly strained mylonites form in plastic shear zone under the fault are commonly observed on the exhumed fault zones (e.g. *White et al., 1980; Sibson, 1980*). The undergoing localized plastic deformation under the fault has been suggested by geophysical observations. Under interplate strike slip faults, seismic tomography suggested vertical offsets of the Mohorovičić discontinuities (e.g. *Henstock*

et al., 1997; *Zhu*, 2000) which indicates the relative motion of the crustal block with different thickness are accommodated by the localized deformation under the fault. In the lower crust, seismic velocity anomalies (e.g. *Wittlinger et al.*, 1998; *Nakajima and Hasegawa*, 2007; *Nakajima et al.*, 2010), high-conductivity zones (*Ogawa and Honkura*, 2004; *Yoshimura et al.*, 2009; *Becken and Ritter*, 2012) and deep tremors on the downward extension of major faults (e.g. *Norris and Toy*, 2014) suggest the existence of weak zones where localized deformation occurs.

However, due to a limited spatial resolution of geophysical observations, the degree of the shear strain concentration in the lower crust is not well resolved. To solve this problem, based on the rheological experiments, various shear strain localization mechanisms, such as thermal weakening, grain size reduction and power law creep have been considered in the thermo-mechanical model. Because the shear strength of the ductile material exponentially depends on the temperature, among these mechanisms, shear and frictional heating was considered to play the principal role in the process of developing the shear zone under an interplate strike slip fault (e.g. *Thatcher and England*, 1998; *Takeuchi and Fialko*, 2012).

Compared to major interplate strike slip faults, intraplate strike slip faults have much slower slip rate, at < 10 mm/year and because of that, the deformation in the lower crust should occur at a much slower rate. The shear strain concentration mechanisms considered for interplate strike slip faults may have different implications and different weights on the development and the maintenance of a shear zone under an slowly deforming intraplate strike slip fault.

To understand the deformation of the continental crust around an intraplate strike slip fault, in the first step, I constructed a thermo-mechanical model based on laboratory-derived rheological laws of lower crustal rocks (Model 1). With a creeping fault in the upper crust, I conduct a series of numerical simulations on deformation of the lower crust under an intraplate strike slip fault. As the temperature changes with time due to shear as well as frictional heating, the evolution of the deformation patterns and the viscosity structure in the geological time scale are evaluated. Based on the simulation results of different rheological settings, I evaluated the relative importance of the shear strain concentration mechanisms including shear and frictional heating, grain size reduction and power law creep. The effect of water weakening is quantitatively evaluated with water fugacity. In addition, deformation of the shear zone beneath an intraplate and an interplate strike slip faults are compared to identify the controlling factors for lower crustal shear localization under intraplate conditions. Chapter 2 of this thesis contains the relevant methods, results, and discussions.

Another difference between intraplate and interplate strike slip faults are their maturity. Generally, major interplate strike slip faults such as the San Andreas fault are considered to be matured faults, as the fault offsets of may as long as few hundreds of kilometers (*Atwater, 1989*). In the last few millions of years, the slip rate of SAF are considered to be stable (*DeMets and Dixon, 1999*). In such a long time scale, thermo-mechanical models for the deformation of interplate strike slip fault show a steady-state behavior. Therefore, in the previous studies using rheological laws to simulate the lower crustal deformation, time dependent solution has not been considered. On

the other hand, for intraplate strike slip fault, geologically estimated slip rates are often slower than the geodetic estimations (e.g. *Oskin et al., 2008; Ohzono et al., 2011; Herbert et al., 2014*). Steady state may not be achieved on immature intraplate strike slip faults with a small cumulative displacement. In order to improve our understanding of evolution process of intraplate strike slip faults, what kind of role elastic/brittle and plastic deformation plays and how the elastic upper crust and the plastic lower crust interact with each other are important questions to answer. There are two end-member models for the interaction between the upper and the lower crust. One is the basal drag model, which postulates the upper crust is passively follows the distributed flow of the stronger plastic lower crust (*Bourne et al., 1998*). The other is the viscoelastic coupling model (*Savage and Prescott, 1978*), which considers the viscoelastic substratum under the fault response to the earthquake rupture on the fault and the far field loading in the upper crust to create the time-dependent deformation around a strike slip fault zone. In that model, the deformation of the viscoelastic lower crust is a result strike slip faulting in the upper crust. The observed deformation along a vertical strike slip fault can be equally well reproduced by both of these models, which means that geodetic observation alone cannot resolve the problem (*Savage et al., 1999*).

Geophysical observations can provide direct constrains on the deformation of the lower crust. There are some geophysical studies (e.g. *Henstock et al., 1997; Zhu, 2000*) suggesting that faults cut through the entire crust. One the other hand, other studies show that the Moho depth varies rather smoothly across the fault zone, indicating that deformation in the lower crust is broadly distributed (e.g. *Wilson et al., 2004; DESERT*

Group et al., 2004). Again, opinions are divided because geophysical observations cannot resolve the ongoing deformation of the lower crust.

Therefore, I try to answer the questions through a construction of a two-dimensional self-consistent mechanical model (Model 2). In this model, I simulate the evolution of the shear stress, effective viscosity and deformation along an infinitely long strike slip fault with constant tectonic loading in the far field on an initially unstressed crust-mantle system. The entire system is composed of nonlinear Maxwell materials whose plastic flow is controlled by the experimental rheological laws and the occurrence of earthquakes are controlled by the stress on the fault. I show how the crustal structures such as the upper crustal fault, localized shear zone in the lower crust, and heterogeneous viscosity distributions are developed. Also, the results with different rheological properties and boundary conditions are compared to find out how model settings affect the deformation. Finally, I discuss how the evolution of the fault related structures affects pattern of geodetic, geological and geophysical observations. Chapter 3 of this thesis contains the relevant methods, results, and discussions.

In this study, there are few assumptions are not realistic and should be addressed in the future study. Firstly, in the upper crust, the off-fault plastic deformation can occurs to accommodate the loading from the far field. The plastic deformation in the crust occurs only when plastic strength is reached. It is different from the plastic deformation in the lower crust, which occurs upon loading. Off-fault plastic deformation can affect the tectonic loading process of earthquakes. Since the upper crust of mechanical model assume viscoelastic rheologies deform elastically, it is necessary to modify

Model 2 to include the plastic deformation in the upper crust. A possible solution to reduce the shear stress in the upper crust is to assume a visco-elasto-plastic deformation for the entire crust. In Chapter 4.1, I discuss the effect of the plastic deformation on the evolution of the fault based on preliminary results of the model considering the off-fault plastic deformation in the upper crust. Secondly, In the interior of the continental plate far away from plate boundaries, the fault may loaded from below by mantle flow. In Chapter 4.2, I discuss the possibility of loading a continental crust by the mantle flow. Thirdly, in the model of this study, the intraplate strike slip fault is assumed to be infinitely long, which is unrealistic since the fault length are typically shorter than few hundreds of kilometers. In Chapter 4.3, I discuss the influence of the fault ends and I propose a possible solution to simulate the behavior of the fault ends. Finally, in Chapter 4.4, I discuss the implications for the intraplate strike slip earthquake activities.

Chapter 2

Shear strain concentration mechanisms in the lower crust under an intraplate strike slip fault based on rheological laws of rocks

In this chapter, I evaluate the relative significance of shear strain concentration mechanisms in the evolution of the shear zone under an intraplate strike slip fault. In previous studies, several shear strain concentration mechanisms have been considered to understand the formation and maintenance of the shear zone under an interplate strike slip fault. Those candidate mechanisms include dislocation (power law) creep (e.g. *Kirby and Kronenberg, 1987*), grain size reduction (e.g. *De Bresser et al., 2001*) and shear and frictional heating (e.g. *Yuen et al., 1978; Thatcher and England, 1998*). For an intraplate strike slip fault whose slip rate is much slower than interplate strike slip faults, there is no comprehensive understanding for the development of the shear zone

under an intraplate strike slip fault. In this study, I construct a numerical model in a two-dimensional space perpendicular to the fault to simulate the shear deformation of the lower crust under the fault. The plastic deformation in the lower crust is controlled by laboratory derived rheological laws. I test the model with different mechanisms to investigate which mechanisms have the most significant impact on the formation of localized deformation in the lower crust under the fault. This chapter is based on the study of *Zhang and Sagiya (2017)*.

2.1 Introduction

Interplate strike slip faults accommodate relative motions between tectonic plates. It is believed that there are highly localized deformation zones in the lower crust beneath them. Evidence of the existence of the shear zones has been shown by various observational, experimental and theoretical studies as well as geological observations of exhumed mylonite zones. Because the viscosity of the crustal rocks follows an Arrhenius relationship with temperature, thermal weakening caused by shear heating has been considered as the most important mechanism for the development and the maintenance of shear zones (e.g. *Yuen et al., 1978; Fleitout and Froidevaux, 1980*). On the San Andreas fault, a broadly distributed heat flow anomaly has been observed (*Lachenbruch and Sass, 1980*). The observations are consistent with the results of thermo-mechanical model for interplate strike slip fault (e.g. *Thatcher and England, 1998; Leloup et al., 1999; Takeuchi and Fialko, 2012*). These models predict a temperature increase of several hundreds degrees in the lower crust under the fault and

produce an widely distributed heat flow anomaly on the surface. A large temperature increase in the lower crust results in a weak zone and lower seismic velocity in the weak zone can be observed as a heterogeneous seismic velocity structure in the seismic tomography data (*Wittlinger et al., 1998*). Furthermore, mylonite outcrops of exhumed shear zones provide direct evidence for the existence of ductile shear zones in the lower crust under interplate (*Rutter, 1999; Little et al., 2002*) and intraplate (*Shimada et al., 2004; Fousseis et al., 2006; Takahashi, 2015*) strike slip faults.

Compared with interplate strike slip faults, intraplate strike slip faults have much slower slip rates (Less than 10 mm/yr) and younger fault ages (Less than 3 Myrs in Japanese islands *Doke et al. (2012)*). Nonetheless, similar to the interplate strike slip fault, heterogeneous structures under intraplate strike slip fault has been observed by seismic tomography (e.g. *Nakajima and Hasegawa, 2007; Nakajima et al., 2010*) and magnetotelluric survey (e.g. *Ogawa and Honkura, 2004; Yoshimura et al., 2009*). Because the spatial resolution of geophysical observations is insufficient to resolve the structures of such ductile shear zones, understanding the mechanisms that lead to shear strain concentration in the lower crust beneath an intraplate strike slip is an important step in understanding the deformation of the crust.

In this study, I construct a series of numerical simulations on the deformation in the lower crust below an active intraplate strike slip fault based on laboratory-derived rheological laws. I calculate the temperature change due to the shear as well as fault frictional heating and also calculated the viscosity and deformation pattern of the lower crust under an intraplate strike slip fault in a geological timescale. I consider three

mechanisms of strain localization, i.e. thermal weakening, grain size reduction and power law creep. The effect of water in wet rheologies is quantitatively evaluated with water fugacity. I discuss the role of shear strain concentration mechanisms and boundary conditions in the development and maintenance of the shear zone. I also compare the shear zone under intraplate and interplate strike slip faults to identify controlling factors for lower crustal shear localization under intraplate strike slip faults.

2.2 Model description

I simulated the deformation of the lower crust beneath an infinitely long strike slip fault by applying a constant velocity boundary condition representing far field tectonic loading and relative motion of two rigid blocks in the upper crust. I solved the stress equilibrium equation and the heat flow equation for a thermo-mechanical coupled model, and the deformation of the lower crustal material follows laboratory-derived rheological laws.

2.2.1 Model Geometry

The model geometry is shown in Figure 3. I considered the problem in a 2-D plane perpendicular to the fault trace. The model has three layers: a faulted rigid upper crust, a ductile lower crust, and a semi-brittle layer between the upper and the lower crust. In the upper crust, an infinitely long vertical creeping fault is assumed with the fault strike parallel to the y -axis. The lower crust and the semi-brittle regime is deformed by plastic flow. The upper boundary of the lower crust is assumed to correspond to the brittle-ductile transition (BDT) and the boundary between the rigid upper crust and

Table 1: Model configurations for the evaluation of shear strain concentration mechanisms

Model	Crustal rheology	Fault type	Grain size	z_b
W1C	Wet anorthite	Intraplate strike slip fault	Constant	15 km
D1C	Dry anorthite	Intraplate strike slip fault	Constant	25 km
W30C	Wet anorthite	Interplate strike slip fault	Constant	15 km
W1E	Wet anorthite	Intraplate strike slip fault	Equilibrium	15 km
D1E	Dry anorthite	Intraplate strike slip fault	Equilibrium	25 km
W30E	Wet anorthite	Interplate strike slip fault	Equilibrium	15 km

^aSix model configurations were tested by this study. The rheological parameters for anorthite are summarized in Table 2. The nomenclature of the model configuration is as follows: The first letter denotes water content (D, dry; W, wet), and the last letter denotes grain size (C: constant, $L=500\mu\text{m}$; E: equilibrium). The number between two letters denotes the total relative velocity in mm/year.

the semi-brittle regime is z_b . It depends on the assumption of crustal rheology (Table 1). In the semi-brittle layer from z_b to the depth of BDT, both creep on the fault and plastic deformation in the bulk of the crust are allowed. Considering the symmetry of the vertical strike slip fault, our model region includes only one side of the fault bounded by the surface and a vertical plane of the bilateral symmetry, which is taken to be the center of the shear zone. The model domain is 35km thick in the vertical(z) direction and the far field boundary is placed at 30 km away from the fault. The Mohorovičić (Moho) discontinuity is represented by a horizontal boundary at depth of 35 km.

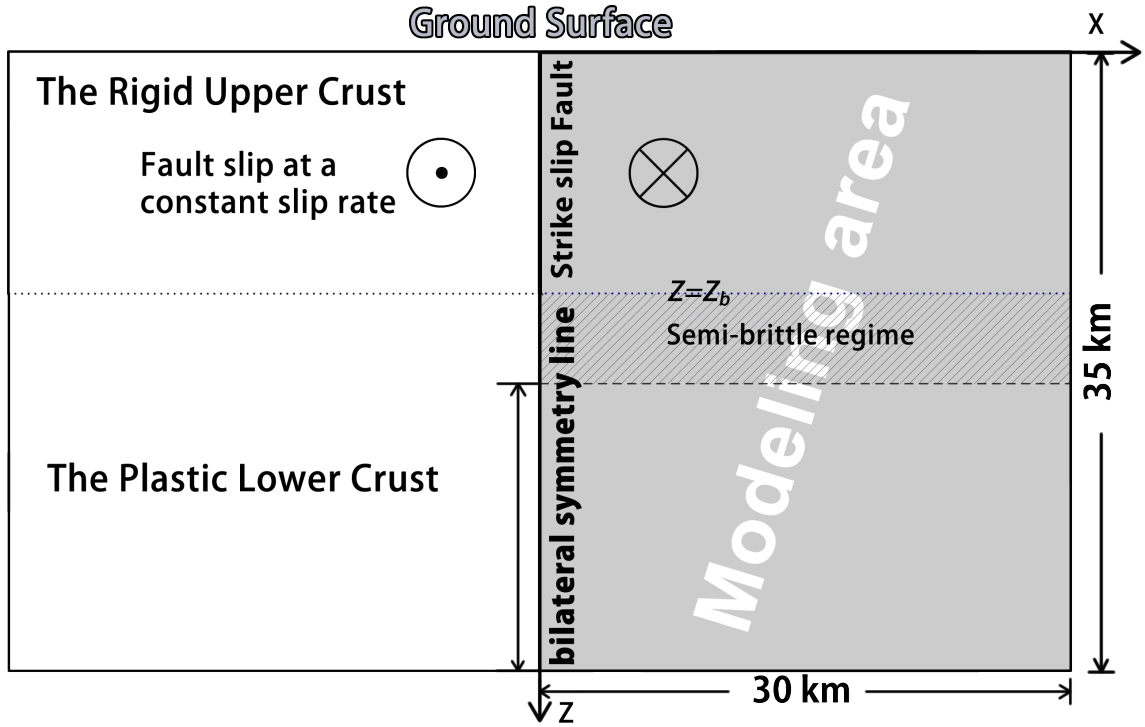


Figure 3: Geometry for model 1 (Zhang and Sagiya, 2017).

2.2.2 Rheology

In this study, the deformation of the lower crust is controlled by the experimental rheological law described as follows (e.g. Bürgmann and Dresen, 2008).

$$\dot{\epsilon} = A \tau_s^n L^{-m} f_{H_2O}^r \exp\left(-\frac{Q + pV}{RT}\right) \quad (2.1)$$

where $\dot{\epsilon}$ is the shear strain rate, τ_s is the maximum shear stress given by the square root of the second deviatoric stress invariant. L is the grain size. f_{H_2O} is water fugacity. Q and V are the activation energy and the activation volume, respectively. R is the universal gas constant. p is hydrostatic pressure, and A , n , m , r are material constants. The rheological parameters are assumed according to the results from the experiments of wet and dry anorthite (Rybacki et al., 2006). The laboratory-derived parameters used in this study are summarized in Table 2.

Regarding the deformation mechanisms of the lower crust, in this model, I considered both diffusion and dislocation creep. In the diffusion creep regime, the shear strain rate is sensitive to the grain size ($m = 3$) and it is proportional to the shear stress ($n = 1$). In the dislocation creep regime, the deformation is sensitive to the shear stress ($n = 3$). Because the shear strain rate is proportional to the shear stress with a power of $n(n > 1)$, large shear strain rate change can be achieved with a small shear stress change. For a given material, I assume that the same shear stress controls the two deformation mechanisms (e.g. *Gueydan et al., 2001; Montési and Hirth, 2003*). Under this assumption, the total strain rate $\dot{\epsilon}_{total}$ is given by the sum of diffusion $\dot{\epsilon}_{diff}$ and dislocation $\dot{\epsilon}_{disl}$ shear strain rate.

$$\dot{\epsilon}_{total} = \dot{\epsilon}_{diff} + \dot{\epsilon}_{disl} \quad (2.2)$$

Thus, the effective viscosity can be defined as follows:

$$\eta_{eff} = \tau_s / \dot{\epsilon}_{total}. \quad (2.3)$$

In the case when diffusion and dislocation creep occurs at a same rate, i.e.,

$$\dot{\epsilon}_{diff}(T, p, \tau_s, L_e) = \dot{\epsilon}_{disl}(T, p, \tau_s) \quad (2.4)$$

The expression for equilibrium grain size (EGS, L_e), which is a function of temperature (T) and shear stress (τ_s), can be solved from Eqs. 2.1 and 2.4:

$$L_e = \left[\frac{A_{diff}}{A_{disl} \tau_s^{n_{disl}-1}} \exp\left(\frac{Q_{dist} + pV_{dist} - Q_{diff} - pV_{diff}}{RT}\right) \right] \frac{1}{m_{diff}} \quad (2.5)$$

The subscript *diff* and *disl* refer to the rheological parameters for diffusion and dislocation creep, respectively, and their values are summarized in Table 2. The L_e is a

Table 2: Rheological Properties of Rocks From Laboratory Measurements (*Rybacki et al., 2006*).

Anorthite		logA	n	Q	m	r	V
		[MPa ^{-n-r} μm ^m s ⁻¹]		[kJ/mol]			[cm ³ /mol]
wet	diff. ¹	-0.7	1	159	3	1	38
	disl. ¹	0.2	3	345	0	1	38
dry	diff. ¹	12.1	1	460	3	0	24
	disl. ¹	12.7	3	641	0	0	24

¹ where diff. denotes diffusion creep and disl. denotes dislocation creep.

function of shear stress and temperature. It is large when shear stress is small (Figure 4) Under the thermal and stress conditions of the lower crust, a large variation in grain size from few tens micrometers to few centimeters are expected with this assumption (Figure 4). Under small grain size and/or stress condition, the rocks is deformed by diffusion creep, the grain growth occurs through grain-boundary migration driven by the reduction of total surface energy (e.g. *Tullis and Yund, 1991; Dresen et al., 1996*). In contrast, under large grain size and/or stress conditions, the rock is deformed by dislocation creep, dynamic recrystallization (e.g. *Tullis and Yund, 1985; Urai et al., 2013*), which result in the grain size reduction, occurs through grain-boundary migration driven by the reduction of the energy stored by the defects of crystals. In the case when reduced grain size is small enough for diffusion creep to occur, *De Bresser et al. (1998)* postulated that, the grain size adjust itself until equation 2.4 is fulfilled. In this study, the evolution of grain size is based on the experimental results of *De Bresser et al. (1998)*. For comparison, I also test a constant grain size (CGS, L_c), which is assumed to be 500 μm.

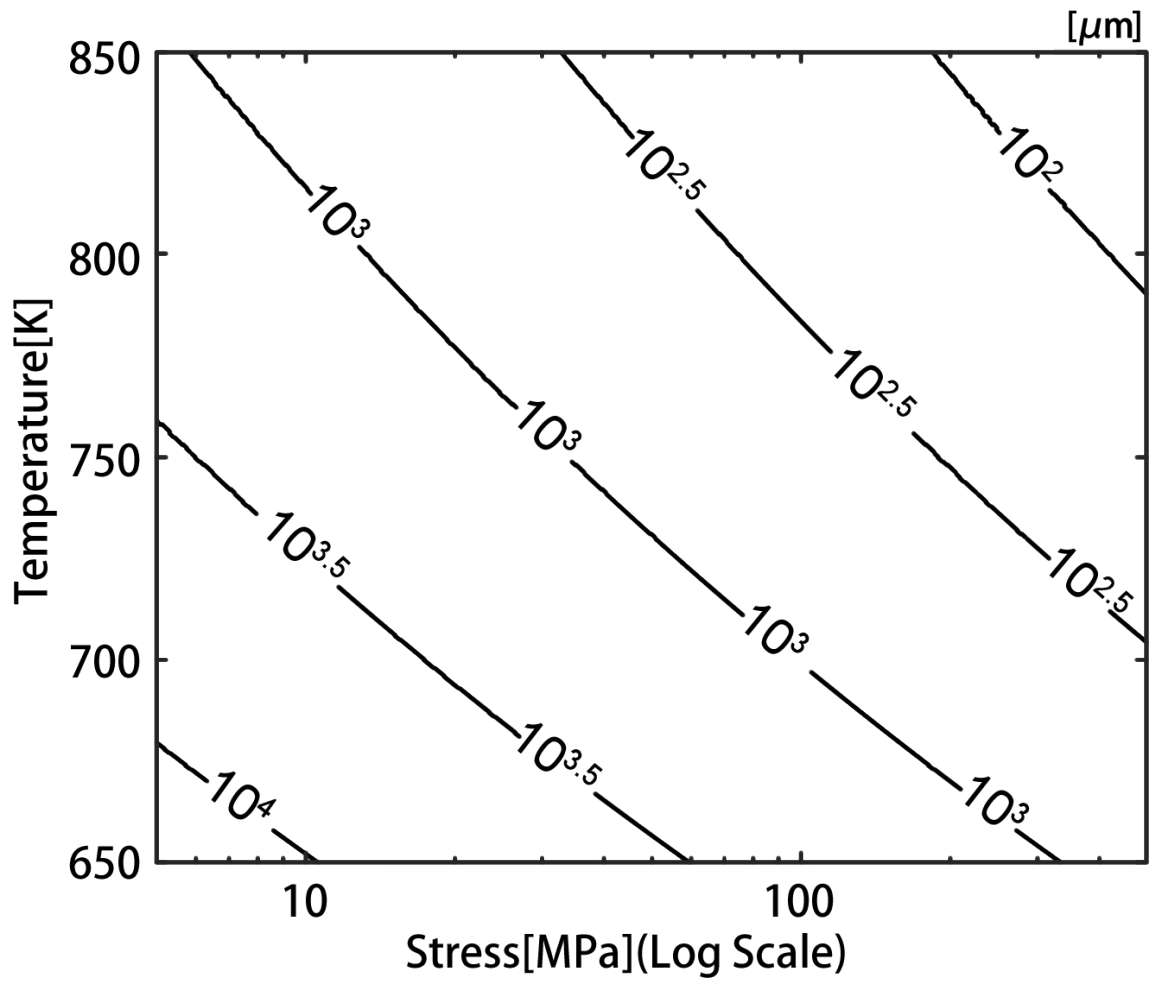


Figure 4: Contours of equilibrium grain size (L_e) as a function of temperature (T) and stress (τ_s), assuming wet anorthite rheology (Zhang and Sagiya, 2017).

The water fugacity is quantitatively evaluated in the cases with wet rheologies ($r = 1$). The weakening effect of water at different temperature (T) and pressure (p) is calculated using the following equation (Karato, 2008):

$$\log \frac{f(p, T)}{p} = \frac{1}{RT} \lim_{p_0 \rightarrow 0} \int_{p_0}^p (V_m(p', T) - V_m^{id}(p', T)) dp'. \quad (2.6)$$

where V_m and V_m^{id} is molar volume of real gas and ideal gas, respectively. The real gas is modeled by the van der Waals equation of state:

$$p = \frac{RT}{V_m - b} - \frac{a}{V_m^2}. \quad (2.7)$$

where a and b are the van der Waals constants of water (H_2O), which have been set to $5.537 \times 10^{-1} \text{m}^6 \text{Pa mol}^{-2}$ and $3.049 \times 10^{-5} \text{m}^3 \text{mol}^{-1}$, respectively. The molar volume of the real gas can be solved from Eq. 2.7 and the analytical solution can be obtained by approximating V_m as RT/p in the second term of Eq. 2.7:

$$V_m = \frac{R^3 T^3}{pR^2 T^2 + ap^2} + b. \quad (2.8)$$

Integrating Eq. 2.6 from p_0 to p using equation of state for real gas (Eq. 2.8) and ideal gas and let $p_0 = 0$, one obtains the analytical expression for fugacity,

$$f(p, T) = \frac{pR^2 T^2}{R^2 T^2 + ap} \exp\left(\frac{bp}{RT}\right). \quad (2.9)$$

2.2.3 Initial and boundary conditions

In this model, I consider an infinitely long strike slip fault and there is no vertical motion. The deformation of the lower crust is driven by the kinematic boundary condition at the horizontal and far field boundaries. The applied horizontal velocity v_0 is

half of the total relative velocity. For intraplate and interplate cases, v_0 is assumed to be 0.5 and 15 mm/year, respectively. The constant velocity is applied on the vertical boundary at the far-field from the depth of z_b to the depth of Moho at 35 km, and at the horizontal boundary between the upper crust and the semi-brittle layer at depth of z_b . On the fault plane with the brittle fracture regime, I assume the fault strength on the basis of Byerlee's law (*Byerlee, 1978*):

$$\tau_f = \begin{cases} 0.85\sigma_n & (\sigma_n < 200[MPa]) \\ 50 + 0.6\sigma_n & (200[MPa] < \sigma_n < 1700[MPa]) \end{cases} \quad (2.10)$$

where τ_f is the frictional strength and σ_n is the normal stress. On the vertical plane of bilateral symmetry in the semi-brittle layer, I apply shear strain rate as boundary condition (Figure 5b). It is given by

$$\dot{\epsilon}_{yx} \equiv \frac{\partial v}{\partial x} = \frac{2\tau_{yx}}{\eta_{eff}} = \frac{2\tau_f}{\eta_{eff}} \quad (2.11)$$

where τ_{yx} is the shear stress of plastic deformation which is assumed to be equal to the fault frictional strength (τ_f). In the semi-brittle layer, the slip rate on the fault (Figure 5a) is calculated by the integral of horizontal shear strain rate ($\dot{\epsilon}_{yx}$) over the entire domain. At depths greater than the bottom of the semi-brittle layer (BDT), the stress of plastic deformation is smaller than the strength given by Byerlee's law, therefore, the deformation is fully plastic and the velocity on the vertical plane of bilateral symmetry is zero. At the crust/mantle boundary, the boundary condition is $\partial v / \partial z = 0$.

For the thermal condition, the temperature of the Earth's surface is fixed to 0 °C and it increases with depth. At the beginning, I assume a constant geothermal gradient

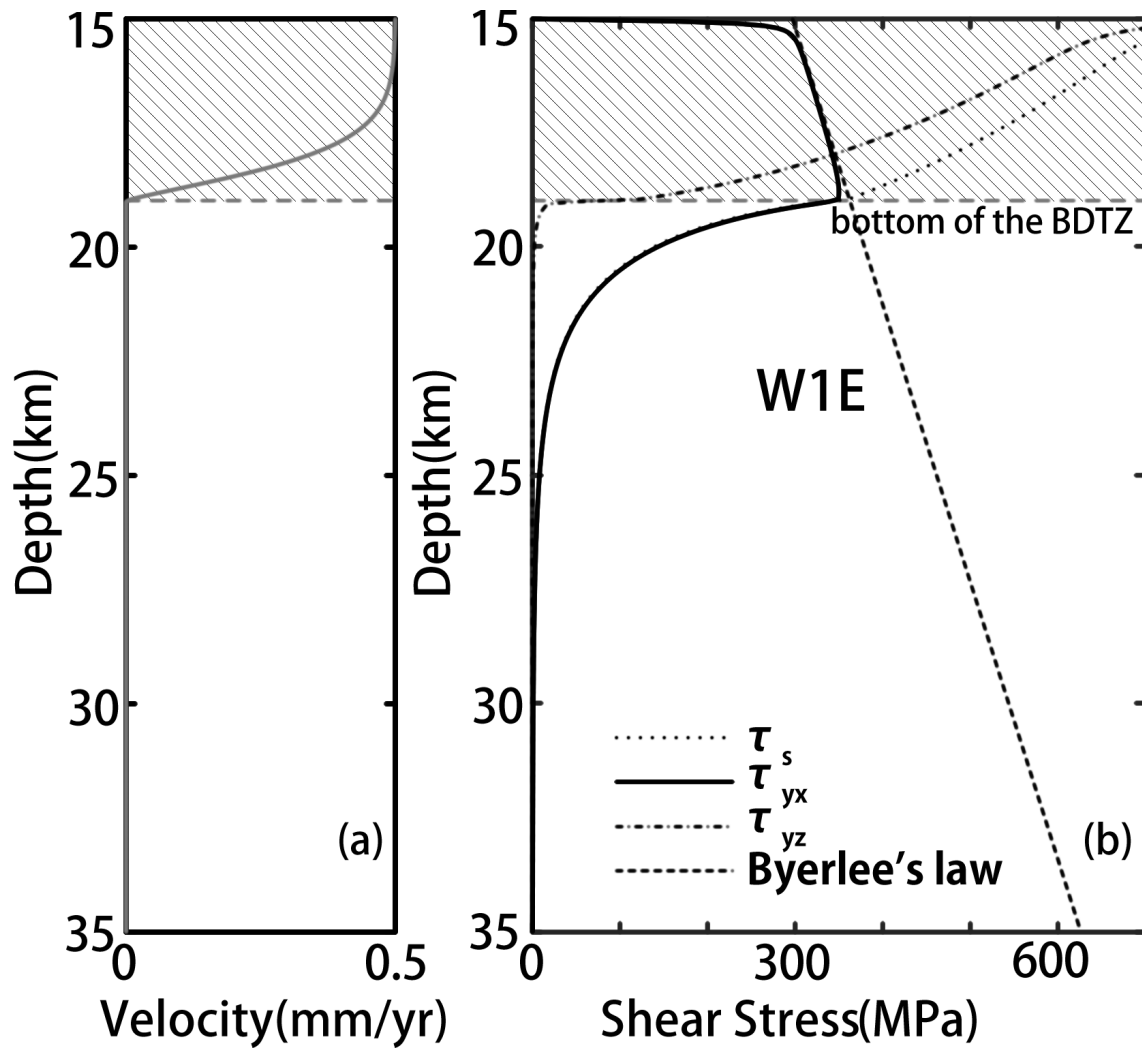


Figure 5: (a) Fault slip velocity (v) and (b) shear stress on the bilateral symmetry line in the lower crust for model W1E. τ_s is the second deviatoric stress invariant; τ_{yx} and τ_{yz} are the yx and yz components of shear stress, respectively; and the straight broken line is based on Byerlee' s law. The gray broken lines indicates the bottom of the BDTZ (*Zhang and Sagiya, 2017*).

Table 3: Thermal and mechanical parameters

Parameter name	abbr.	Value	Unit
Thermal Parameters			
Thermal Conductivity	k	2.60	$\text{W K}^{-1} \text{m}^{-1}$
Heat Capacity	C_p	1130	$\text{J kg}^{-1} \text{K}^{-1}$
Geothermal Gradient	$\frac{dT}{dz}$	25	K km^{-1}
Mechanical Parameters			
Slip rate	v_0	0.5 or 15	mm yr^{-1}
Crustal rock density	ρ	2800	kg m^{-3}

of 25 K/km (Table 3). On the vertical boundaries and the Moho, I assume zero and a constant heat flux (0.065 W/m^2 , *Turcotte and Schubert (2014)*), respectively.

2.2.4 Thermo-mechanical coupling model

Temperature of the crust changes with time due to shear and frictional heating. In our model, all mechanical energy is dissipated as heat. It is represented by a source term in the heat flow equation:

$$\rho C_p \frac{\partial T}{\partial t} = k \left(\frac{\partial^2 T}{\partial x^2} + \frac{\partial^2 T}{\partial z^2} \right) + H_s + H_f, \quad (2.12)$$

where ρ is the density, C_p is specific heat capacity at constant pressure, k is the thermal conductivity and T is the temperature. The change in temperature is a result of the thermal diffusion and volumetric heat generated by shear heating ($H_s = \tau_{ij} \dot{\epsilon}_{ij}$) and frictional heating (H_f). I assume that heat generated by friction conduct to the grid closest to the fault (*Leloup et al., 1999*):

$$H_f = \tau_f \frac{v_0}{\Delta x}, \quad (2.13)$$

where Δx is the width along the x -axis of the considered unit cell. The magnitude of the source terms on the right hand side of heat equation represents the intensity of the heat sources which depends on the grid size. Because the amount of heat generated from the heat sources is independent of the grid size, the chosen grid size has almost no influence on the time dependent solutions of the temperature distributions as the generated heat is spread out in the entire crust. The heat flow equation is solved in the entire modeling area, which is a 2-D space perpendicular to the fault (gray-colored area in Fig 3). In each time step, I assumed that viscous shear strain rate is constant in time, and it is solved from the stress equilibrium equation. Because the motion is purely horizontal, the only non-zero stress components are τ_{yx} (the shear stress on vertical planes parallel to the fault plane) and τ_{yz} (the shear stress on horizontal planes perpendicular to the fault plane):

$$\frac{\partial \tau_{yx}}{\partial x} + \frac{\partial \tau_{yz}}{\partial z} = 0. \quad (2.14)$$

2.2.5 Calculation method

The calculations in this study were preformed in MATLAB. The stress equilibrium equation (Eq.2.14) is solved by Partial Differential Equation Toolbox using finite element method. The finite element mesh consists of two element layers, each composed of 256 elements in both depth (z) and fault-perpendicular (x) direction, for a total of 131072 triangular elements. The node spacing is uniform in both x and z directions. The heat flow equation is solved using Alternating Direction Implicit finite difference method (*Buzbee et al., 1970*). The heat flow equation (Eq.2.12) is solved on a grid

containing 700×600 (420,000) cells, each of which is 50m in both of its width and height directions. The calculated temperature is interpolated to the nodes of finite element mesh for the calculation of effective viscosity. I also test the model with a finer grid with a half grid size. Although the solution gets more accurate compared with the one with a coarser grid used in this study, the test results shows that the overall pattern of solution is insensitive to the chosen grid size. The time step is controlled by the maximum heat production rate. That is, the higher the heat production rate is, the smaller the time step gets (e.g. *Thatcher and England, 1998*). I calculated the temperature evolution during 3 Myrs because the initiation age of active faulting in the inland area of Japan are mostly less than 3 Myrs (*Doke et al., 2012*).

2.3 Results

In this section, I first present the calculation results of shear stress, grain size distribution obtained by applying a 1-D linear geothermal gradient. I discuss the effect of different model assumptions on the deformation of the lower crust. Next, I show the temperature anomaly produced by shear and frictional heating. Finally, I show the effective viscosity structures obtained from all 6 cases in this study.

2.3.1 Shear stress distribution

Figure 6 shows distribution of the horizontal (a, τ_{xx}) and the vertical (b, τ_{yz}) shear stress in the lower crust for case W1E. The gray broken lines in these figures indicates depth of BDT. As shown in Figure 5, above the bottom of the BDTZ in the semi-brittle layer, the horizontal shear stress is no larger than few hundreds of MPa because the

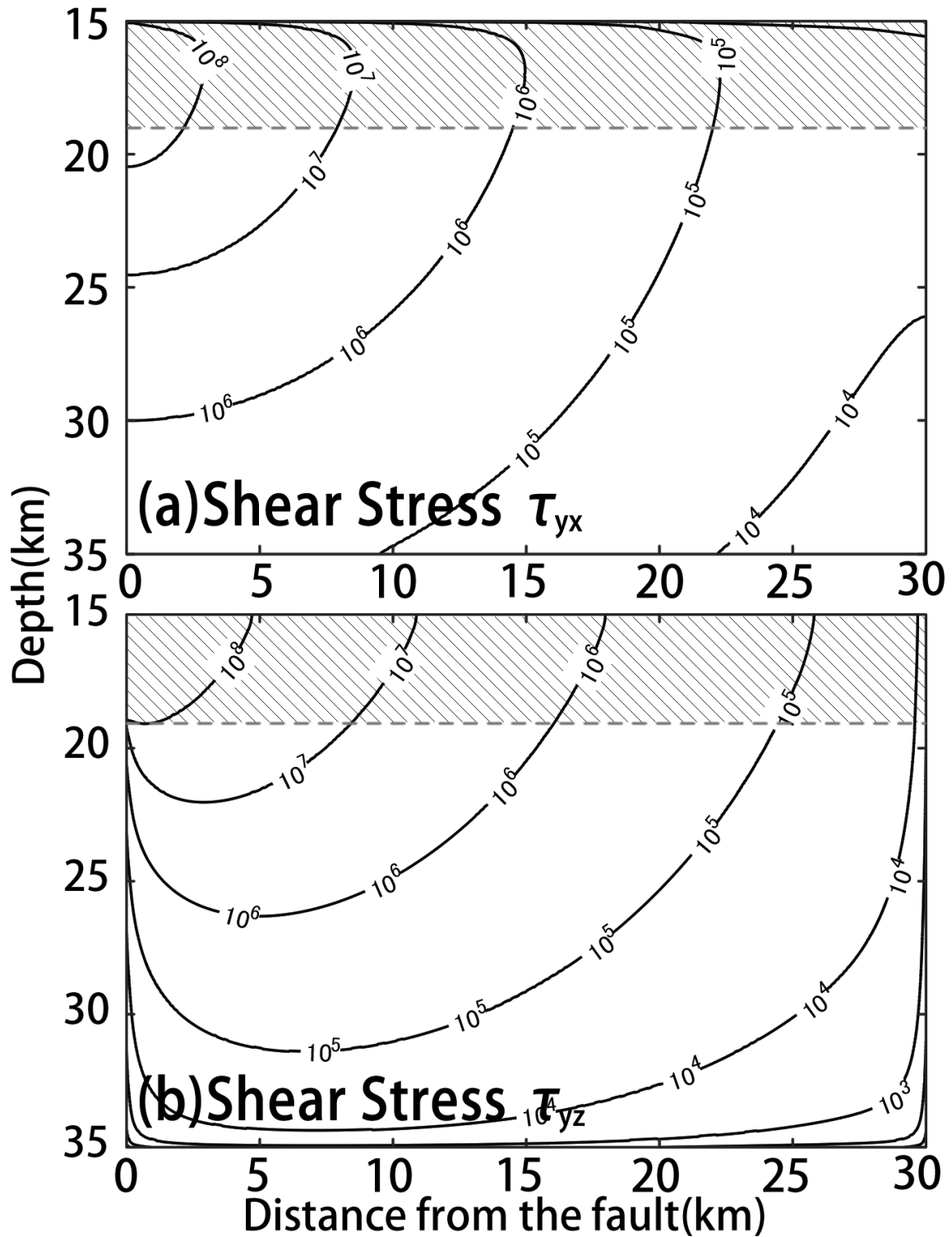


Figure 6: Contours of the horizontal (a, τ_{yx}) and the vertical (b, τ_{yz}) shear stress in the lower crust as a function of depth and distance from the fault for model W1E. The gray broken lines indicates the bottom of the BDTZ (Zhang and Sagiya, 2017).

shear stress τ_{yx} is limited by the fault strength. On the other hand, the vertical shear stress component (τ_{yz}) is larger than 700 MPa around $x = 0, z = z_b$ which results in a very large maximum shear stress there. The deformation in the semi-brittle layer right below the rigid upper crust is significantly influenced by the rigid upper crust through the imposed boundary conditions. This part behaves like rigid body because of its large effective viscosity ($> 10^{25}$ Pas) due to a low temperature. Because the elasticity is not considered in this model, all relative motions need to be accommodated as plastic flow, which results in such a large shear stress. As shown in Figure 5, τ_{yz} rapidly decreases with the depth. At the depths greater than the depth of BDT, τ_{yz} becomes negligible compared with τ_{yx} . Therefore, in the lower crust, the distribution of the shear stress is considered to be a result of far-field loading. In the following section, I focus our discussion to the lower crust below the depth of BDT.

Figure 7 shows the distribution of the shear stress in the lower crust for all the 6 cases (Table 1). In the lower crust, the shear stress decreases with depth and distance from the fault. The concentration of shear stress around the down-dip extension of the fault is a common feature that results from the assumption of a creeping strike slip fault in the upper crust. The magnitude of shear stress in the bulk of the lower crust depends on the model assumptions such as the rheology and boundary conditions. Compared with the wet anorthite cases (Figure 7a,d), the depth of the bottom of the BDTZ in the dry anorthite case is about 8 km deeper. The dry anorthite requires a higher temperature to achieve an effective viscosity that allows plastic deformation to occur with a relatively small shear stress less than few hundreds MPa. According to

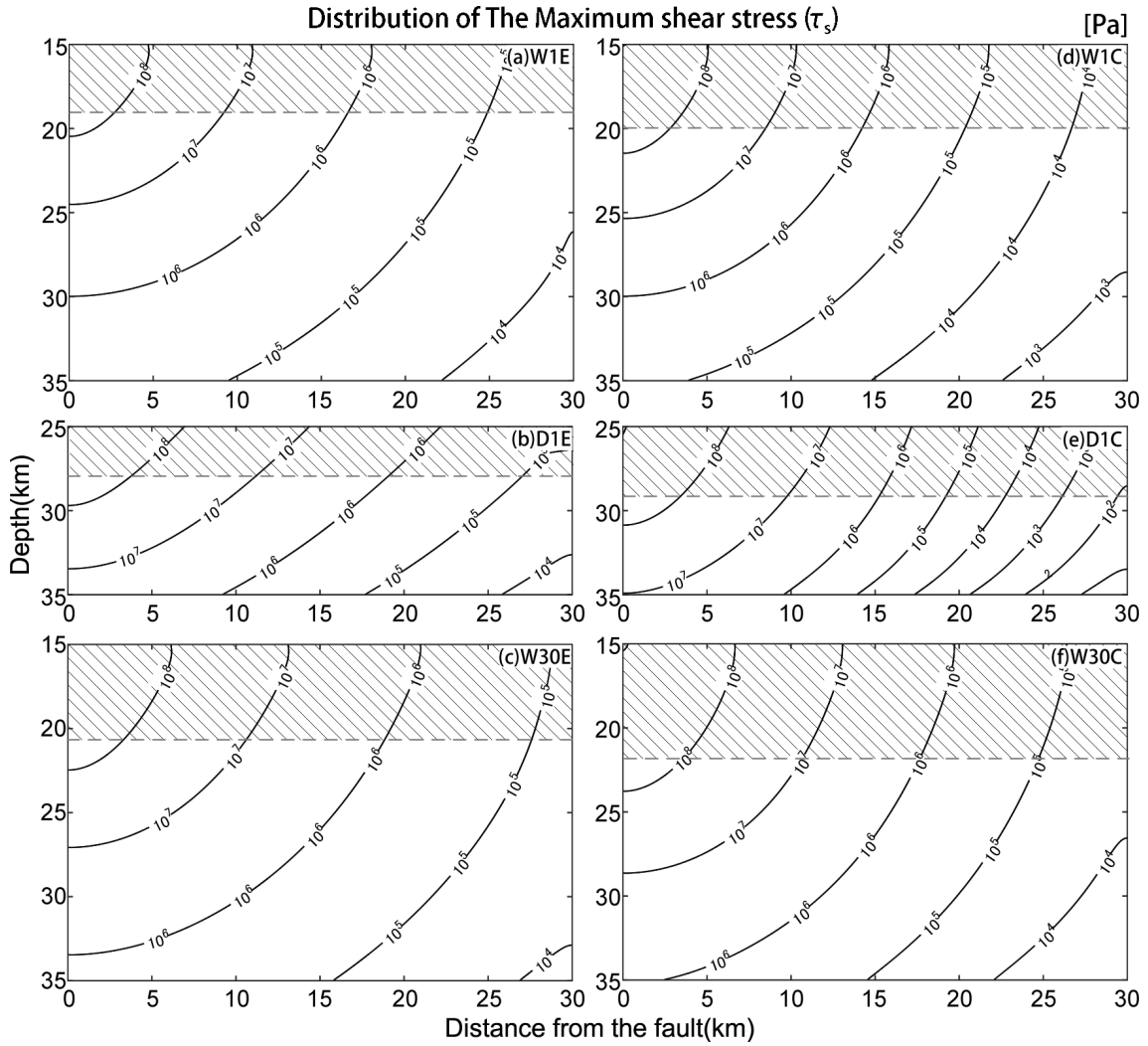


Figure 7: Contours of shear stress (τ_s) in the lower crust as a function of depth and distance from the fault for models (a) W1E, (b) D1E, (c) W30E, (d) W1C, (e) D1C, and (f) W30C. The thickness of the lower crust and the depth of the bottom of the BDTZ are dependent on the assumed rheology and far-field velocity (v_0). The gray broken lines indicate the bottom of the BDTZ (Zhang and Sagiya, 2017).

the depth of BDT, the z_b for dry anorthite was set at a depth of 25 km. In the interplate cases (Figure 7c,f), even though the slip rate is 30 times faster than the intraplate cases, the shear stress is only slightly larger, and the depth of the bottom of the BDTZ is only about 2 km deeper than its intraplate counterpart. These results indicate that the magnitude of the shear stress and the depth of the bottom of the BDTZ is not sensitive to the fault slip rate.

2.3.2 Grain size distribution

I have calculated the grain size L_e using Eq. 2.5. As examples, Figure 8 shows the distribution of L_e obtained in cases W1E and D1E with the initial temperature field. Fine grains are located in the region where deformation is localized because both L_e and shear strain rate depend on the temperature and shear stress (see Eq. 2.5 and Figure. 8). In our models, the grains are finest at the depth of the bottom of the BDTZ where shear stress becomes the largest in the lower crust. In cases W1E and D1E, the minimum grain size is $\sim 215 \mu\text{m}$ and $\sim 17 \mu\text{m}$ where the temperature is $\sim 475 \text{ }^\circ\text{C}$ and $\sim 700 \text{ }^\circ\text{C}$, respectively. Our results of L_e agree with the grain size measurements to show that the plagioclase grains in ultramylonites have a mean diameter of $16 \mu\text{m}$ (Okudaira *et al.*, 2015) and $85 \mu\text{m}$ (Okudaira *et al.*, 2017) under the condition of $\sim 700 \text{ }^\circ\text{C}$ and $\sim 600 \text{ }^\circ\text{C}$, respectively. Although the calculation results are generally in agreement with geological observations, the comparison between calculation and observation is not straightforward because the calculated grain size can vary with the physical conditions and model assumptions. For example, in the shear zone, the shear stress could be smaller than the calculation due to the weaker fault shear strength (Iio,

1997). Even though the physical conditions, such as temperature and stress, are similar to the real condition, the dynamically recrystallized grain size may be still larger than the calculated L_e (De Bresser *et al.*, 2001).

Field observations of naturally deformed rocks show that relatively coarse-grained (up to few centimeters) rocks are widely exposed over wide area outside of the shear zone (e.g. Markl, 1998). Generally, our calculation of L_e provides a fairly reasonable grain size distribution. However, in the far field, due to the low temperature and shear stress, unrealistic grain size larger than several centimeters appears. This may be ascribed to our assumption of grain size following the model of De Bresser *et al.* (1998). In this model, I did not consider the time for grain growth and physical mechanisms that limit the grain size, such as the Zener pinning effect (e.g. Hillert, 1988; Rohrer, 2010).

2.3.3 Temperature increase

Figure 9 shows the temperature increase during 3 Myrs after the initiation of shearing and fault sliding. In the cases of W1E and W30E with wet anorthite, the maximum temperature increases are about 15 and 219 °C, respectively. Due to the higher slip rate, heat generation in the interplate cases is more intensive compared to the intraplate cases. Because the fictional heating on the fault is very concentrated, the temperature rise in the crust is largely affected by frictional heating. On the surface, heat flow has a peak due to the fault friction. For interplate case W30E, the peak heat flow anomaly at the surface is elevated as much as $\sim 55 \text{ mW/m}^2$ than the background value of 65 mW/m^2 (Figure 10). On the contrary, for intraplate cases, the heat flow anomaly is

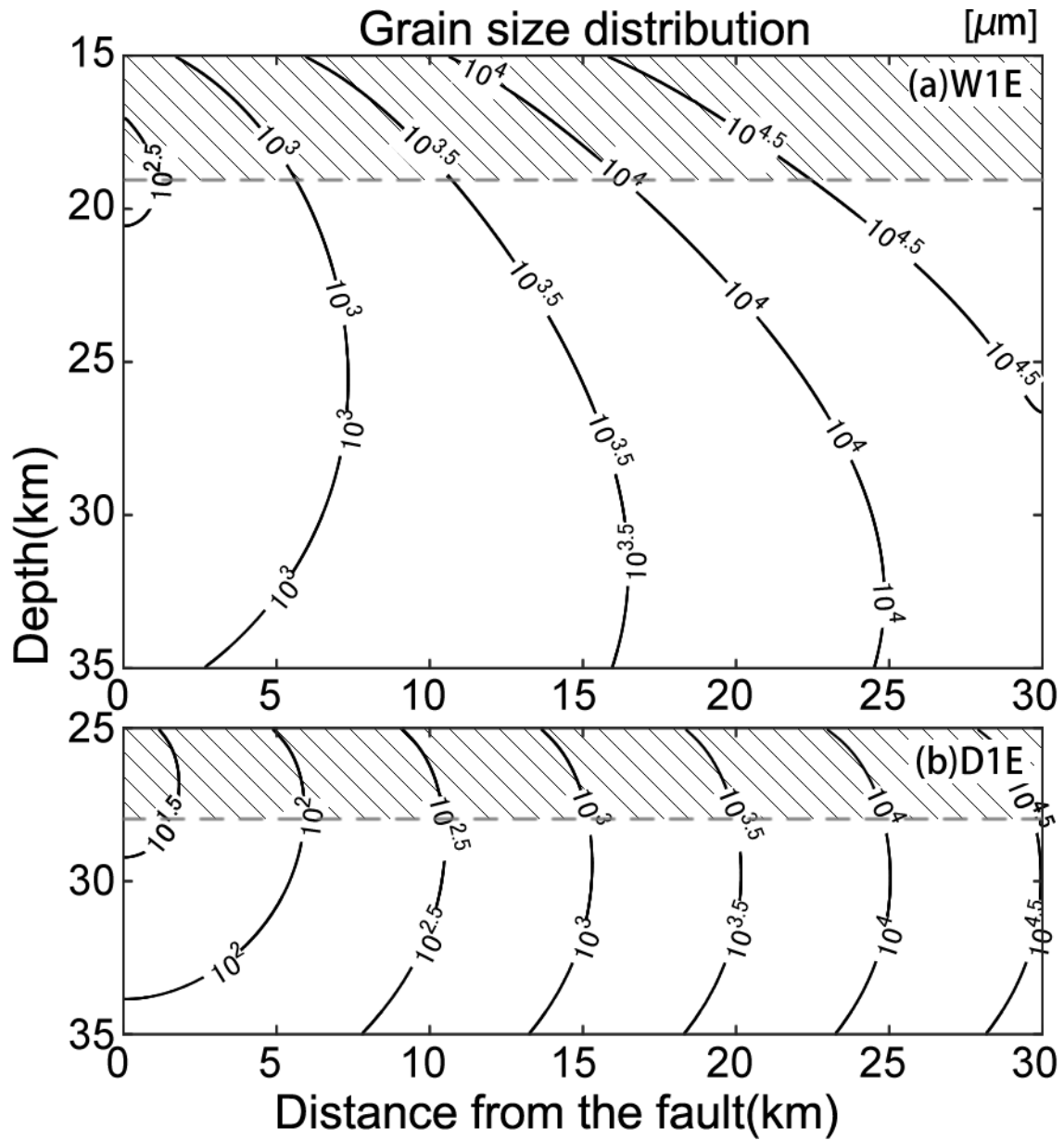


Figure 8: Contours of equilibrium grain size distribution as a function of depth and distance from the fault, calculated from case W1E (a) and D1E (b). The *gray broken lines* indicate the depth of the bottom of the BDTZ (Zhang and Sagiya, 2017).

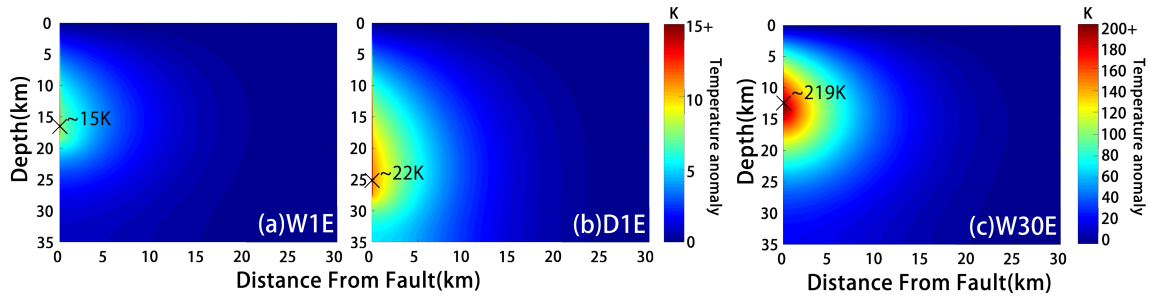


Figure 9: Temperature anomaly produced by shear and frictional heating versus depth and distance from the fault for models (a) W1E, (b) D1E and (c) W30E after 3 Myr of fault sliding. \times shows the location of maximum temperature increase; numbers indicate the magnitude of maximum temperature increase (*Zhang and Sagiya, 2017*).

very small, less than 5 % of the background value. Therefore, I cannot expect to detect a heat flow anomaly around intraplate strike slip faults (*Tanaka et al., 2004*).

To illustrate how rock rheology affects the heat generation rate, I also perform the same calculation using the rheological parameters of dry anorthite. Figure 9b shows the temperature increase for case D1E. The maximum temperature increase is about 22 °C which is higher than the case W1E. However, it is still insufficient to cause an observable heat flow anomaly at the surface.

2.3.4 Effective viscosity structure

Figure 11 shows the effective viscosity structure, which strongly depends on assumptions applied for calculation. For intraplate and interplate cases, the effective viscosity are $\sim 10^{22.5}$ Pas (Figure 11a,d) and $\sim 10^{21}$ Pas (Figure 11c,f) at the BDT, respectively. Because of the higher shear stress and shear strain rate, interplate cases have lower effective viscosity compared to the intraplate cases.

The effective viscosity of dislocation creep is very sensitive to the shear stress. The viscosity becomes extremely high when the shear stress is small. In the cases assuming

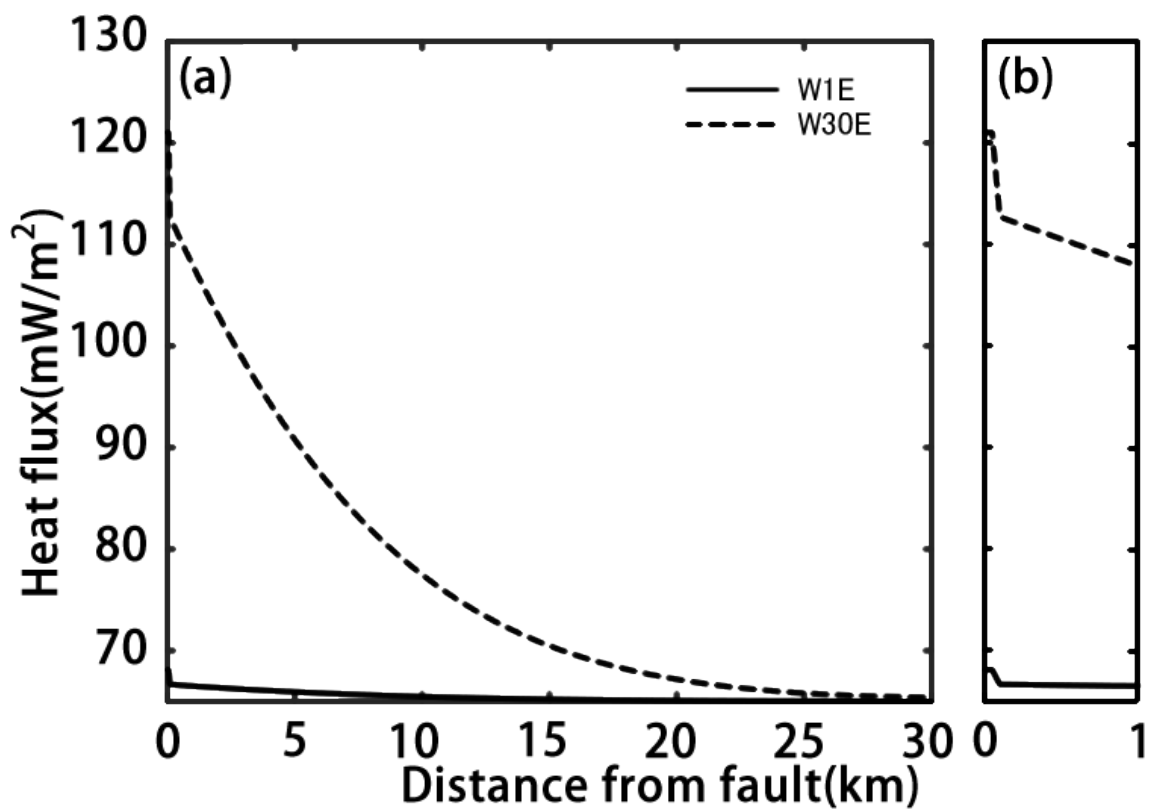


Figure 10: Surface heat flow for simulation of interplate (Dotted line) and intraplate (Solid line) strike slip fault, Sharp peak on top of the fault is created by fault frictional heating (*Zhang and Sagiya, 2017*).

EGS, the effective viscosity in the region with relatively small shear stress is significantly larger than that in the shear zone under the fault where stress is concentrated. This is because the same effective viscosity of dislocation and diffusion creep. In the region with relatively low temperature and small shear stress, the effective viscosity exceeds $\sim 10^{25}$ Pa s and materials behave like a rigid body.

On the other hand, in the cases assuming CGS, diffusion creep yields a smaller effective viscosity compared to the dislocation creep when shear stress is small. Therefore, the diffusion creep becomes a dominant mechanism in the far field. Because of the 1-D linear geothermal gradient, the effective viscosity in the far field has a layered structure. In the shear zone where stress is large, dislocation creep is dominant. The broken lines in Figure 11d-f indicate the location in which dislocation creep and diffusion creep with a constant grain size of 500 μm contribute equally to the deformation. On the left side of the broken lines, dislocation creep gives lower viscosity compared to the diffusion creep. Therefore, the deformation in the shear zone is dominated by dislocation creep.

The effect of water on the effective viscosity is shown by the comparison between the cases with wet and dry anorthite rheology. In the lower crust, the viscosity gets significantly smaller by the presence of water, which enables the plastic deformation at the depth between 20 to 25 km, whereas in the previous study of interplate strike slip fault (e.g. *Takeuchi and Fialko, 2012, 2013; Moore and Parsons, 2015*), due to the tremendous amount of heat generation, the temperature in the shear zone increases for a few hundreds of degrees. As a result, the effective viscosity in the center of the shear

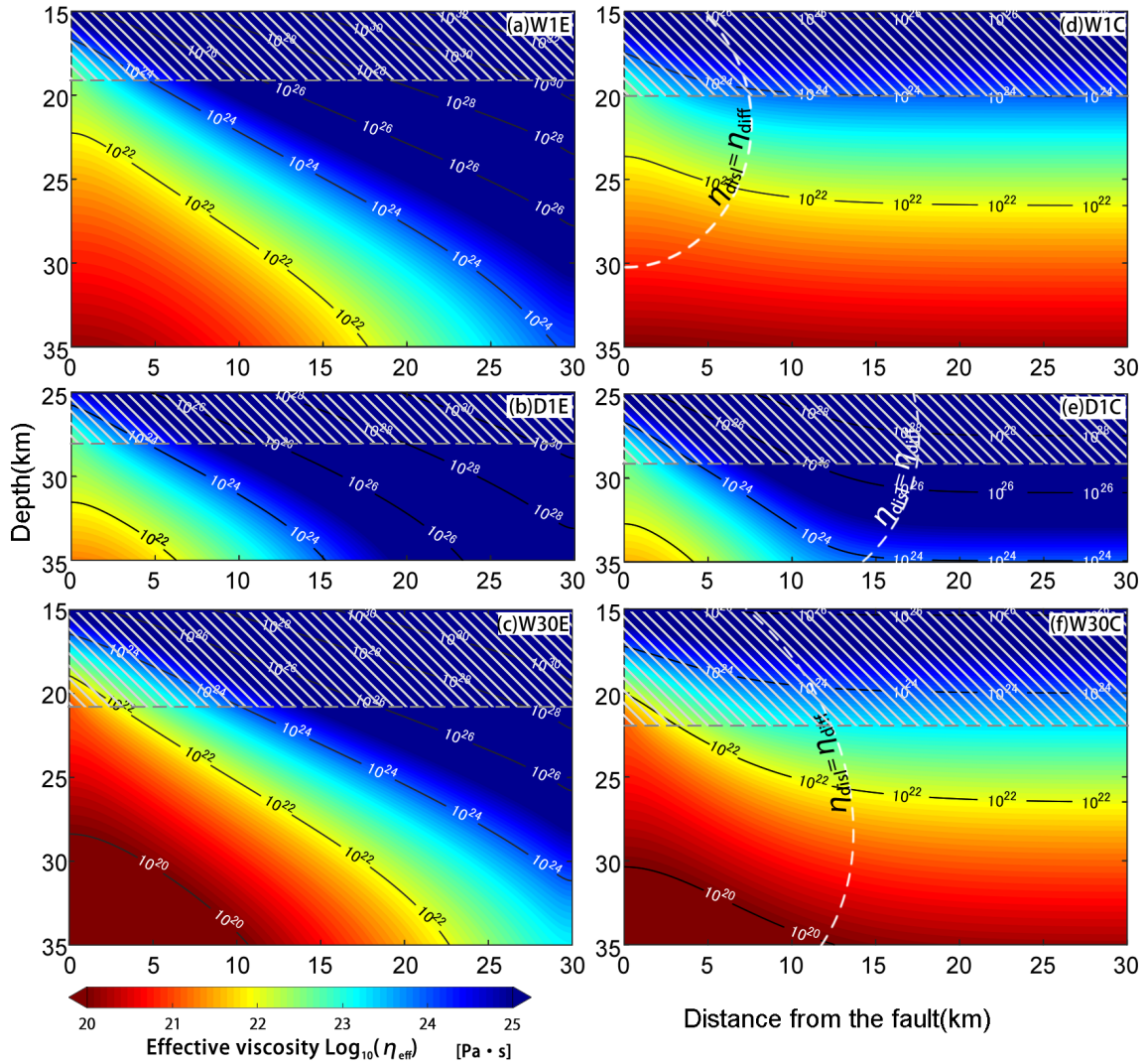


Figure 11: Effective viscosities versus depth and distance from fault for equilibrium grain size(a~c) and constant grain size(d~f). Broken line in d~f indicates the location where diffusion and dislocation creep has same shear strain rate (*Zhang and Sagiya, 2017*).

zone was similar in the case of wet and dry rheology. However, this is not same for in the intraplate cases, because heat produced by shear heating and frictional heating is too small and the temperature change is too small to change the effective viscosity structure.

2.4 Discussion

In this section, I discuss the relative importance of candidate mechanisms for the formation and maintenance of the lower crustal shear zone under an intraplate strike slip fault.

2.4.1 Comparison with thermo-mechanical model in previous studies

For interplate strike slip faults, such as the San Andreas Fault, discussed in previous studies (e.g. *Lachenbruch and Sass, 1980; Leloup et al., 1999*), shear, as well as frictional heating has been considered as a main cause of the formation of the lower crustal shear zone. To evaluate the effect of shear heating and friction heating, I compared the shear strain rate obtained from a temperature field at 3 Myr (solid contour in Figure 12) and that obtained from an initial temperature field (broken contour in Figure 12). In the interplate case W30E, there is a significant temperature increase around the fault tip at the depth of ~ 12 km (Figure 9c). The temperature increase in our model is consistent with the results of recent models of interplate strike slip fault (e.g. *Takeuchi and Fialko, 2012; Moore and Parsons, 2015*). Due to the increased temperature field, the effective viscosity gets significantly lowered after few millions

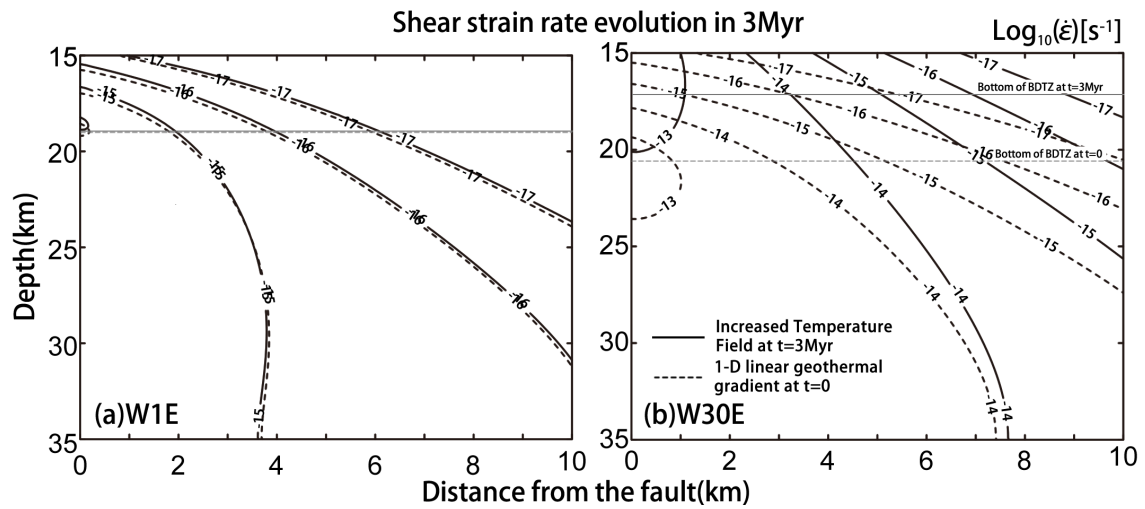


Figure 12: Shear strain rate changed by increased temperature for (a)W1E and (b)W30E, broken contour lines shows the shear strain rate with temperature field of 1-D geothermal gradient and solid contour lines shows the shear strain rate with temperature field from a 3Myr simulation (*Zhang and Sagiya, 2017*).

years. Compared to the shear deformation with 1-D linear geothermal gradient, the shear deformation is more concentrated and the depth of the bottom of the BDTZ gets shallower (Figure 12) with the temperature field at 3 Myr. This indicates that the deformation and the depth of the bottom of the BDTZ for an active interplate strike slip fault is time dependent.

On the contrary, for the intraplate case (Figure 12a), the change of shear strain rate during a time period of 3 Myrs negligible because the temperature increases minimal compared to the original temperature ($\sim 15\text{ }^{\circ}\text{C} / 400\text{ }^{\circ}\text{C}$). Therefore, for intraplate cases, shear and frictional heating effect on the thermal structure is negligible. I can conclude that the main cause of the formation of shear zone under intraplate strike slip faults is not the heating.

The absence of water in the crust can result in an increase of the heat generation

rate by shear heating and frictional heating. In the previous studies (e.g. *Takeuchi and Fialko, 2012; Moore and Parsons, 2015*), the temperature increases ~ 200 °C higher in the cases with dry rheologies than the cases with wet rheologies. In our study, heat generation rate is insensitive to the rock rheology because the shear stress and shear strain rate mainly depend on the boundary conditions of fault strength and far field velocity. Instead, the depth of the bottom of the BDTZ for the dry anorthite case becomes ~ 8 km deeper, which is equivalent to a temperature increase of ~ 200 °C, compared with the cases of wet anorthite.

2.4.2 Possible shear strain concentration mechanisms for shear zone under intraplate strike slip fault

In this model, the degree of shear strain concentration depends on the assumption of rheology. Compared to the case of Newtonian fluid (Figure 13c), deformation is more concentrated in the cases assuming a power law fluid (Figure 13a,b). In the shear zone, the shear strain rates for the cases W1E and W1C have similar distributions, which indicate that the assumption of grain size dose not affect the deformation in the shear zone. Therefore, I can conclude that, among the mechanisms considered in this study, weakening due to power law rheology is the most important mechanism for the formation of the shear zone in the lower crust.

In the fine-grained rocks, other mechanisms, such as grain boundary sliding (*Boullier and Gueguen, 1975; White, 1979*), could occur to further reduce the strength of materials and enhance shear strain localization. In the cases assuming EGS, only a small portion of the shear zone is composed of materials with such kind of small grain

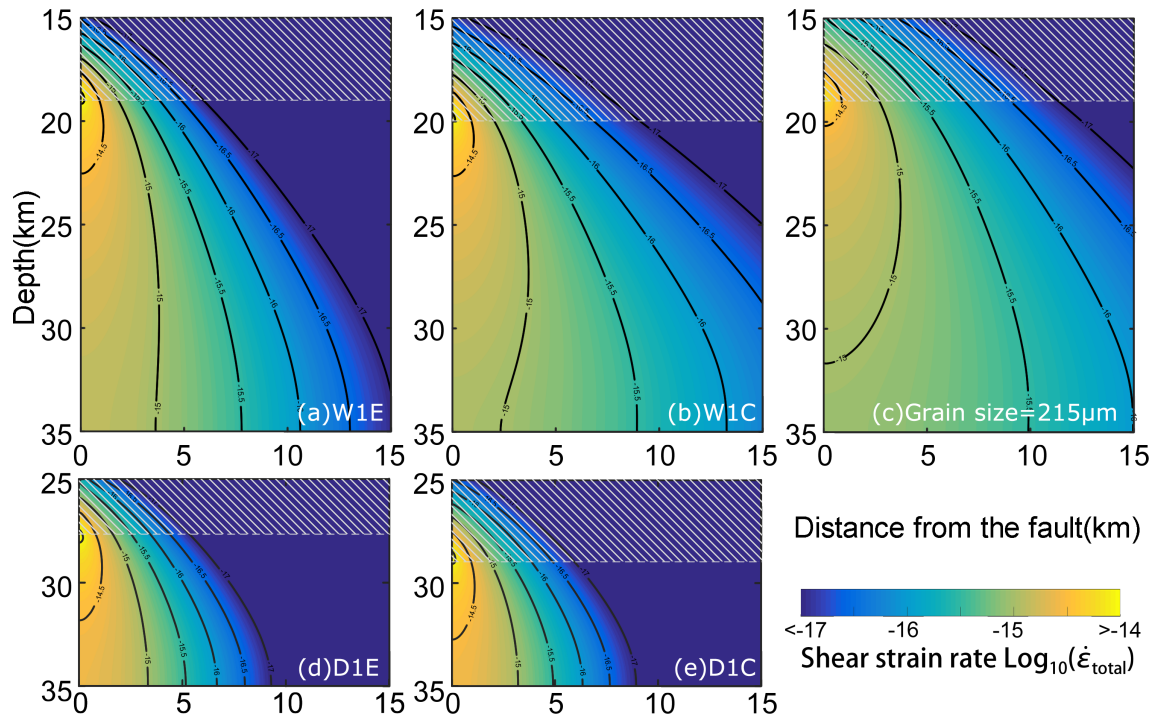


Figure 13: Shear strain rate for (a)W1E, (b)W1C (c)linear (d)D1E and (e)D1C. The grain size of linear case is a constant of 215 μm , minimum grain size in model W1E (Zhang and Sagiya, 2017).

size. Because the weakening effect of the grain size reduction dose not have a significant impact on the overall pattern of the plastic deformation in the lower crust, shear localization mechanisms other than grain size reduction is not considered in this study. Once a shear zone is formed in the lower crust, the grain size of the material in the shear zone gets smaller than its surroundings. The strength heterogeneity due to small grain size will remain over a geological time scale ($\sim 10^8$ years) due to the slow growth rate (Tullis and Yund, 1982). Mylonites found in an exhumed fault zone provide the evidence for the long-lived weak zones beneath intraplate strike slip faults. Because the mylonites are commonly observed in the earth's crust, lower plastic strength and strain localization in the lower crust, are common features for many

active faults.

In the far field, shear strain rate is larger in the case of CGS compared to that in the case of EGS. Despite differences in the far field, deformations in the localized shear zone are almost the same because the shear strain rate in the far field is much smaller than that in the shear zone.

2.4.3 Implication to the deformation of the lower crust

According to the model of *De Bresser et al. (1998)*, the evolution rate of grain size toward EGS depends on the shear strain rate. However, EGS in our calculation was assumed to be achieved instantaneously in this study, which may be an oversimplification and may not be realistic. Therefore, the calculated EGS can be considered as a result of long-term steady state deformation. Our results demonstrate that, strain localization can occur in the lower crust and the corresponding grain size distribution can be created no matter how slow the relative motion is across an intraplate strike slip fault. The model also predicts that rocks far away from a strike slip fault to behave like a rigid body. Studies of post-seismic deformation after the 1992 Landers and 1999 Hector Mine earthquakes indicates that viscoelastic deformation in the lower crust was not significant (*Pollitz, 2001; Freed et al., 2007*). Our results of the effective viscosity structures of the cases assuming EGS are in good agreement with such observations, because in those cases, the plastic deformation is limited in the narrow shear zone under the strike slip fault.

For interplate strike slip faults, a kinematic model with a buried dislocation in an elastic half-space has been proposed by *Savage and Burford (1973)*. This model can

be utilized to explain the geodetically observed interseismic deformation across the fault. A case study of the Atotsugawa fault (e.g. *Ohzono et al., 2011*) shows that elastic dislocation model can be also applied to intraplate strike slip faults and can give a reasonable estimate of the fault locking depth. The model in this study demonstrates that the localized deformation is possible even under an intraplate strike slip fault with a very low slip rate. This provides a physical basis for applicability of the *Savage and Burford (1973)* model to intraplate strike slip faults.

2.5 Conclusions

In this study, I have considered the formation and maintenance of the localized deformation under an intraplate strike slip fault. Models that incorporate laboratory-derived temperature-dependent power law rheology, grain size, and shear and frictional heating are examined to understand the mechanism and boundary conditions that influences the deformation of the lower crust. Water is very important to reduce the temperature requirement for plastic deformation in the lower crust, as for wet anorthite, deformation is fully plastic at temperature of ~ 475 °C, whereas for dry anorthite is ~ 700 °C. The temperature anomaly owing to 3 Myr of heat generation on an intraplate strike slip fault is negligibly small. In our model, dynamically recrystallized materials with small grain sizes are important for maintaining a shear zone on a geological time scale of $\sim 10^8$ years. The degree of shear strain is controlled by the weakening effect due to nonlinear relation between shear strain rate and stress (power law rheology) which is the most important mechanism in the development of the shear zone in the

lower crust.

Chapter 3

Evolution of intraplate strike slip fault and the shear zone under the fault

In this chapter, I introduce a new mechanical model consider earthquake cycles in the upper crust by assuming the entire crust is composed of a viscoelastic material. I investigate how repeating earthquakes affect the shear zone development in the lower crust under the fault and how localized deformation in the lower crust change the fault behavior. This chapter is based on the study of *Zhang and Sagiya (2018)*.

3.1 Introduction

It is widely accepted that a continental crust comprises an elastic upper crust overlying a ductile lower crust. The upper crust deforms in a elastic manner accompanied by earthquakes, while aseismic ductile flow occurs in the lower crust (e.g. *Sibson, 1982; Kohlstedt et al., 1995*). The upper and the lower crust deform in a different manner, which complicates the problem of crustal deformation. As I have shown in

Chapter 2, with a creeping fault in the upper crust, localized deformation appears in the lower crust. The degree of shear strain localization can further increase by shear strain mechanisms such as the power law rheology, grain size reduction and thermal weakening. Among these mechanisms, power law rheology is the most important mechanism that influences the deformation of the lower crust.

In this model, the upper crust is assumed to be two rigid blocks separated by a creeping fault to accommodate the relative motion. The lower crust is deformed by constant loading from the upper crust and the far field boundary. As a result, a localized deformation with high shear strain rate can be obtained in the lower crust under fault. In the geological time scale, the shear strain rate of the localized deformation can be increased by the heat generated in the lower crustal shear zone. Because of the imposed boundary condition between the upper crust and the plastic lower crust, the stress accumulation process and the evolution of the fault was not modeled properly. As the stress takes time to propagate in the material with nonlinear (power law) rheology (*Melosh, 1976*), it is important to understand the interaction between the upper crust and the lower crust and the process of shear zone formation in the lower crust.

Previous studies using a thermal-mechanical model to simulate the lower crustal deformation under the San Andreas fault (SAF) showed that steady state temperature and deformation under the fault can be reached in a few million years (*Thatcher and England, 1998; Leloup et al., 1999; Takeuchi and Fialko, 2012*), which is significantly shorter than the history of SAF that has been active over tens of millions of years (*Atwater, 1970*). In the recent few millions of years, estimation from global plate

motion model NUVEL-1A (*DeMets et al., 1994*) showed that the slip rate of SAF is stable (*DeMets and Dixon, 1999*), and is consistent with the geodetically observed slip rate (*Bourne et al., 1998*). For these reasons, the evolution of the stress and strain over multiple earthquake cycles were not considered in these thermal mechanical models.

On the other hand, the history of intraplate strike slip faults in the Japan island are much shorter compared to interplate strike slip fault (e.g. *Doke et al., 2012*). The geological estimation of slip rate on the intraplate strike slip fault are often slower than the geodetic estimations (e.g. *Ohzono et al., 2011; Herbert et al., 2014*). *Gourmelen et al. (2011)* interpreted this discrepancy as an evidence for the acceleration of an evolving strike slip fault. However, the mechanisms for such kind of fault slip acceleration are not clear.

For an immature intraplate strike slip fault, the degree of the shear strain concentration in the shear zone under the fault may be smaller compared to a mature interplate strike slip fault and the physical conditions and mechanical properties of the crust around the intraplate strike slip fault such as the shear stress and the temperature may change significantly in the geological time scales. Therefore, it is important to understand the evolution of physical quantities, such as the distribution of shear stress, effective viscosity, shear strain rate and shear strain, in the entire crust across the fault over geological time scales.

In this study, I construct a new mechanical model for intraplate strike slip deformation and earthquake cycle (Model 2). In this model, I consider deformation of a crust-upper mantle system. In order to understand the evolution of the shear stress

in the entire crust, the elastic deformation has been considered in the upper crust, I assume the entire model is composed of nonlinear Maxwell material whose plastic deformation is controlled by a power law rheology (Eq. 2.1). In the shallow part of the crust where temperature is low, the effective viscosity becomes extremely large and the Maxwell viscoelastic material behaves elastically. In the deeper part of the crust, where temperature is high, the effective viscosity becomes low enough for plastic deformation to occur. During the interseismic period, the lower crust behaves viscoelastically.

I calculate time variation of the shear stress, effective viscosity, shear strain rate and shear strain distribution and the fault behavior. I also show how distributions of these physical quantities are influenced by the model configurations such as the assumptions of rock rheologies and boundary velocities. Finally, I discuss how geodetic, geological and geophysical observations affect by a developing shear zone in the lower crust.

3.2 Model description

3.2.1 Model geometry

I consider deformation of the crust and mantle across a vertical strike slip fault as shown in Figure 14. I simulate earthquake cycles for a 2-D antiplane problem of an infinitely long strike slip fault. Because of the symmetric feature of the problem, only one side of the fault is considered. The model domain is 65 km (vertical, z coordinate) thick and 50 km wide (fault normal, x coordinate) rectangular regime, which is composed of a 35 km thick crust and a 30 km thick upper mantle. A horizontal boundary

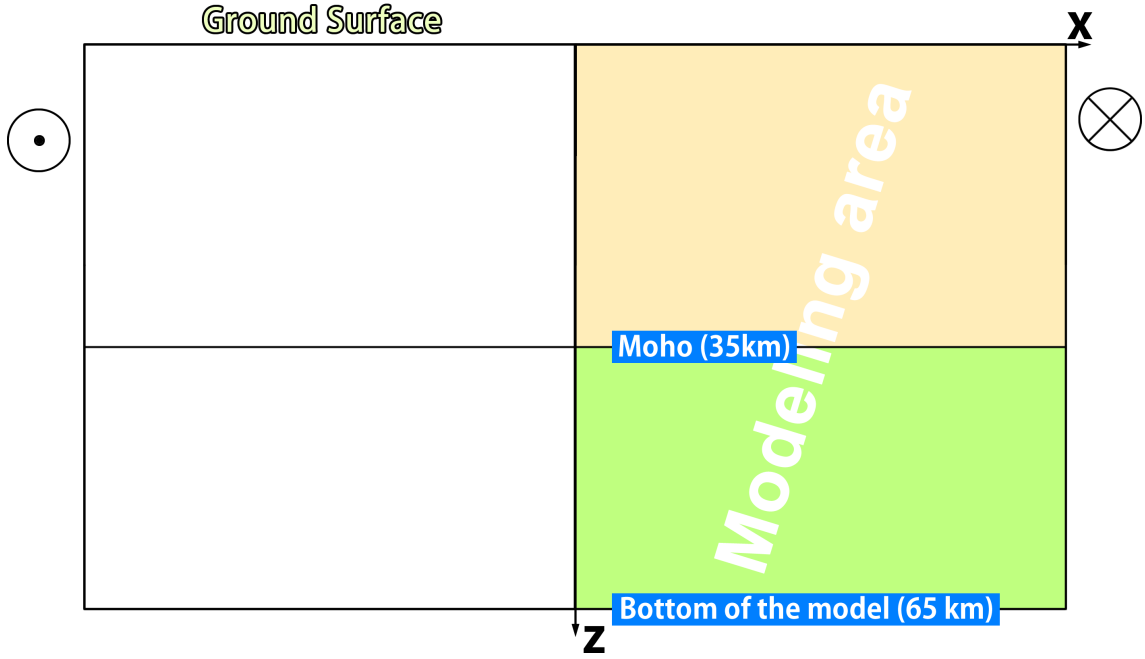


Figure 14: Geometry for model 2. Mohorovičić discontinuity (Moho) is a horizontal boundary at the depth of 35 km (*Zhang and Sagiya, 2018*).

at depth of 35 km represents the Moho discontinuity.

3.2.2 Temperature structure

The temperature structure used in this model is shown in Figure 15, which is considering the radioactive heat production in the crust (*Sclater et al., 1980*).

$$T(z) = \begin{cases} \frac{Q_r z}{k_1} + \frac{D^2 A_0}{k_1} \left(1 - \exp\left(-\frac{z}{D}\right)\right) & (z \leq h) \\ T(h) + \frac{z-h}{k_2} Q_r & (z > h), \end{cases} \quad (3.1)$$

where h is the depth of the Moho, k_1 and k_2 are the thermal conductivity of the crust and the upper mantle, respectively. Q_r is the heat flow at the base of the crust, D is degree of upward migration of the radiologic elements and A_0 is the heat production at the surface which is given by

$$A_0 = (Q_0 - Q_r)/D \quad (3.2)$$

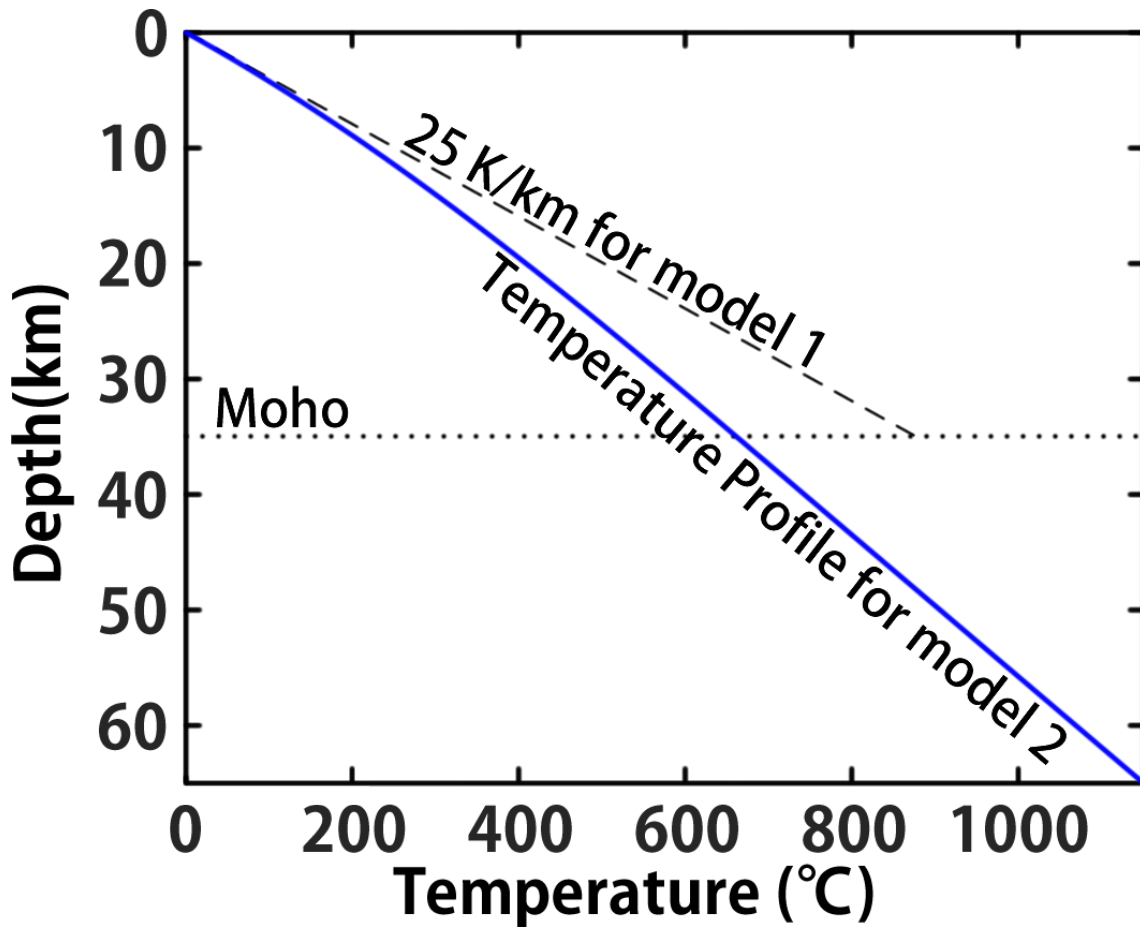


Figure 15: Temperature structure used in model 1 (broken line) and model 2 (Solid blue line). Geothermal gradient near Earth's surface are same in the model 1 and model 2. By considering the upward migration of the radiologic elements, in model 2, the temperature is lower in the deeper part of the crust compared to model 1.

where Q_0 (65 mWm^{-2}) is the heat flow on the ground surface (*Turcotte and Schubert, 2014*). Near the surface, the geothermal gradient is assumed to be 25 Kkm^{-1} . The thermal conductivity of the crust (k_1) can be calculated from Fourier's law of heat conduction i.e. $k_1 = \frac{Q_0}{dT/dz} = 2.6 \text{ WK}^{-1}\text{m}^{-1}$. k_2 is assumed to be $2.5 \text{ WK}^{-1}\text{m}^{-1}$. D can be solved from equations 3.1 and 3.2 with a fixed temperature boundary condition at the bottom of the model at 65 km, which is assumed to be $1150 \text{ }^\circ\text{C}$.

In this study, The effect of the shear and frictional heating is not considered in both

Table 4: Rheological properties of rocks from laboratory measurements

Rock Type		$\log A$	n	Q	m	r	V	Ref.
		[MPa ⁻ⁿ - τ μ m ^m s ⁻¹]		[kJ/mol]			[cm ³ /mol]	
Wet Quartz	disl. ^a	-4.9	3	242	0	1	0	<i>Rutter and Brodie (2004)</i>
Wet Anorthite	disl. ^a	0.2	3	345	0	1	38	<i>Rybacki et al. (2006)</i>
Wet Olivine	disl. ^a	3.2	3.5	520	0	1	22	<i>Hirth and Kohlstedt (2013)</i>

^a disl. denotes dislocation creep. ^b density of quartz, anorthite and Olivine are 2660, 2760, 3214 kgm⁻³, respectively.

intraplate and interplate cases. In the case of intraplate strike slip fault with a very slow slip rate, as I have discussed in Chapter 2, the heat generation has almost no influence on the intraplate deformation. On the other hand, in the case of an interplate strike slip fault, there is a considerable amount of heat generation, which affects the degree of shear localization in the lower crust. However, the time for the fault evolution in this study is less than ~ 1 million years. This duration is too short for dissipated heat to have a notable influence on the deformation around the fault. Therefore, the temperature structure is fixed in this study.

3.2.3 Rheologies

The entire model region is composed of nonlinear Maxwell viscoelastic medium, whose constitutive equation is described as follows:

$$\dot{\epsilon}^T = \dot{\epsilon}^v + \dot{\epsilon}^e = \frac{\tau}{\eta_{eff}} + \frac{1}{G} \frac{d\tau}{dt} \quad (3.3)$$

The total shear strain rate ($\dot{\epsilon}^T$) of the medium is represented as a sum of elastic shear strain rate ($\dot{\epsilon}^e$) and viscous strain rate ($\dot{\epsilon}^v$). G is the elastic shear modulus, which is assumed to be 30 GPa for both the crust and the upper mantle. The effective viscosity

(η_{eff}) is calculated from shear stress (τ) using the constitutive law of plastic flow (Eq. 2.1). The calculation method for the water fugacity is same as that in Chapter 2.

The crust is assumed to be composed of wet quartz (*Rutter and Brodie, 2004*) or wet anorthite (*Rybacki et al., 2006*) and the upper mantle is assumed to be composed of wet olivine (*Hirth and Kohlstedt, 2013*). As shown in Chapter 2, the plastic deformation in the lower crust is mainly controlled by grain size insensitive dislocation creep. Thus, in this study, I only consider the dislocation creep. The laboratory-derived parameters of experimental flow laws for dislocation creep are found in Table 4. Furthermore, I also test a case of stress independent linear rheology with a temperature dependent viscosity structure for comparison. Due to the lower temperature in this model compared to a constant geothermal gradient of 25 K/km in model 1 (Figure 15), plastic deformation dose not occur even in the deepest part of the crust if I assume dry rheologies. Therefore, the dry rheologies is not considered in this model.

3.2.4 Earthquake cycle model

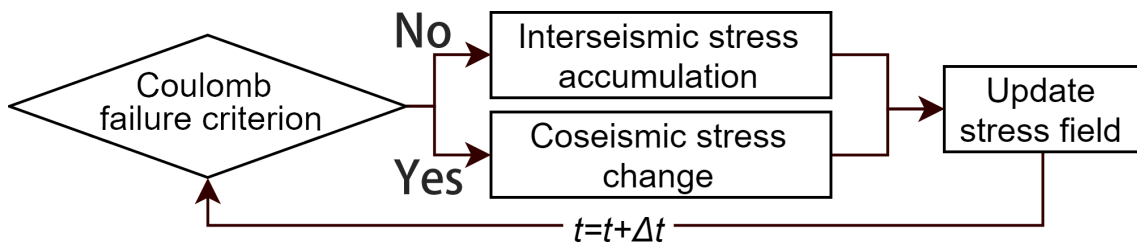


Figure 16: The algorithm for calculation of the earthquake cycle, both interseismic and coseismic stress change is solved using stress equilibrium equation (eq. 2.14) (*Zhang and Sagiya, 2018*).

The numerical simulations of this study starts from a stress-free initial condition and the lithostatic stress field $\sigma_n = \rho g z$ is applied for the entire model, where ρ is the

density of the rock which can be found in Table 4, g is the gravitational acceleration and z is the depth. The far field velocity v_0 at the vertical boundary 50 km away from the fault is assumed to be 0.5 mm/yr and 15 mm/yr for the case of an intraplate and an interplate strike slip fault, respectively. On the ground surface and the bottom of the model (65 km), the traction free condition, i.e., $\tau_{yz} = 0$, is applied. Shear stress in the bulk of the crust and the upper mantle evolves due to the far field loading. The shear stress on the fault is used to judge the occurrence of an earthquake (Figure 16). Frictional fault strength is described as follows

$$\tau_f = \mu_f \sigma_n + C_f \quad (3.4)$$

where μ_f is the coefficient of internal friction, which is assumed to be 0.2 and 0.6 in the case of a weak and a strong fault, respectively (Table 5). The frictional cohesive strength (C_f) is assumed to be 5 MPa.

During the interseismic period, stress change due to the far field loading is calculated for each time step to satisfy the stress equilibrium. In this calculation, the fault is locked, and no incremental displacement occurs at $x = 0$ km. The interseismic strain rate is assumed to be constant during each time step, and the elastic (viscous) strain change is calculated as a product of the elastic (viscous) shear strain rate and the elapsed time.

$$\tau_{ij}^{t_0+\Delta t} = \tau_{ij}^{t_0} + G \left(\dot{\epsilon}_{ij}^{t_0} - \frac{\tau_{ij}^{t_0}}{\eta_{eff}} \right) \Delta t. \quad (3.5)$$

which is the summation of the shear stress at t_0 ($\tau_{ij}^{t_0}$) and change of the shear stress. Δt is the adaptive time step, which is determined by the minimum effective viscosity of the entire model (η_{eff}^{min}) as $\Delta t = 0.1 \eta_{eff}^{min} / G$. The effective viscosity and the viscous

Table 5: Model configurations for the fault evolution process

Model	Crustal Rheology	fault coefficient	frictional	Boundary velocity (mm/yr)
Q1W	Wet Quartz	0.2		1
A1W	Wet Anorthite	0.2		1
Q1S	Wet Quartz	0.6		1
A1S	Wet Anorthite	0.6		1
Q30W	Wet Quartz	0.2		30
Q30S	Wet Quartz	0.6		30
Linear	Prescribed viscosity structure	0.2		1

^a Seven model configurations were tested by this study. The nomenclature of the model configuration is as follows: The first letter denotes rheological model (A, Anorthite; Q, Quartz). The rheological parameters for Anorthite and Quartz are summarized in Table 4. The last letter denotes fault strength (W, Weak; S, Strong). The number between two letters denotes the total relative velocity in mm/year.

shear strain rate calculated from stress at t_0 using Eq. 2.1. Total shear strain rate ($\dot{\epsilon}_{ij}^{t_0}$) can be solved from the stress equilibrium equation (Eq. 2.14). The shear stress in the bulk of the crust and the mantle at the next time step ($\tau_{ij}^{t_0+\Delta t}$) is calculated from the accumulated elastic strain (second term in the right hand side of Eq. 3.5).

On the fault, the shear stress increases until the Coulomb failure criterion (Eq. 3.4) is satisfied. In the coseismic period, a static stress drop is applied on the fault while the deep extension of the fault is locked. For all other boundaries, the traction free conditions, i.e., $\tau_{yz} = 0$ for the horizontal boundaries and $\tau_{yx} = 0$ for the far field boundary are applied. During the coseismic period, the entire crust and upper mantle behaves elastically, and the relationship between the change of the stress and the strain is linear.

$$\Delta\tau_{ij} = G\Delta\epsilon_{ij}^e. \quad (3.6)$$

Change of the elastic shear strain ($\Delta\varepsilon_{ij}^e$) are also solved from the stress equilibrium equation (Eq. 2.14). The stress boundary condition for the calculation of the stress change in the bulk of the crust and the upper mantle is given by the difference between stress on the fault in the previous step and the residual fault surface traction (black dotted line in Figure 17). After the brittle fracture in the elastic upper crust, stress concentration occurs near the crack tip (the deepest point of the rupture). As shown in Figure 17 (orange line), concentrated shear stress below the crack tip is significantly larger than the fault strength. Such kind of shear stress concentration should not exist near the fault tip after an earthquake. Therefore, I apply an iterative method to eliminate the stress concentration near the crack tip. The dark blue line is the stress on the fault before the first iteration. In each iteration, the stress drop boundary condition on the fault plane is determined by the shear stress on the fault after the previous iteration. The stress on the fault after each iteration is shown by other solid lines. The stress drop and the fault slip in each iteration become smaller. Iteration continues until the increment of the fault slip on the surface is less than 10^{-4} m. As a result of the iterations, the fault tip depth increases after each earthquake. In our simulations, several iterations are required for each earthquake. These iterations of the coseismic deformation are considered as an instantaneous process.

After several earthquake cycles, the rupture of an earthquake extends over the entire elastic upper crust. Starting from a stress free condition, I calculate the evolution of stress distribution until the appearance of a regular earthquake cycle, in which stress distribution does not evolve over each earthquake cycle any more. The brittle-ductile

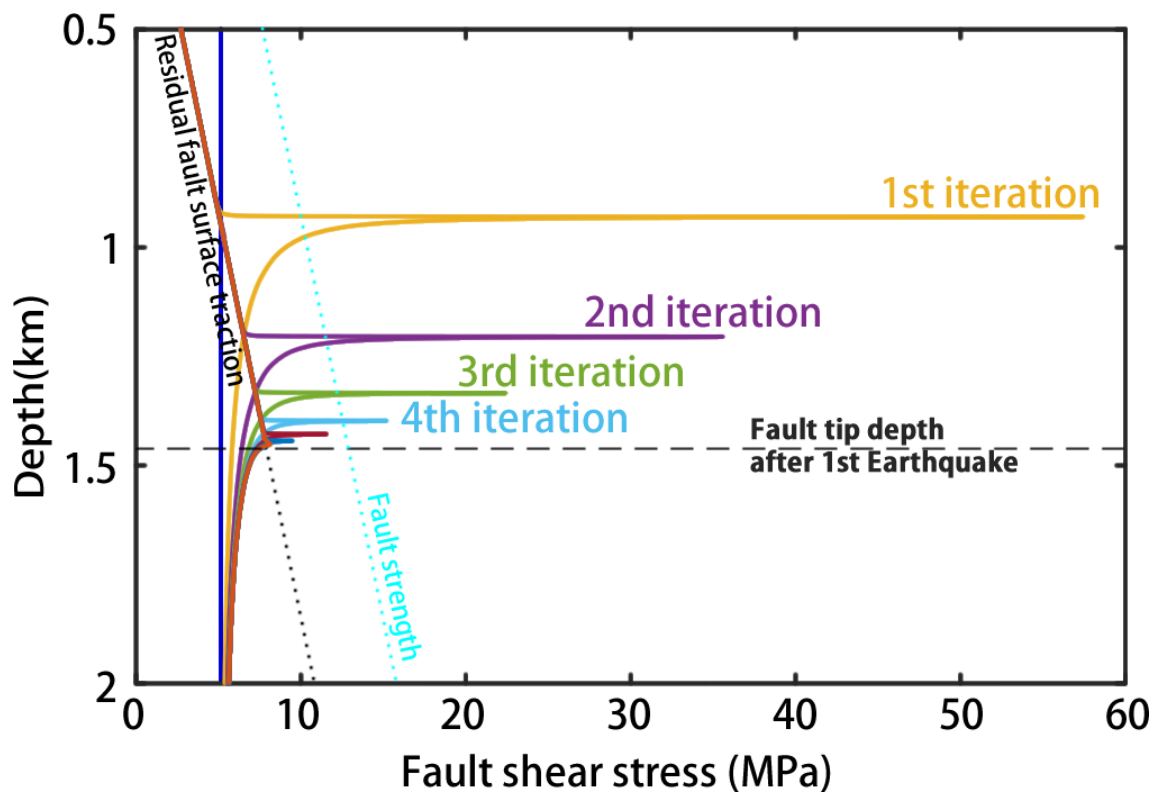


Figure 17: Stress concentration at the crack tip can be eliminated by several iterations. Time does not proceed in these iterations. The dark blue line is the stress on the fault before the first earthquake. Other solid lines are the shear stress on the fault after each iteration (*Zhang and Sagiya, 2018*).

transition zone (BDTZ) is a region on the fault where deformation mode gradually changes from fault slip to bulk deformation in the crust (*Kohlstedt et al., 1995*). Based on the definition of BDTZ, the depth of the BDTZ can be quantitatively estimated from the calculated coseismic offsets on the fault after the regular earthquake cycle started, which is almost a constant in the elastic upper crust. In this study, I tentatively define the boundary between BDTZ and the elastic upper crust at the depth where the modeled coseismic slip is 90 % of its maximum value at the surface. The boundary between BDTZ and the plastic lower crust is located at the depth where the coseismic slip becomes zero.

In this study, several different model configurations were considered. They are summarized in Table 5. The cases with a power law rheology are named in the following manner. The first letter indicates the rock type of the crust (A: Anorthite, Q: Quartz) and the second letter indicates the fault strength (W: $\mu_f = 0.2$, S: $\mu_f = 0.6$). The one or two digit number between two letters indicates the total relative velocity in the far field ($2v_0$) in mm/year. In addition, the case with linear Maxwell material is also considered for comparison. In the following sections, I refer to each case by the name shown in Table 5.

3.3 Results

In this section, I first present the spatiotemporal evolution of shear stress, effective viscosity, shear strain and shear strain rate around a strike slip fault. These results are snapshots at the end of the interseismic period in earthquake cycles. Next, I show how

the fault behavior changes in time by showing results on the fault plane including the stress accumulation rate averaged over different cycles, the shear stress distribution at the end of the interseismic period and the coseismic slip. Although, there are 7 different cases (Table 5), only Q1W is used to demonstrate the evolution process because all other cases are somehow similar. However, because the distributions of shear stress, viscous shear strain rate and effective viscosity depend on model configurations, I show the results for all 7 cases and compare them.

3.3.1 Shear stress evolution

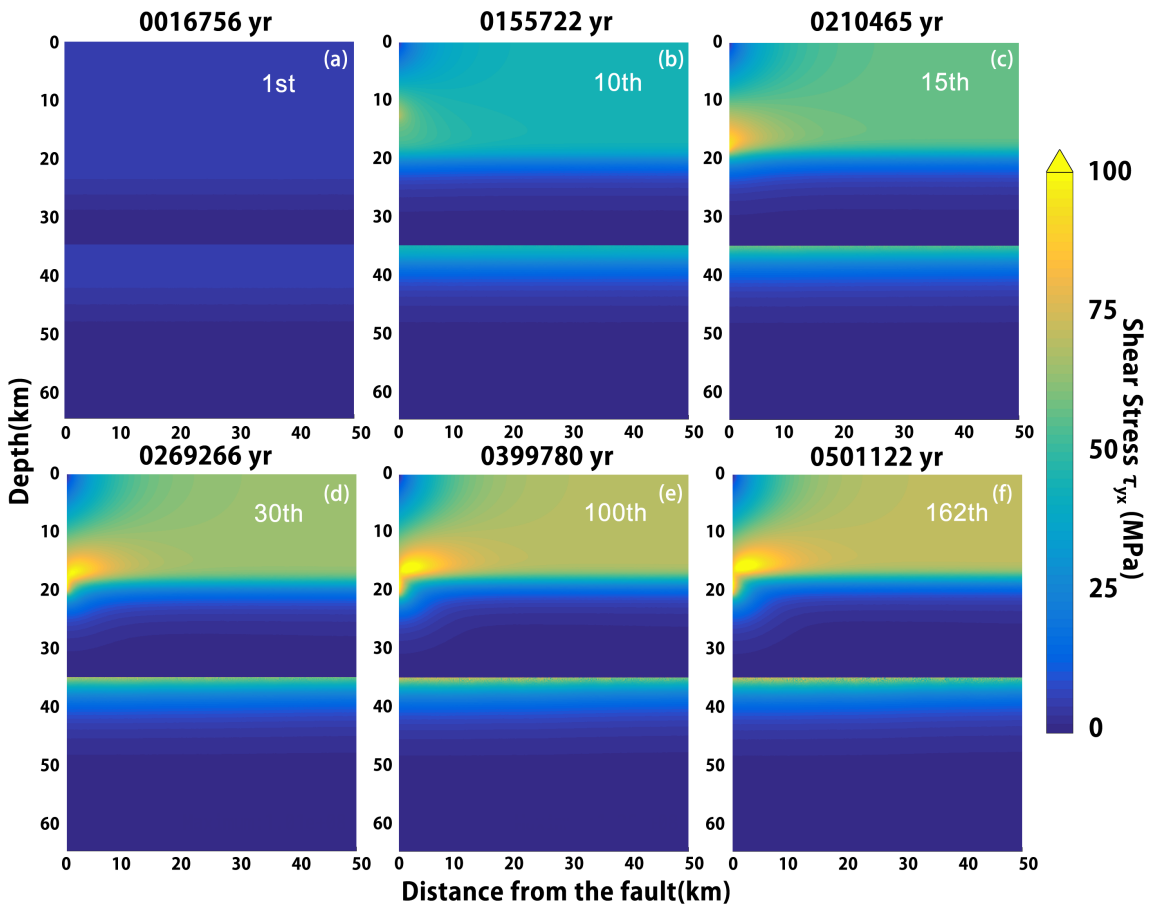


Figure 18: Shear stress τ_{yx} evolution in the model of Q1W, each figure is plotted right before an earthquake, the number of earthquake cycle is shown in each figure and the elapsed time is shown on the top of each figure (Zhang and Sagiya, 2018).

The shear stress evolution of the model Q1W is shown in Figure 18. At the beginning when the entire model is unstressed, the stressing rate in the crust and the upper mantle are constant due to the constant far field boundary velocity. Because the effective viscosity is inversely proportional to the shear stress with a power of $n - 1$ ($n = 3$), at the beginning when shear stress is very low (Figure 18a), the entire crust and upper mantle behave elastically. In the elastic upper crust, the shear stress increases at a constant rate of ~ 300 Pa/year until the fault cohesive strength (5 MPa) is reached. In the lower crust where temperature is higher, stressing rate decreases to zero as the dominating deformation mode changes from elastic to plastic. As earthquakes repeat, the degree of stress localization around fault tip increases after each earthquake. Figure 18b shows the shear stress distribution before the 10th earthquake at ~ 0.15 Myr. The shear stress near the fault tip at the depth of 15km is ~ 70 MPa, which is ~ 20 MPa higher than the stress in the bulk of the crust far away from the fault. As I showed in Figure 17, the fault tip depth increases after each earthquake. At ~ 0.21 Myr after the 15th earthquake (Figure 18c), the fault tip reaches the BDTZ. After that, the shear stress variation over earthquake cycles becomes smaller. From ~ 0.21 Myr to ~ 0.27 Myr, the maximum value of the shear stress increases by 4.7 MPa (Figure 18d). It is much smaller than the increase of the maximum value of shear stress from ~ 0.15 Myr to ~ 0.21 Myr, which is 24.4 MPa. The shear stress eventually stops evolving around 0.40 Myr and a regular recurrence of earthquake starts (Figure 18e and 18f).

In the bulk of the crust and the upper mantle, the shear stress gradually evolves with time until it reaches ~ 70 MPa after the regular recurrence starts. In the far field,

the shear stress is almost uniform and reaches ~ 70 MPa near the ground surface. Such kind of large shear stress is unrealistic because the rock strength in the shallower part of Earth's crust is small compared to the calculated shear stress (e.g. *Hallbauer et al., 1973; Barton, 2013*). This results from our assumptions of the constant far field velocity and elastically deforming upper crust. In our model the upper crust behaves elastically because of the extremely high effective viscosity in the low temperature environment. In reality, however, plastic deformation occurs in the shallower part of the crust when shear strength of the rock is reached. This problem will be further addressed in Chapter 4.1.

3.3.2 Evolution of effective viscosity

The evolution of effective viscosity in case Q1W is shown in Figure 19. The effective viscosity decreases with the increase of the shear stress. Before the fault start to have influence on the shear stress distribution in the lower crust and the upper mantle, the effective viscosity has a layered structure due to the depth dependent temperature (Figure 19a and 19b). At the depth shallower than 20 km, the effective viscosity is larger than $\sim 10^{24}$ Pas. Because the relaxation time ($t_r = \eta_{eff}/G$) for such high effective viscosity material is longer than the total elapsed time in these simulation, which is about 1 million years, the effective viscosity in the depth shallower than 20 km is almost unchanged by the process of shear stress concentration. At the depth of 35 km, there is a large effective viscosity jump across the Moho. The effective viscosity in the shallowest part of the upper mantle is 2-3 orders of magnitude larger than that in the deepest part of the lower crust.

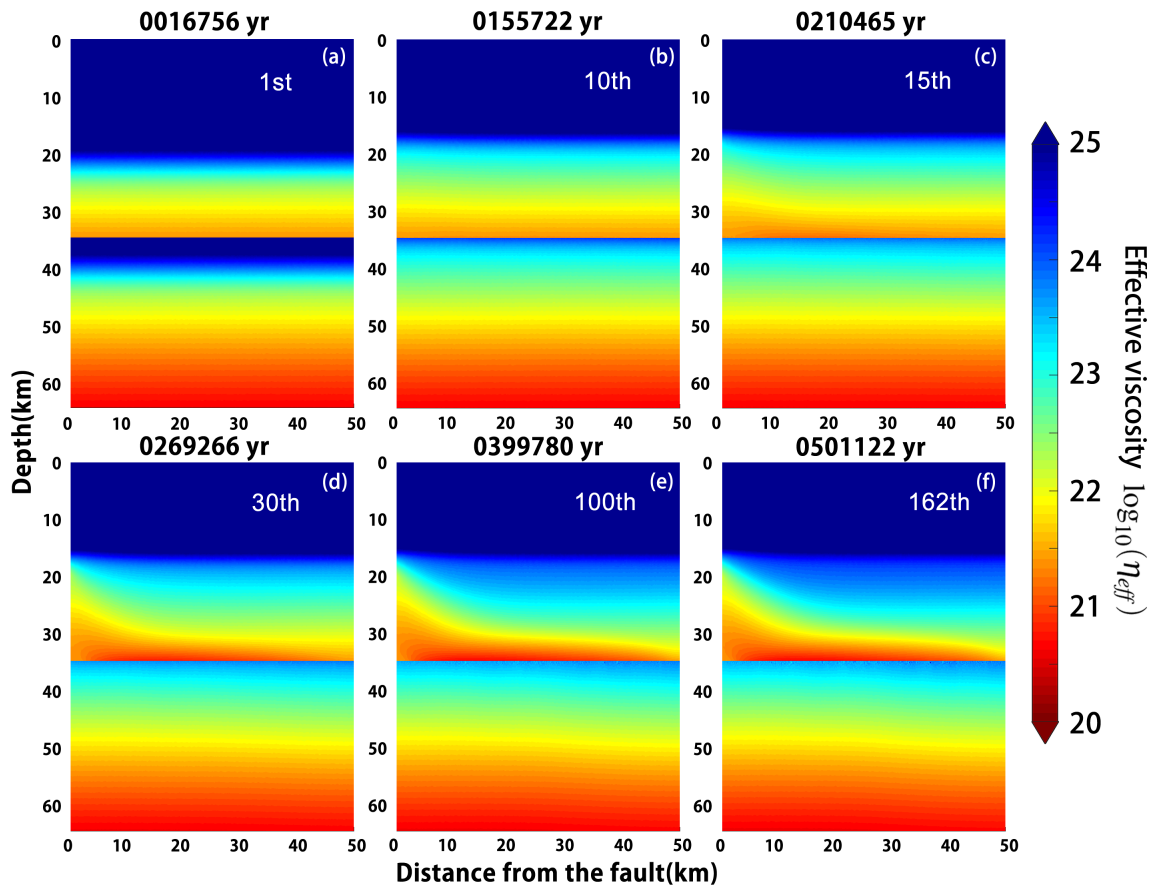


Figure 19: The effective viscosity η_{eff} evolution in the model of Q1W, each figure is plotted right before an earthquake, the number of earthquake cycle is shown in each figure and the elapsed time is shown on the top of each figure (*Zhang and Sagiya, 2018*).

As the fault tip gets closer to the lower crust, due to the stress concentration near the fault tip, the effective viscosity there starts to drop. In case Q1W, the fault tip depth increases until it reaches a depth of 20.4 km (Table 6). In the 10th earthquake cycle, the effective viscosity at the depth of 20.4 km is $\sim 10^{23.2}$ Pas. In the process of the shear stress concentration, the effective viscosity near the fault tip decreases by about a factor of 10. Meanwhile, in the far field at the depth between ~ 20 km and 30 km, the effective viscosity increases by about a factor of 10 due to the reduced shear stress. Thus, at same depth, an effective viscosity contrast of a factor of up to ~ 100 develops in the lower crust. In the deepest part of the lower crust, due to the basal drag from the upper mantle layer, the vertical component of shear stress (τ_{yz}) increases and the effective viscosity decreases. Generally, in the lower crust under the fault, the effective viscosity becomes smaller toward the deeper extension of the fault and in the far field. And in the far field, the depth dependence of the effective viscosity remain unchanged. After the regular recurrence starts, the viscosity structure does not change after each earthquake cycle. The effective viscosity structure at 0.4 Myr (Figure 19e) is identical to that at 0.5 Myr (Figure 19f).

3.3.3 Evolution of the plastic deformation rate

The deformation of the lower crust and the upper mantle is dominated by plastic deformation due to their lower effective viscosity. Figure 20 shows the evolution of the plastic deformation ($\dot{\epsilon}_{yx}$ component) in the case of Q1W. Before the fault tip reaches the lower crust, the deformation of the lower crust and the upper mantle is dominated by a laminar flow in which the viscous shear strain rate is about 10^{-16} s $^{-1}$ (Figure

19a and 19b). The concentration of deformation and the shear stress starts at the same time at 0.2 Myr when the fault tip gets closer to the lower crust. Meanwhile, the shear strain rate in the far field of the lower crust starts to decrease. Under the elastic upper crust at the depth between 17 km and 20 km, there is a thin layer where the shear strain rate does not change from the 10th earthquake. Due to the extremely high effective viscosity and long relaxation time, stress accumulated by the far field loading cannot be relaxed in our calculation.

The degree of the strain concentration is significantly smaller in the upper mantle compared with that in the lower crust. Due to the small effective viscosity in the deepest part of the lower crust, there is a vertical decoupling between the crust and the mantle. Therefore, the fault in the upper crust can significantly affect the lower crust, but its effect is negligible in the upper mantle.

3.3.4 Evolution of shear strain

The cumulative shear strain from case Q1W is shown in Figure 21. In the upper crust where elastic deformation plays a dominating role, the shear strain distribution shares the same characteristics with the shear stress distribution due to the linear relationship between shear strain and shear stress. In the lower crust, the distribution of shear strain is a temporal integration of the viscous shear strain rate (Figure 20). Before the fault reaches the BDTZ at 0.2 Myr (Figure 21b and 21c), the shear strain is very small, and the maximum shear strain near the fault tip does not exceed 10^{-2} . After the regular earthquake recurrence started, the shear strain starts to accumulate rapidly in the lower crust under the fault due to shear strain localization. As a result, the distribution of

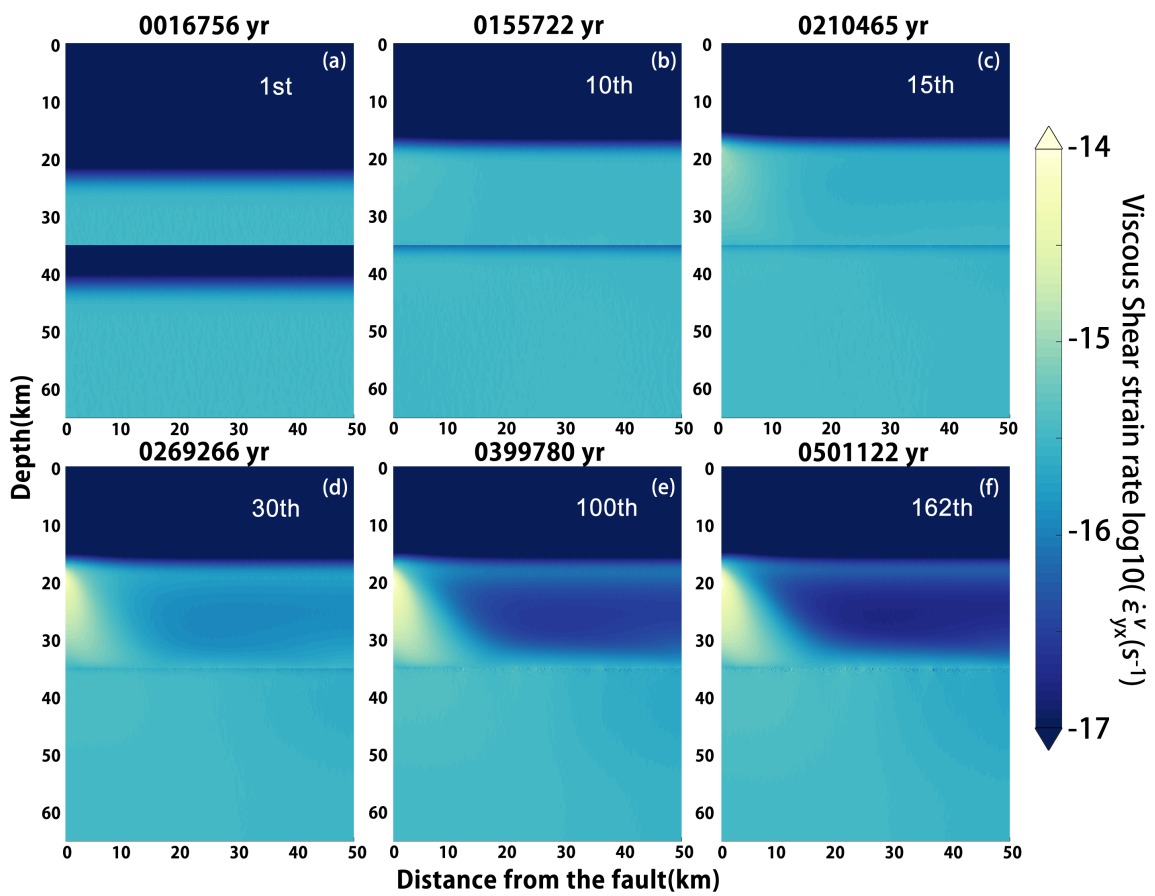


Figure 20: The viscous shear strain rate $\dot{\epsilon}_{yx}$ evolution in the model of Q1W, each figure is plotted right before an earthquake, the number of earthquake cycle is shown in each figure and the elapsed time is shown on the top of each figure (*Zhang and Sagiya, 2018*).

shear strain in the lower crust has a similar pattern as the distribution of shear strain rate shown in Figure 20.

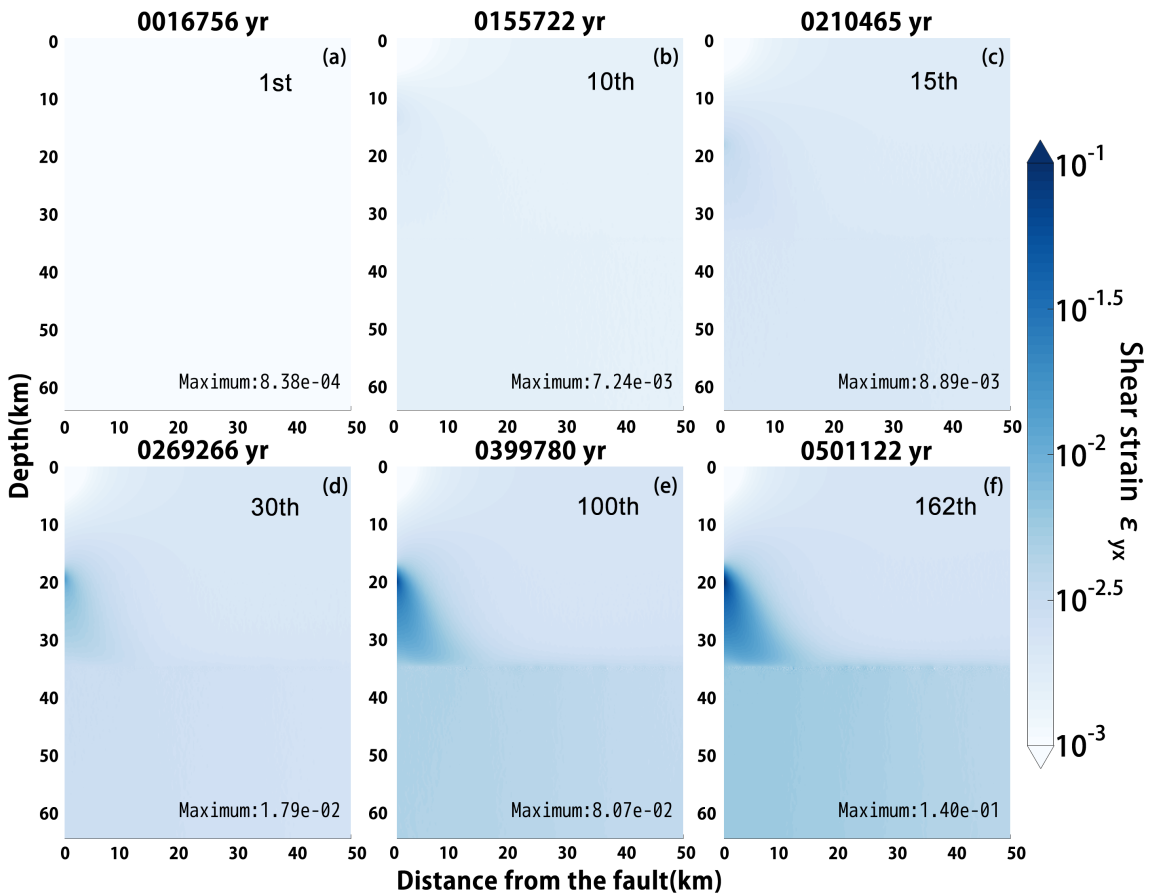


Figure 21: The cumulative shear strain ϵ_{yx} in the model of Q1W, each figure is plotted right before an earthquake, the number of earthquake cycle is shown in each figure and the elapsed time is shown on the top of each figure (Zhang and Sagiya, 2018).

Between the crust and the upper mantle, there is a clear discontinuity. This is because there is almost no concentration of deformation in the upper mantle. On the other hand, in the crust, there is no obvious boundary between the upper and the lower

crust because the same material has been assumed for the entire crust and there is a seamless transition occurs from elastic to plastic behavior in the BDTZ. In the far field, the shear strain in the entire crust is almost uniformly distributed. At 0.5 Myr, the shear strain in the far field reaches $\sim 2.5 \times 10^{-3}$, which is significantly smaller than the maximum value in the center of the shear zone which is $\sim 1.4 \times 10^{-1}$. The shear zone in the lower crust develops with time in the following few million years. As the development continues, the shear strain accumulates and the localized shear deformation is expected to be recognizable as a shear zone.

3.3.5 Evolution of the fault behavior

The fault behavior changes with the process of the tectonic stress evolution. I show the behavior of the fault in different earthquake cycles by showing the evolution of the averaged interseismic stressing rate (Figure 22a) and shear stress (Figure 22c) across the fault surface and coseismic offsets distribution in an earthquake (Figure 22b).

Before the shear stress on the fault reaches the cohesion strength of 5 MPa, the shear stress in the entire crust is very small. Due to the high effective viscosity of the materials with low shear stress, the entire crust behaves elastically. The shear stress accumulation rate in the lower crust is the same as that in the upper crust. In the first interseismic period, shear stress accumulates from zero with a nearly constant rate of 300 Pa/yr due to the far field loading. After a few earthquake cycles, the shear stress stops increasing in the plastic lower crust. As the shear stress in the elastic upper crust increases, the crust with a higher strength in the deeper part of the elastic upper crust starts to break. In the 10th earthquake cycle (green lines in Figure 22a), the earthquake

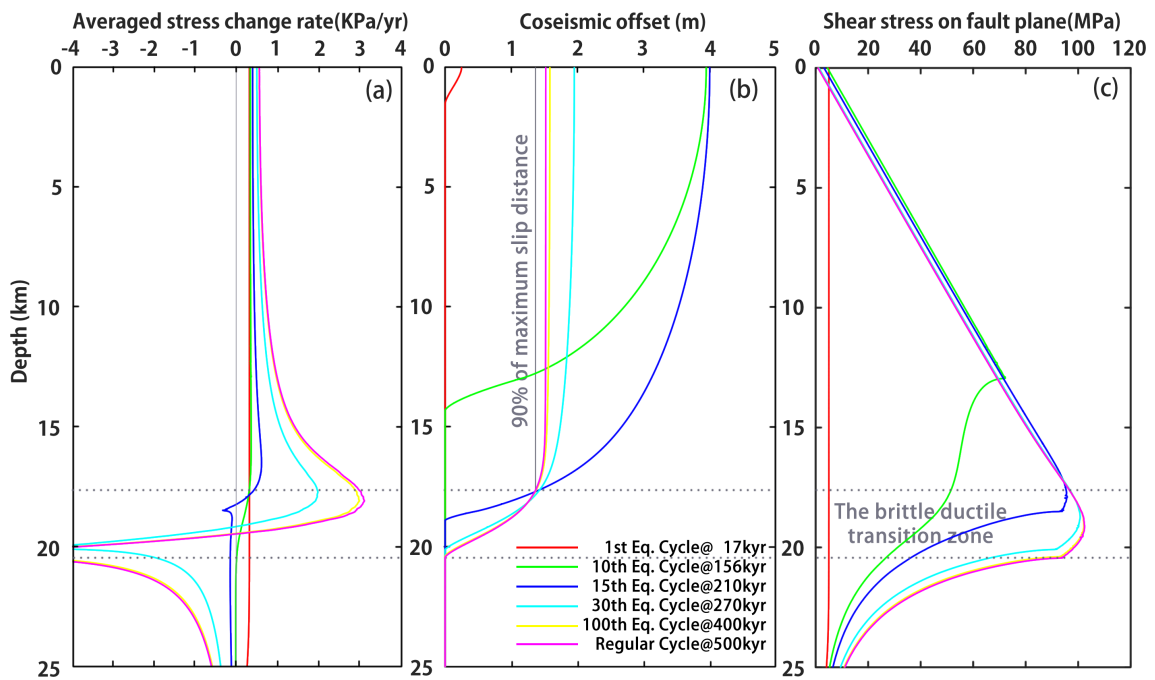


Figure 22: Stress change rate averaged over an earthquake cycle (a), coseismic offset (b) and shear stress on fault plane right before an earthquake (c). Lines with different colors indicate the result from earthquakes at different time. The gray broken lines indicate the depth of BDTZ (Zhang and Sagiya, 2018).

breaks through a large portion of the elastic upper crust. Before the rupture reaches the deeper part of the upper crust, the stressing rate in the upper crust is nearly a constant. In the case of the 10th earthquake cycle, the stressing rate is larger than the initial value by 20 to 40 Pa/yr. The increase of the stressing rate in the elastic upper crust is a result of a basal drag from the plastic deformation of the lower crust. After the rupture reaches the BDTZ, the stress starts to decrease in the shallower part of the lower crust due to the stress relaxation during the interseismic period. As the fault tip gets closer to the lower crust, the stress relaxation in the lower crust becomes stronger and the basal drag becomes more intense after each earthquake. Due to the effect of the basal drag, the averaged interseismic stressing rate significantly increases around the upper boundary of the BDTZ. The stressing rate in the shallower part of the upper crust is also affected by the basal drag, though the stress perturbation is smaller than that near the upper boundary of BDTZ. After the regular recurrence starts, the maximum shear stressing rate at the depth of ~ 18 km is ~ 3 kPa/yr, which is 6 times larger than that on the surface (~ 500 Pa/yr). The coseismic offsets on the ground are ~ 0.76 m which is roughly equal to the far field travel distance during the 1.54 kyr long interseismic period. For other cases, the coseismic offsets and the length of the interseismic period after the regular recurrence started are summarized in Table 6.

Because the fault is mainly loaded by the basal drag, the coseismic offsets are almost constant in the elastic upper crust. In Figure 22, gray broken lines indicate the upper and the lower boundaries of the BDTZ. In the case of Q1W, the depth of BDTZ ranges from 17.6 km to 20.4 km. I estimate the depth of all the cases in this study.

Table 6: Model properties after regular recurrence starts

Model	Depth of BDTZ [km]	Surface displacement [m]	dis-Recurrence interval [Kyr]	Regular recurrence start time [Myr]
Q1W	17.6–20.4	0.76	1.54	0.4
A1W	23.9–27.0	0.84	1.70	0.5
Q1S	15.5–18.0	0.67	1.39	1.0
A1S	21.6–24.5	0.77	1.59	1.4
Q30W	19.7–23.0	0.90	0.061	0.015
Q30S	17.6–20.4	0.78	0.053	0.038
Linear	18.7–23.9	1.23	2.52	0.8

The results, which are depend on the assumptions, are summarized in Table 6.

3.3.6 Effect of model configurations

In order to understand how the rock rheology, far field loading rate and fault strength affect the evolution of the shear stress, deformation, and the effective viscosity structure, I consider 7 different cases, including one with linear Maxwell viscoelastic materials whose viscosity structure is predefined using the effective viscosity structure shown in Figure 19b. Figure 23 and Figure 24 show the distribution of shear stress, effective viscosity and viscous shear strain rate of intraplate and interplate cases, respectively. These figures are plotted at the end of the interseismic period in an earthquake cycle after the regular recurrence has been reached. For each case, time to reach regular recurrence is summarized in Table 6.

The first row of Figure 23 and the first column of Figure 24 show the distribution of shear stress. In our model, the fault strength is the primary controlling factor on the magnitude of the shear stress in the bulk of the crust and the upper mantle. The

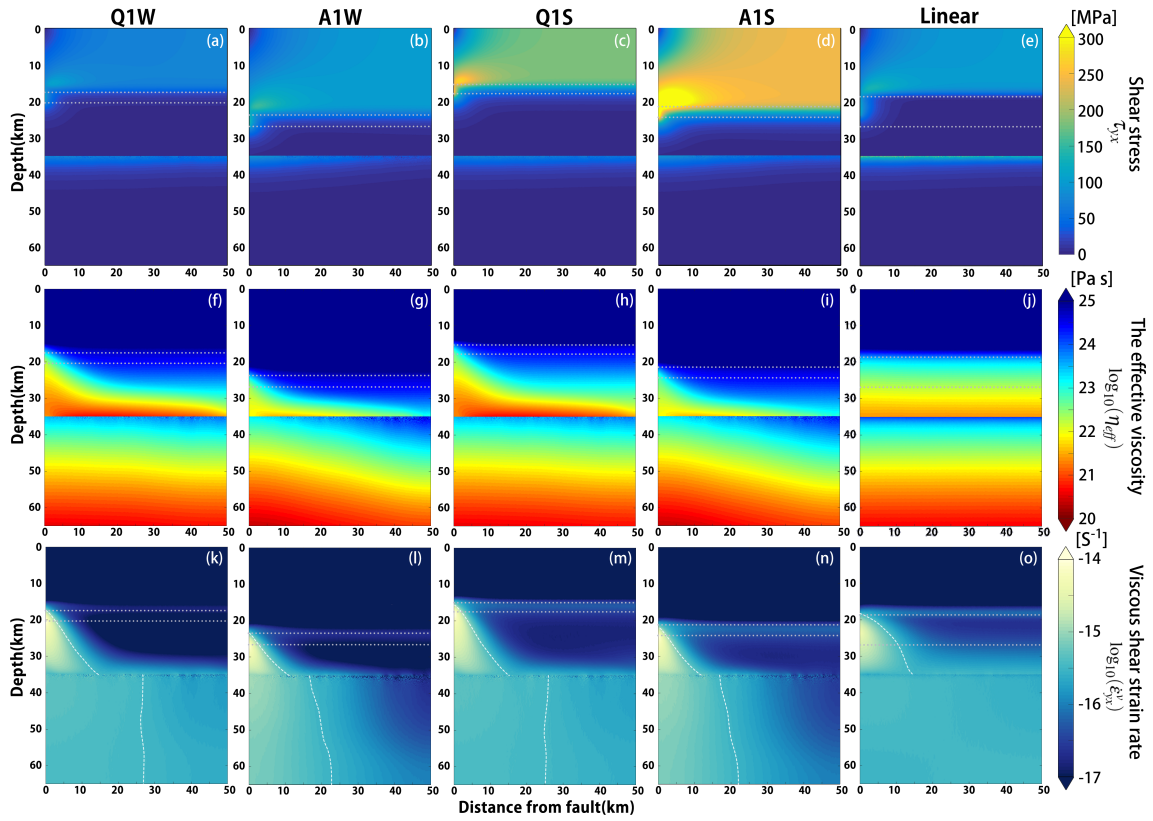


Figure 23: Shear stress(a-e), effective viscosity(f-j) and viscous shear strain rate(k-o) distributions of intraplate cases after regular recurrence is reached. Figures are plotted at the end of an interseismic period right before an earthquake. Each row shows the results of a case and the name of the case is shown on the top of the row. White broken lines indicate the location where viscous shear strain rate is not changed from the shear strain rate of uniformly distributed simple shear which is about $3.17 \times 10^{-16} \text{ s}^{-1}$ in intraplate cases. The gray broken lines indicate the depth of BDTZ (*Zhang and Sagiya, 2018*).

fault strength depends on the depth and the fault's frictional coefficient. In the cases with a same rock rheology, the magnitude of shear stress in the cases with a fault frictional coefficient of 0.6 are 3 times larger than that in the cases with a fault frictional coefficient of 0.2.

In each case, the shear stress reaches its maximum at the depth of BDTZ. The deeper the BDTZ, the larger the magnitude of shear stress in the BDTZ. In the cases with a same fault frictional coefficient (Q1W and A1W, Q1S and A1S), the depth of BDTZ varies with the assumption of rock rheology. Compared to the cases with wet quartz, the depth of BDTZ is ~ 6 km deeper in the cases with wet anorthite (Table 6). As a result, the shear stress in the cases with wet quartz (Figure 23a and 23c) is smaller than that in the cases with wet anorthite (Figure 23b and 23d). The far field boundary velocity has a smaller effect to the depth of BDTZ compared to the rheology. In the cases of intraplate cases, the depth of BDTZ is only ~ 2 km shallower than that in the interplate cases (Table 6). In the interplate cases, the slip rate is 30 times faster than the intraplate cases, while the shear stress in the lower crust under fault is only ~ 3 times larger than intraplate cases. In the nonlinear cases, because I assume a power law rheology for the entire model, the viscous shear stress in the lower crust is proportional to shear strain rate with a power of $1/n$ ($n = 3$). Therefore, the shear stress is less sensitive to the shear strain rate.

The second row of Figure 23 and the second column of Figure 24 show the distribution of effective viscosity. Because the shear strain rate is proportional to the far field velocity and the effective viscosity is proportional to the shear strain rate with a

power of $(1 - n)/n(n = 3)$. Compared to the intraplate cases, 30 times faster shear strain rate in interplate cases result in a ~ 10 times smaller effective viscosity.

The third row of Figure 23 and the third column of Figure 24 shows the distribution of viscous shear strain rate. Unlike the shear stress, viscous shear strain rate in the shear zone and the far field velocity have a positive linear relationship with each other. The maximum value of the shear strain rate in the case of intraplate cases (Figure 23k-23o) and the interplate cases (Figure 24e and 24f) are $\sim 1.7 \times 10^{-14} \text{ s}^{-1}$ and $\sim 4.6 \times 10^{-13} \text{ s}^{-1}$, respectively. In the lower crust and the upper mantle, white broken lines in Figures Figure 23k and 23o and Figure 24e and 24f indicate the location where shear strain rate does not change from the beginning when deformation is dominated by uniformly distributed simple shear. Deformation concentrates on the left-hand side of the broken line closer to the fault tip. With a elevated shear strain rate, a shear zone with a localized high shear strain develops under the fault. At any depth, the distance of the fault plane to the broken line indicates the degree of the shear strain concentration. The smaller the distance is, the higher the degree of shear strain concentration becomes. Thus the white broken line enables us to compare the width of the shear zone in different cases. The shear zone width increases with depth and it is not influenced by the far-field velocity as the location of white broken lines is similar to each other in the cases assuming wet quartz rheology (Figure 23k, 23m, 24e and 24f).

The assumption of rock rheology has a significant influence on the width of the shear zone. In the deepest part of the lower crust near Moho, the width of the shear zone in the cases of wet anorthite (Figure 23i, 23n) is narrower than the cases of wet

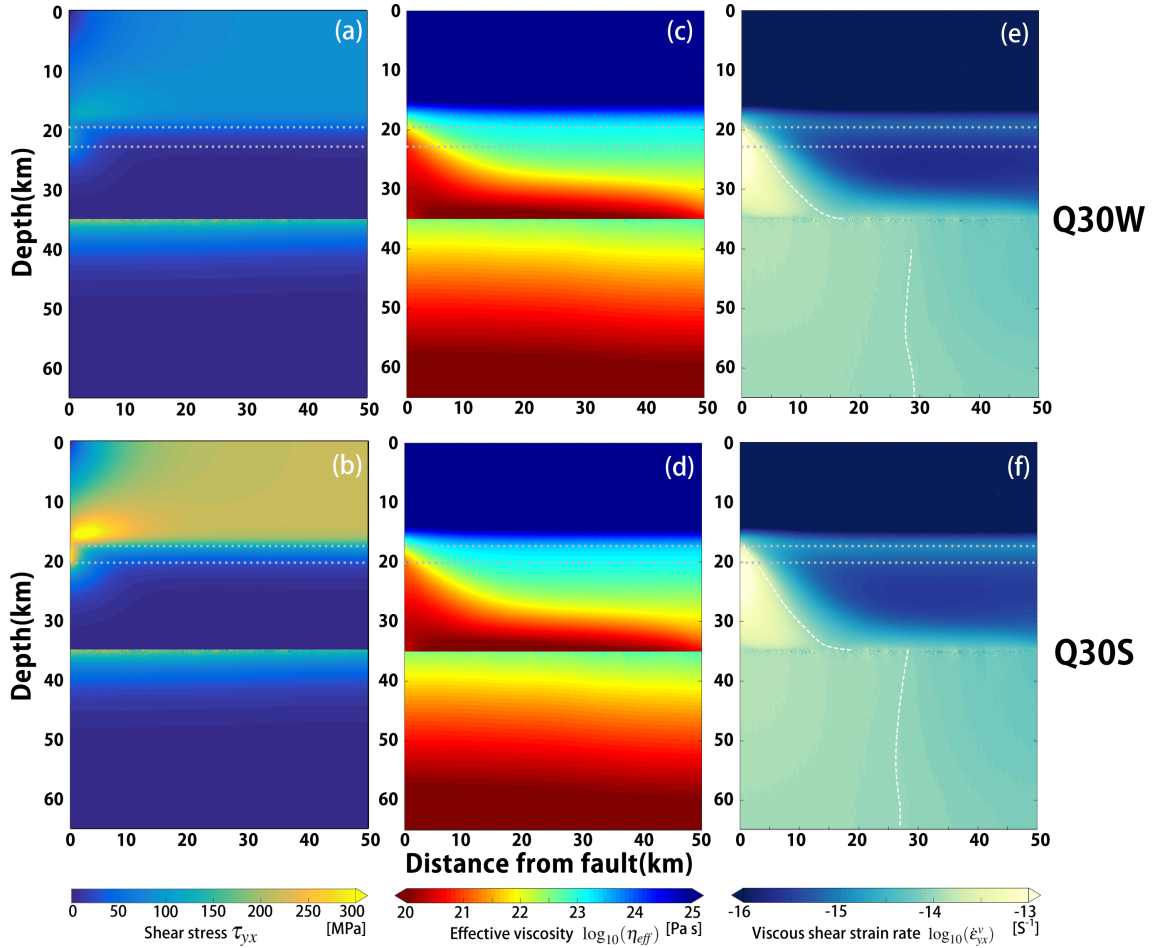


Figure 24: Shear stress(a and b), effective viscosity(c and d) and viscous shear strain rate(e and f) distributions of interplate cases after regular recurrence is reached. Figures are plotted at the end of an interseismic period right before an earthquake. Each column shows the result of a case and name of the case is shown at the end of the column. White broken lines indicate the location where viscous shear strain rate is not changed from the shear strain rate of uniformly distributed simple shear which is about $9.51 \times 10^{-15} \text{ s}^{-1}$ in interplate cases. The gray broken lines indicate the depth of BDTZ (*Zhang and Sagiya, 2018*).

quartz. In the upper mantle, the deformation is also more concentrated in the cases of wet anorthite compared to the cases of wet quartz. This is because of the larger effective viscosity in the deepest part of the lower crust and the deeper BDTZ in the cases of wet anorthite compared to the cases of wet quartz.

The results of the linear case are shown in the last column of Figure 23. The effective viscosity structure of the linear case is fixed using the result at the end of the 10th interseismic period of model Q1W(Figure 19j). Because of the reduced effective viscosity in the nonlinear case of Q1W, the depth of the bottom of the BDTZ is ~ 2.5 km shallower than the linear case. In the lower crust, because the stress concentration is a result of repeating earthquake in the upper crust, the linear and the nonlinear cases have similar degree of stress concentration. On the other hand, the width of shear zone in the linear case is larger than the nonlinear cases. For example, at depth of 25 km, the width of shear zone in nonlinear case Q1W is 6.0 km, which is shorter than 9.2 km in the linear case. These results show that the deformation is less concentrated in the linear case (Figure 23o) compared to the nonlinear case Q1W (Figure 23k). Compared to the linear case, much smaller shear stress is required for nonlinear cases to achieve the same magnitude of shear strain rate. After the regular recurrence starts, the maximum value of the shear strain rate in the linear case is $\sim 6.1 \times 10^{-15} \text{ s}^{-1}$, which is only about one-third of the nonlinear case Q1W.

3.4 Discussion

3.4.1 Stage of the fault evolution

In the simulation of this study, before the start of regular earthquake cycle, two distinct stages can be defined from the results of the fault evolution. Figure 25 shows the time evolution of the maximum coseismic offsets in each earthquake (a), the recurrence interval (b) and fault tip depth (c) for model Q1W. The first stage is the stress build-up stage, which starts from the beginning and ends at the time when the fault rupture reaches the upper boundary of the BDTZ. In this stage, the shear stress builds up in the upper crust, and the coseismic offset on the surface increases with the fault tip depth. The second stage is the shear localization stage, which starts right after the first stage and continues until a regular cycle is reached. In this stage, deformation is gradually localized under the fault in the lower crust.

In the first few earthquakes, the fault tip depth increases by ~ 1.4 km in each earthquakes. The slip distance on the ground surface is small and the recurrence intervals of earthquakes are as long as ~ 16 kyrs. As the stress builds up on the fault, the rupture extends to the deeper part of the upper crust and the surface rupture increases to its maximum value of 4.4m at the end of the first stage. In the stress build-up stage from ~ 0.2 Myr to ~ 0.4 Myr, the maximum coseismic offset in each earthquake gradually decreases to 1.54 m. Regular earthquake starts after 0.4 Myr. After that, earthquakes with a coseismic offset of 1.54 m occur every 1.54 kyrs.

In our model, the far field loading and fault cohesive strength is assumed to be a

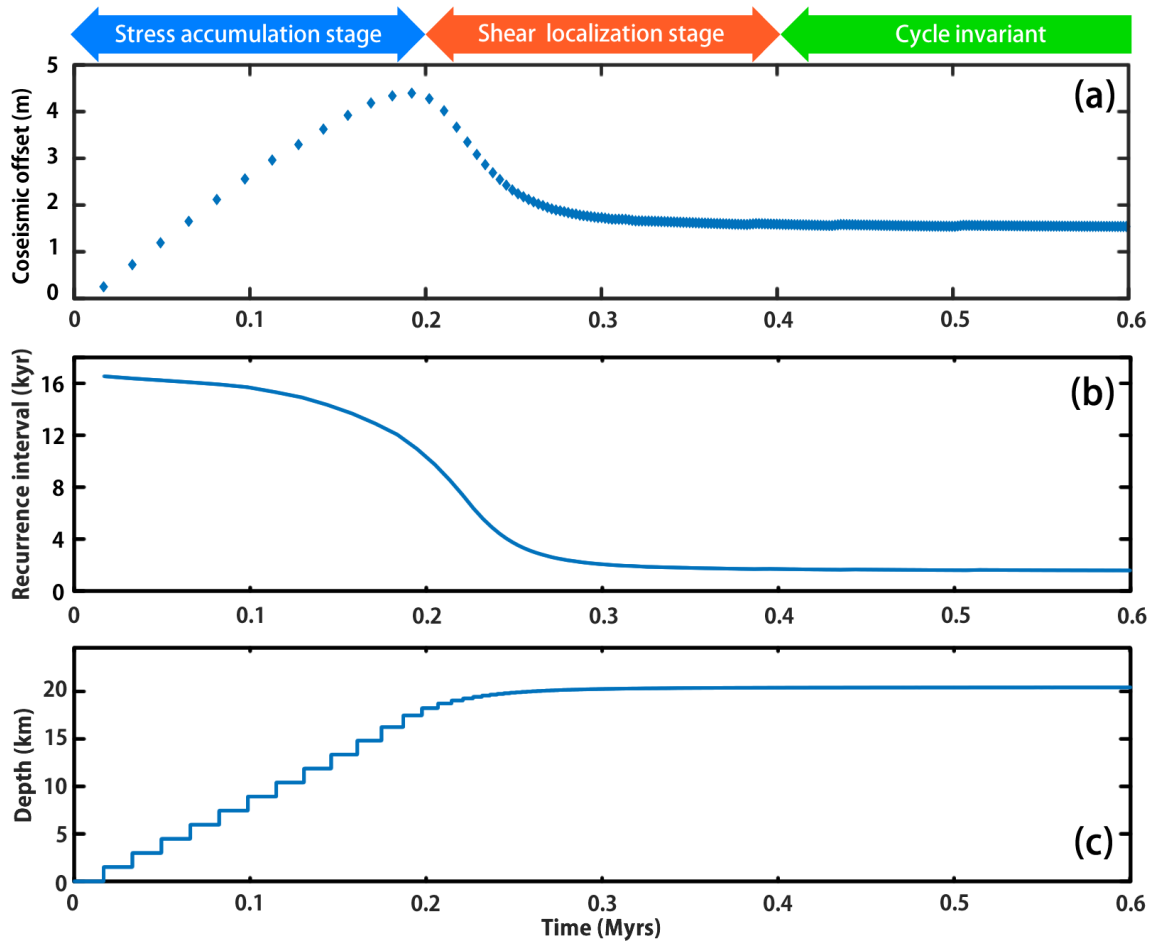


Figure 25: Time evolution of coseismic offset on the surface in each earthquakes (a), recurrence interval (b) and (c) fault tip depth for model Q1W. Each rhombus dots in (a) represents an earthquake (*Zhang and Sagiya, 2018*).

constant. However, as a result of the loading from localized deformation in the lower crust, the recurrence interval changes in the process of fault evolution. As shown in Figure 25b, recurrence interval decreases from the beginning to the end of the shear localization stage, which indicates the growing influence of the localized lower crust deformation. With continuous loading in the far field, the fault is expected to become recognizable as an active fault because the cumulative offset increases with time as moderate earthquake with a ~ 1.5 m total offset repeats every 1500 years.

In the nonlinear cases of our model, the durations of the two evolution stages are roughly equal to each other. The recurrence intervals after the regular earthquake cycle starts are about one-tenth of the recurrence interval at the beginning of the simulation. On the other hand, in the linear case, the shear strain rate linearly depends on the shear stress, which results in a smaller increment of the shear strain rate after each earthquake compared to the case of Q1W, as a result, the time duration of shear localization stage is ~ 0.6 Myrs, which is three times longer than its nonlinear counterpart case Q1W. Time to reach regular recurrence for all the cases considered in this study are summarized in Table 6.

3.4.2 Development of a ductile shear zone development

Our results show that the development of a ductile shear zone in the lower crust is directly related to the cumulative offsets on the surface (Figure 26a and Figure 27a), which suggests that heterogeneous structures are expected to be more obvious under a strike slip fault with a larger cumulative offset. *Zhu (2000)* showed that Moho offsets under the San Andreas fault (SAF) in southern California are more obvious compared

to that under the eastern California shear zone (ECSZ). For other major continental strike slip faults, such as the Alpine fault in New Zealand, the North Anatolian Fault in Turkey and the Altyn Tagh Fault in Tibet, geophysical observations showed heterogeneous seismic velocity structures under these faults, which suggest that fault related shear zones do exist (e.g. *Stern et al.*, 2013; *Elvira et al.*, 2017; *Wittlinger et al.*, 1998). The cumulative offsets of these faults range from several tens of kilometers to several hundreds of kilometers (*Stirling et al.*, 1996; *Cowgill et al.*, 2003), which are long enough to have a developed shear zone in the lower crust.

Slip rates of the intraplate strike slip faults are much slower than interplate strike slip faults, which means that intraplate strike slip faults need a much longer time to develop shear zones beneath them. Due to the small accumulated shear strain, for most intraplate strike slip fault, plastic shear zones may not be visible by geophysical observations. Shear localization, on the other hand, starts at an early stage when the maximum value of accumulated shear strain is less than 0.01 (Figure 27). In the case of A1W, it takes ~ 0.7 Myrs to start localized deformation in the lower crust which is the latest among all 4 nonlinear cases with 0.5 mm/year boundary velocity.

For a recognizable strike slip fault with a large offset more than few hundred meters, shear deformation is likely to be localized under the fault and the surrounding lower crust is likely to behave in a quasi-rigid manner. Therefore, for most of known intraplate active strike slip faults, the screw dislocation model in an elastic half space (*Savage and Burford*, 1973) can be used to interpret the observed deformation around the faults and yields reasonable estimates of the fault locking depth (e.g. *Ohzono et al.*,

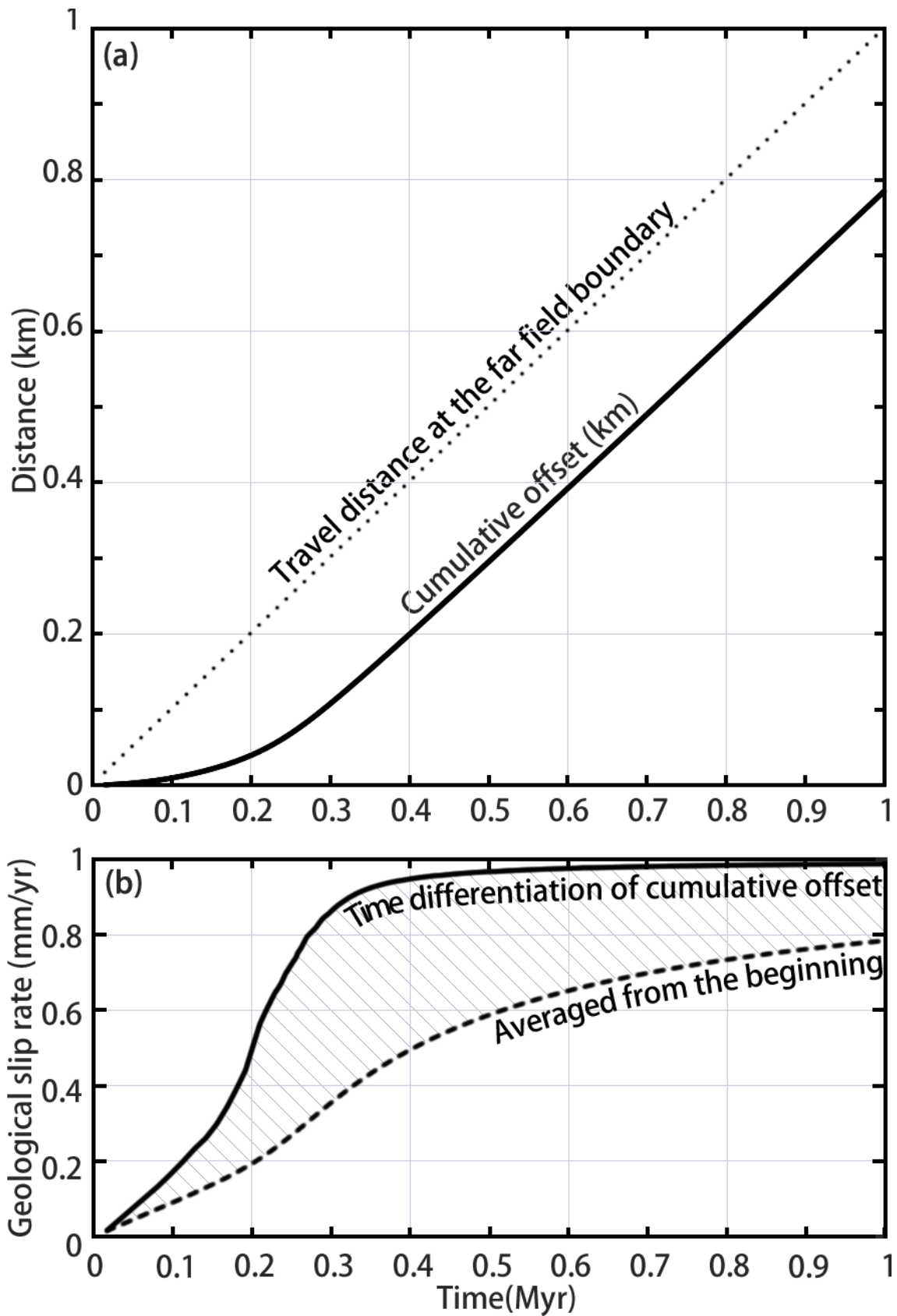


Figure 26: Cumulative fault slip (a) and Geological slip rate (b) from the case of Q1W (Zhang and Sagiya, 2018).

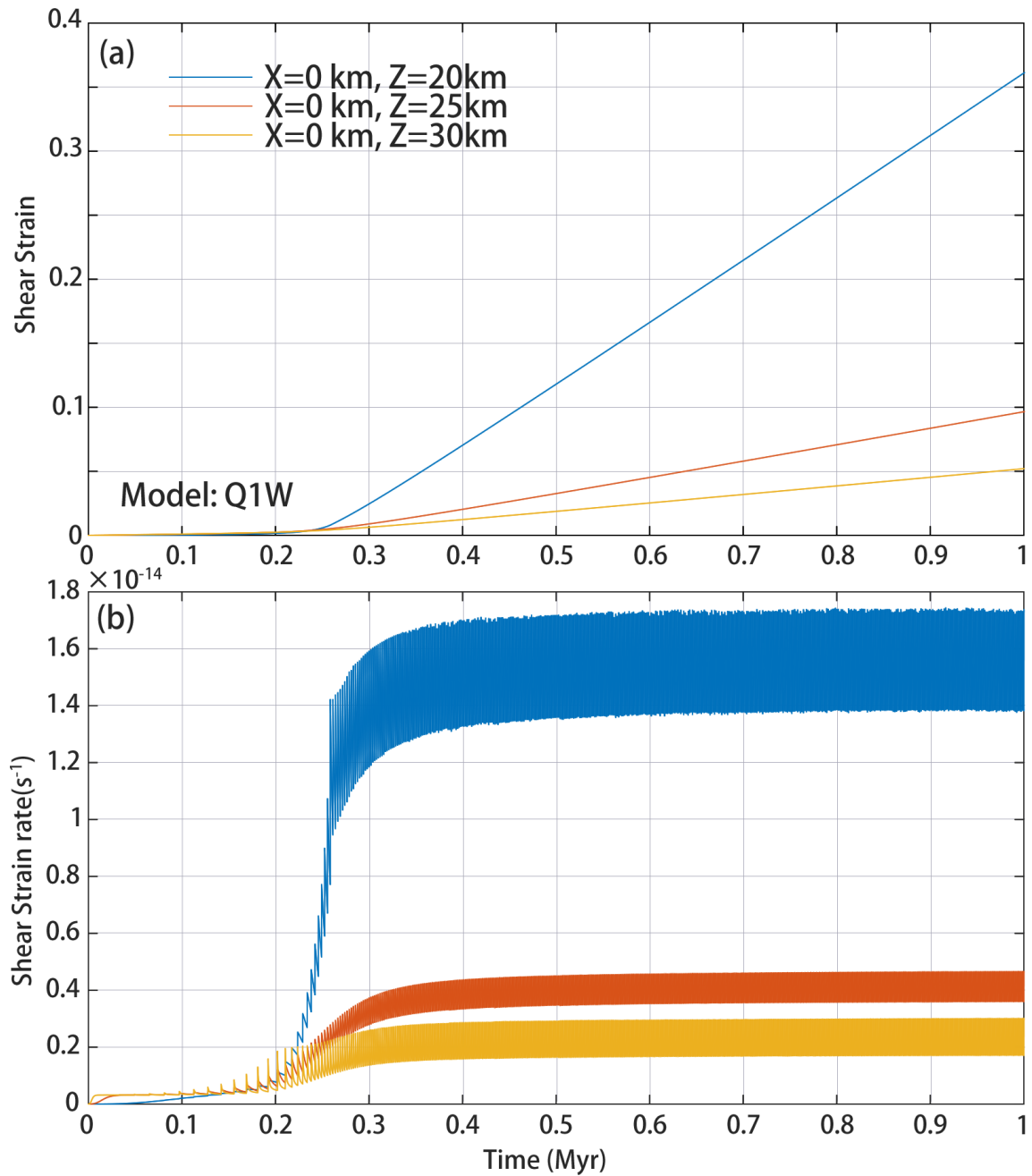


Figure 27: Shear strain(a) and Shear strain rate(b) and under the fault in the lower crust, example taken from case Q1W (*Zhang and Sagiya, 2018*).

2011). The mechanical model in this study provides a physical base for the validity of the screw dislocation model. On the other hand, for strike slip fault in their developing stages, because there is no localized deformation under the fault, the simple screw dislocation model may not work properly.

3.4.3 Implication to the discrepancy between Geodetic and Geological fault slip rate

For a mature fault with a large offset and stable long term slip rate, such as the San Andreas Fault (SAF), the slip rates estimated by geodetic observations are in general agreement with those estimated by geological observations (e.g. *Bourne et al., 1998*). On the other hand, the discrepancy between geodetic and geological slip rate can be found in many intraplate strike slip faults (e.g. *Meade and Hager, 2005; Oskin et al., 2008; Ohzono et al., 2011*). Possible explanations such as a shallow slip deficit (*Fialko et al., 2005*), off-fault deformations (*Herbert et al., 2014*) and time-dependent interseismic velocity (*Meade et al., 2013*) have contributed to our understanding of the discrepancy between geodetic and geologic fault slip rates.

In the study of *Herbert et al. (2014)*, the contribution of the off-fault plastic deformation on the deformation across the fault zone has been estimated in the eastern California shear zone (ECSZ) using mechanical models. The model results showed that $\sim 40\%$ of the total relative motion has been accommodated by the off-fault plastic deformation. By considering the off-fault plastic deformation, $\sim 60\% - 70\%$ of discrepancy between geodetic and geological fault slip rate in the ECSZ can be explained. On the scale of a single fault, the shallow slip deficit may affect the obser-

vation results of geological slip rate. In the study of *Fialko et al. (2005)*, the shallow slip deficit model postulates that coseismic slip in the shallower part of the upper crust (0–4 km) is less than that in the depth of seismogenic layer (4–10 km). In the shallower part of the upper crust where plastic strength is relatively low, the plastic deformation may accommodate most of the relative motion across the fault. A large discrepancy between geodetic and geological fault slip rate can result from an underestimated geological slip rate. During the interseismic period, due to the viscoelastic relaxation in the lower crust and upper mantle, the geodetically observed velocities are time dependent (e.g. *DeVries and Meade, 2013*). The geodetically observed short-term (years and decades) velocity may be different from the velocity averaged over geological time scales. Such kind of difference can also contribute to the discrepancy between geodetic and geological fault slip rate (*Meade et al., 2013*).

In this model, I find an additional clue to understand the discrepancy between geodetic and geologic fault slip rates. Figure 26a shows the cumulative surface offsets in case Q1W and the travel distance at the far-field boundary. Figure 26b shows the modeled geological slip rate calculated on the fault. In Figure 26b, the solid line shows the time differentiation of the cumulative offsets representing the instantaneous slip rate at each moment and the broken line shows a long-term fault slip rate calculated by the cumulative fault offset from the beginning divided by the elapsed time. This result shows that even in such a simplified model, the geological slip rate could be underestimated because of the delayed accumulation of the fault offset corresponding to the tectonic stress build-up. After a few millions of years of the constant tectonic

loading, slip rate discrepancy due to the fault evolution becomes negligible and the geological slip rate catches up with the geodetic slip rate.

If the measurement is conducted at a different depth, due to the increasing coseismic offsets toward the surface (Figure 22b) in the developing stage of the fault evolution, the measured geological slip rate on the fault might be slower than the slip rate shown in Figure 26b. Even in such a case, however, the geological slip rate will catch up with the geodetic slip rate as the modeled coseismic slip is almost a constant in the elastic upper crust after the regular recurrence is reached (Pink line in Figure 22b). On the other hand, at the depth of the BDTZ, the modeled coseismic offset is smaller than that in the elastic upper crust because the surrounding plastic flow accommodates significant relative motion. Therefore, slip rate in an eroded and exposed BDTZ will be much smaller.

If there is a temporal change of the regional tectonic motion in the continental crust, optimally oriented faults can be newly created or reactivated. But the fault offset accumulation is delayed due to the creation of the tectonic stress field. Faults under such a condition may demonstrate a significant discrepancy between their geodetic and geologic slip rates. Such a delay effect is expected to be more common for slowly moving intraplate faults.

3.4.4 Mechanical model comparison

Previous investigations of the deformation of the lower crust and the upper mantle using mechanical models have shown that, in the lower crust, localized shear deformation develops under the interplate (e.g. *Thatcher and England, 1998; Takeuchi and*

Fialko, 2012; Moore and Parsons, 2015; Allison and Dunham, 2018) and intraplate (e.g. *Zhang and Sagiya, 2017*) strike slip faults. With regard to the deformation in the upper crust, some of these models considered the repeating earthquakes (e.g. *Takeuchi and Fialko, 2012; Erickson et al., 2017; Lambert and Barbot, 2016; Allison and Dunham, 2018*) and others assumed a creeping fault (e.g. *Thatcher and England, 1998; Moore and Parsons, 2015; Zhang and Sagiya, 2017*). In spite of these different assumptions, they share a common feature that there is a localized deformation in the lower crust under the fault. It is because the long-term behavior of the upper crust in all these earthquake cycle model is block-like after the regular earthquake recurrence starts and at least one shear concentration mechanism for the lower crust, such as shear and frictional heating, power law rheology and grain size reduction, has been incorporated. Our results show that, under a slowly deforming intraplate strike slip fault in the lower crust, a few million years are necessary to develop a shear zone with a high shear strain (> 1).

In the previous studies assuming nonlinear rheologies for the lower crust and upper mantle, regular cycle can be reached only after thousands of earthquake cycles (e.g. *Takeuchi and Fialko, 2012; Allison and Dunham, 2018*). This spin-up process corresponds to the tectonic stress build-up. Our simulation demonstrates that the fault behavior is highly variable during the stress build-up process, which is controlled by the model assumptions such as the far field velocities and the fault strength. Without careful examination of the model assumptions, unexpected results, such as the negative shear strain rate in the lower crust (*Takeuchi and Fialko, 2012*), extremely large

shear stress right below the strike slip fault (e.g. *Moore and Parsons, 2015; Zhang and Sagiya, 2017*) appear in the simulation results. Several model assumptions may have led to those unexpected results. For example, the thickness of the upper crust in the model is often fixed according to the thickness of the seismogenic layer. This assumption does not cause any problems in models assuming linear rheology for the lower crust as the viscosity is independent of the shear stress (e.g. *Thatcher and England, 1998*). However, in the models considering power law rheology, due to the relatively low temperature in the shallower part of the lower crust, the effective viscosity there becomes extremely large ($> 10^{24}$ Pa s). In thermo-mechanical models, in order to enable the viscous flow in the shallower part of the lower crust, a tremendous amount of heat is generated in the shear zone to reduce the effective viscosity (e.g. *Takeuchi and Fialko, 2012; Moore and Parsons, 2015*). This problem has been partially solved in our model by calculating the depth of the bottom of the BDTZ according to the assumed boundary conditions and rock rheologies. Through such a consideration, as shown in Chapter 2, shear stress in the lower crust is less than few hundreds MPa which is comparable to the fault strength in the BDTZ. On the other hand, in the BDTZ where effective viscosity is larger than 10^{24} Pa s, only plastic deformation is allowed and the shear stress can exceed 1 GPa. In this study, the maximum value of the shear stress does not exceed a few hundreds MPa (Figure 23) which is comparable to the fault strength at depth. The mechanical model in this study demonstrates that the depth of the BDTZ depends on model assumptions including the rock rheology, fault strength and far field velocity. Therefore, it is not appropriate to impose an

elastic/brittle upper crust layer for the simulation of crustal deformation.

3.5 Conclusions

I have developed a self-consistent earthquake cycle model for simulating the evolution of an intraplate strike slip fault with nonlinear Maxwell rheology. I investigate the stress build-up process in an initially stress-free crust-mantle system in the geological timescale. At the beginning of stress build-up process, the stressing rate is constant in the entire model. Due to the plastic flow, stressing rate become zero in the lower crust and the upper mantle. As stress increases in the upper crust, the deeper part of the upper crust with a higher strength can be broken by the earthquakes. As the fault tip getting closer to the BDTZ, shear stress, as well as shear strain deformation, starts to concentrate near the fault tip.

The depth of the BDTZ depends on the fault strength, rock rheology, and total relative velocity in the far field. Before the fault tip reaches the BDTZ, there is no concentrated deformation in the lower crust and the earthquakes have very long recurrence interval of ~ 16 kyrs in the cases of 1 mm/yr total relative slip rate at 50 km away from the fault. The recurrence interval is influenced by the concentrated shear stress deformation in the lower crust as the fault tip getting closer to the lower crust. After the regular earthquake recurrence starts, the recurrence interval decreases by an order of magnitude.

Under a slowly deforming intraplate strike slip fault, time to develop a shear zone with large shear strain is much longer than the time for shear strain deformation to

concentrates under the fault. Shear zone in the lower crust under an intraplate strike slip fault may not be detectable with geological observations. Even without any geophysical evidence of shear zone under the intraplate strike slip fault, simple screw dislocation model (*Savage and Burford, 1973*) can explain the geodetically observed deformation across the fault. Our model provides the physical explanation of the validity of the screw dislocation model.

Chapter 4

Discussions

In Chapter 2 and Chapter 3, I conduct a series of numerical simulations to understand the evolution of the deformation in the lower crust under an infinitely long strike slip fault. The results of the thermo-mechanical model in Chapter 2 shows that the power-law rheology plays an important role in forming the shear zone in the lower crust under a slowly deformed intraplate strike slip fault. In the mechanical earthquake cycle model in Chapter 3, I find a relation between the deformation in the lower crust and the strike slip faulting in the upper crust. The degree of the shear strain localization in the lower crust increases with the cumulative offset of the fault in the upper crust. The longer the cumulative offset, the higher the degree of the shear strain concentration. The localized deformation exerts a drag force on the upper crust which increases the stressing rate on the fault and results in a shorter recurrence interval of the earthquakes.

In this chapter, first, I discuss a few major problems in the mechanical model in Chapter 3: In the upper crust of the model, the plastic deformation was not considered and the calculated shear stress near the surface is larger than the typical cohesive strength of rocks. Based on preliminary results of a model assuming a visco-elasto-

plastic material, I discuss how plastic deformation in the upper crust affects the shear stress accumulation process and the evolution of the crustal deformation. In the far field boundary, a constant velocity has been assumed to represent tectonic loading. However, in the plate interior far away from the plate boundary, the loading may come from the mantle flow. By assuming a constant shear strain rate on the Moho, I calculate the shear stress evolution in the crust. According to the calculation results, I discuss a possibility of loading a crust by the mantle flow. The fault in this model is assumed to be infinitely long and the influence of the fault ends was not considered. Based on the previous studies, I discuss the influence of the fault ends and possible solutions to the problems. Finally, based on calculation results of this study, I discuss the implications for the intraplate strike slip earthquake activities.

4.1 Effect of off-fault plastic deformation on the evolution of intraplate strike slip fault

In the shallower part of the upper crust, the rocks can be deformed by irrecoverable plastic deformation (*Barton, 1976*). On a scale of a single fault, field observations showed that highly damaged rocks exist in the vicinity of the fault. The damaged zone usually have a thickness less than few hundreds of meters (e.g. *Childs et al., 2009*; *Shelef and Oskin, 2010*) and it is surrounded by the undeformed host rock (*Chester et al., 1993*). In the earthquake cycle model of this study, the damage zone in the vicinity of the strike slip faulting is approximated by a fault surface that has no thickness. Because the shear stress and shear strain near the fault is released by the earthquakes,

a small region with a width of a few kilometers next to the fault can be considered as the undeformed host rock.

On a scale of a strike slip fault system, the tectonic loading can be shared by the faults sub-parallel to the main fault (e.g. *Meade and Hager, 2005*). The off-fault plastic deformation between those faults has been suggested by the mechanical model in *Herbert et al. (2014)*. In Chapter 3, I investigate the fault evolution with a mechanical model composed of nonlinear visco-elastic material. In the upper crust, because the off-fault plastic deformation is not considered in this model, the shear stress in the bulk of the upper crust far away from the fault is ~ 70 MPa and ~ 210 MPa in the case with weak and strong fault, respectively. Such a large shear stress is significantly larger than the strength of the rocks at low confining pressures (e.g. *Hallbauer et al., 1973*; *Barton, 2013*).

In this section, as a candidate mechanism to moderate the stress level in the upper crust, I consider the off-fault plastic deformation in the upper crust. The assumptions considered in this section is conjectural and I offer the preliminary calculation results for the propose of the present discussion. Based on the time dependent calculation results of the plastic deformation, I investigate how the strike slip faulting and the off-fault plastic deformation interact with each other and I discuss how off-fault plastic deformation influences the geological and geodetic observations on a strike slip fault zone.

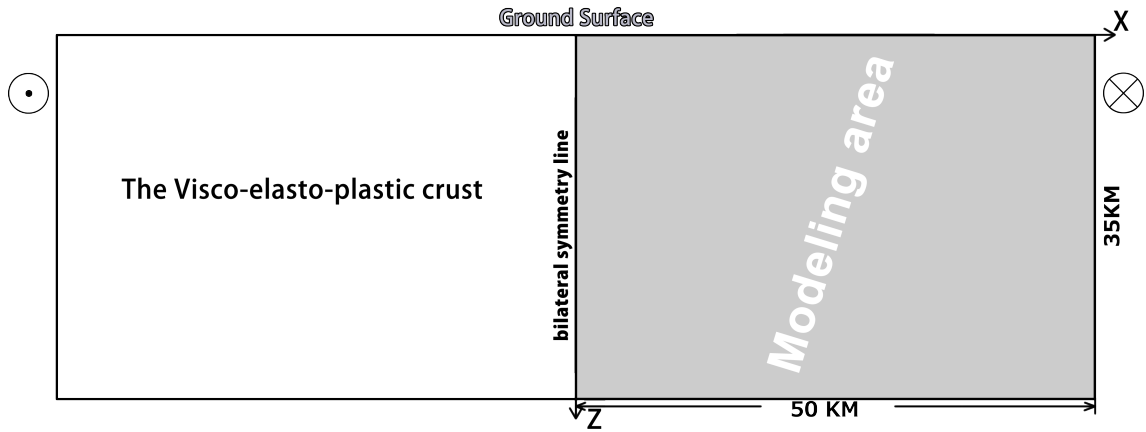


Figure 28: Geometry for the model consider the plastic deformation in the upper crust

4.1.1 Model settings

In order to simulate the plastic deformation in the upper crust, I make several changes on the mechanical model in Chapter 3. The model geometry is shown in Figure 28. Since there is almost no shear strain concentration in the upper mantle in the earthquake cycle in the Chapter 3 (Figure 20), the deformation of the upper mantle is not included in this study. At the depth of Moho, I apply a constant shear strain rate boundary condition ($\dot{\epsilon}_{yx} = 0.01\text{ppm/yr}$).

The rheology model for the entire crust is assumed to be visco-elasto-plastic rheology (e.g. *Ranalli, 1995*) with the total shear strain rate $\dot{\epsilon}^T$ including three different components.

$$\dot{\epsilon}^T = \dot{\epsilon}^v + \dot{\epsilon}^e + \dot{\epsilon}^p, \quad (4.1)$$

where $\dot{\epsilon}^p$ is the plastic shear strain rate, the viscous $\dot{\epsilon}^v$ and elastic $\dot{\epsilon}^e$ shear strain rate follow the definition in previous chapters (Eq. 2.1 and 3.3). For the plastic deformation in the upper crust, I consider an elastic-perfectly plastic material. The increment

of the plastic strain is defined as follows

$$\Delta\varepsilon^p = \begin{cases} 0 & (\tau_s < \tau_{yield}) \\ \Delta\tau_s/G & (\tau_s = \tau_{yield}) \end{cases} \quad (4.2)$$

where τ_{yield} is the plastic yield strength for given rock. $\Delta\tau_s$ is determined at each time step of calculation to satisfy the plastic yielding condition: $\tau_s = \tau_{yield} = \mu_f \sigma_n + C_f^p$, where μ_f is the coefficient of internal friction, σ_n is the lithostatic stress and C_f^p is the cohesive strength of the crustal materials which is assumed to be larger than fault frictional strength. When plastic yield strength is reached, the plastic strain increment ($\Delta\varepsilon^p$) is calculated in two steps. In the first step, the shear stress change in a time step is calculated as it is for the model with visco-elastic material. In the second step, the plastic shear strain increment is calculated from $\Delta\tau_s$, which is the amount of shear stress exceeds the plastic yield strength. I tested different cohesive strength including 10 MPa, 15 MPa and 20 MPa. These cases are respectively named Q1W_VEP_10, Q1W_VEP_20 and Q1W_VEP_30.

4.1.2 Shear stress evolution process

The shear stress evolution of the case Q1W_VEP_10 is shown in Figure 29. At the beginning before the first earthquake, there is no plastic deformation as the stress in the entire model is smaller than the fault cohesive strength of 5 MPa. The shear stress distribution shown in Figure 29a is similar to that in case Q1W (Figure 18a). As the stress accumulates in the upper crust, the shear stress reaches the plastic yield strength after a few earthquake cycles. In the region where plastic yield strength is reached, the shear stress increases with depth. Figure 29b shows the shear stress before the 10th

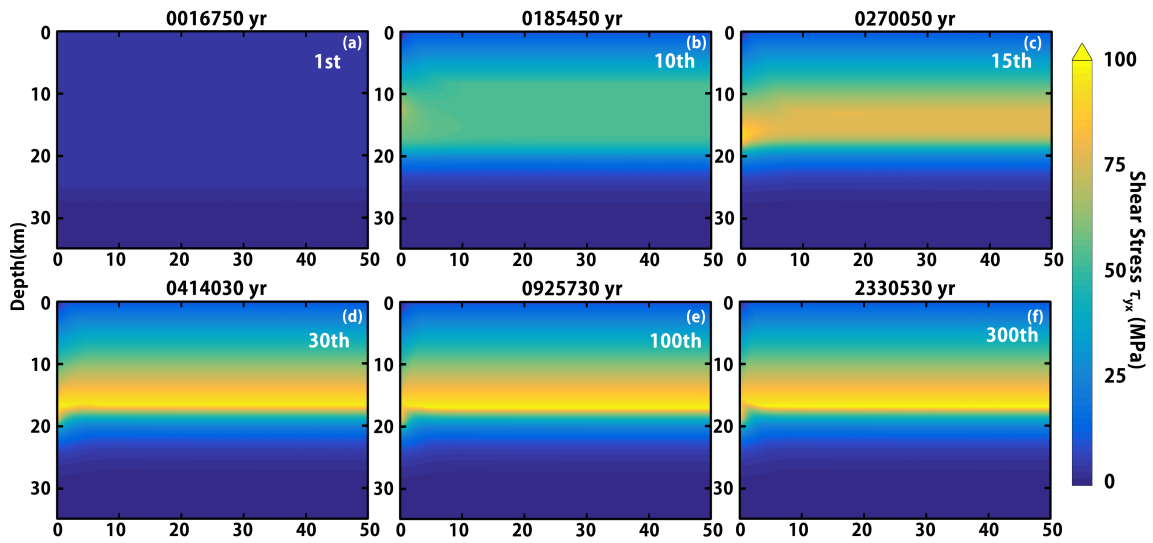


Figure 29: Shear stress τ_{yx} evolution in the model of Q1W_VEP_10, each figure is plotted right before an earthquake, the number of earthquake cycle is shown in each figure and the elapsed time is shown on the top of each figure.

earthquake. Shear stress gradually concentrates around the fault tip as earthquakes repeat. After the fault tip reaches the BDTZ (Figure 29d), the shear stress in the lower crust starts to localize under the fault. Unlike the cases assuming no plasticity in the upper crust in Chapter 3, the shear stress concentration in the bulk of the upper crust due to the basal drag of the lower crust is not obvious in the model considering the plasticity in the upper crust because the concentrated shears stress in the upper crust is larger in the model assuming no plasticity in the upper crust is larger than the plastic strength. Because the shear stress concentration in the lower crust is a result of earthquakes in the upper crust, the number of the earthquakes in each evolution stage is similar to that of the viscoelastic model in Chapter 3. The regular earthquake cycle is reached at the 100th earthquake (Figure 29e) at 926kyr and after that, the change of the shear stress become negligible.

4.1.3 Evolution of plastic deformation in the upper crust

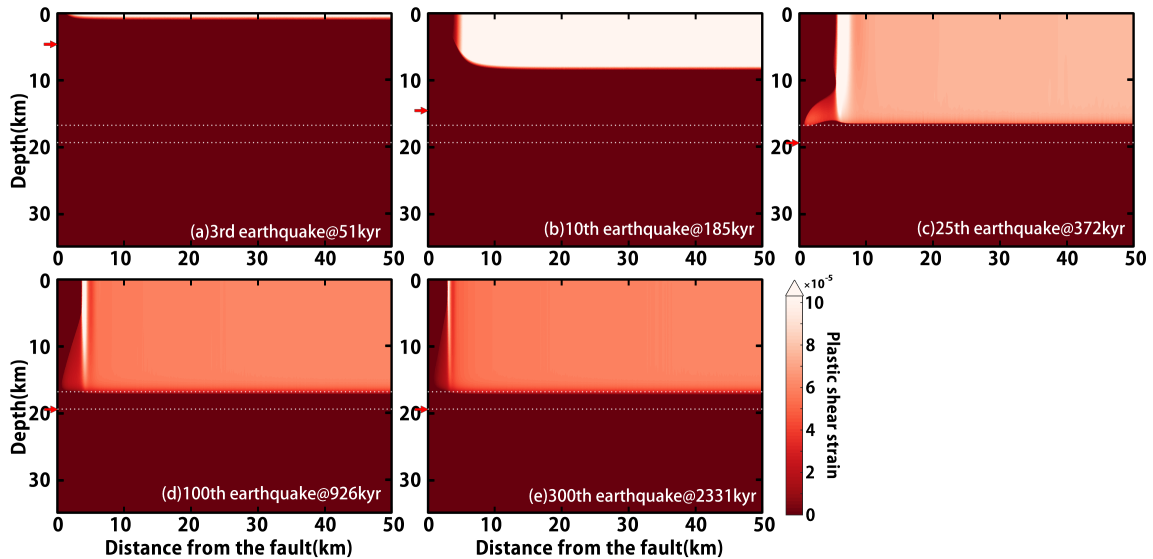


Figure 30: Plastic shear strain (ϵ_{yx}) accumulated in an earthquake cycle in the model with 10 MPa off-fault cohesive strength, the number of earthquake cycle and the elapsed time is shown in each figure. The red arrows indicate the depth of the fault tip and the white dot lines indicate the boundaries of the BDTZ

Figure 30 shows the plastic shear strain (ϵ_{yx}) accumulated during an interseismic period in the case of Q1W_VEP_10. At the beginning, the shear stress is smaller than the plastic strength, and the upper crust deforms as an elastic material. Near the ground surface, the stress reaches the yield strength, in the 3rd earthquake cycle (Figure 30a). The plastic strength of the deeper part of the upper crust can be reached as the stress accumulates.

After the 25th earthquake cycle, the fault tip reaches the BDTZ (Figure 30c), and plastic deformation occurs over the entire upper crust, except for a small region near the fault. There is a narrow region near the fault where no plastic deformation occurs. In this region, the shear stress never reaches the yield strength because earthquakes

on the fault release the shear stress periodically. We can define the elastic-plastic transition (EPT) between the elastic and plastic deformation regions. The distance of the EPT from the fault changes with time until the reach of regular cycle. For a given plastic strength, the width of the elastic deformation region depends on the value of both the coseismic offsets and the fault tip depth. The larger the stress perturbation of the earthquakes, the wider the elastic deformation zone is. As the fault tip gets closer to the lower crust (e.g. Figure 30c-30e), concentrated plastic deformation occurs at a distance of 3 km to 8 km from the fault. The maximum magnitude of plastic strain accumulated in an interseismic period is ~ 2 times larger than that in the far field where plastic deformation is uniformly distributed.

In each earthquake cycle, plastic deformation concentration in the upper crust near the EPT. In the earthquake cycle model composed of nonlinear Maxwell material, shear stress concentrates at the depth above the BDTZ in the bulk upper crust (e.g., Figure 18e and 18f), which is a result of shear stress relaxation in the visco-elastic lower crust during the interseismic period. Because the concentrated shear stress is larger than the assumed plastic strength, in the model composed of visco-elasto-plastic material, instead of the shear stress, the plastic deformation concentrates in the upper crust.

Figure 31 shows the evolution of plastic deformation rate in an interseismic period after the regular cycle is reached. Right before an earthquake, the shear stress in the plastic deformation regime is uniformly distributed. During the coseismic period, the entire crust behaves elastically. Due to the assumption of the constant plastic

strength and the larger coseismic stress drop in region closer to the fault, right after an earthquake, shear stress in the far field is higher than that in the near field. Because of the stress drop, the shear stress in the entire upper crust becomes smaller than the plastic strength. In the first 900 years of the interseismic period, the plastic strength is not been reached and the entire upper crust behaves elastically, and 1000 years after the last earthquake, the plastic deformation starts to occur in the far field (Figure 31a). As the loading continues, the plastic deformation propagates towards the fault until it reaches the EPT. At the end of the interseismic period at 7 kyr, the plastic deformation concentrates at the EPT. The maximum plastic shear strain rate ($\dot{\epsilon}_{yx}^p$) is about $1.4 \times 10^{-15} \text{ s}^{-1}$ which is about 3 times larger than the plastic shear strain rate in the far field.

The concentrated deformation in the upper crust at the end of an interseismic is unexpected. Here I present a possible explanation for the result. In the model in Chapter 3, I have shown that the fault in the upper crust can be loaded by the basal drag from a localized deformation in the lower crust under the fault during the interseismic period (Figure 22a). The mechanical model of *Kenner and Segall (2000)* shows that the relaxation of the lower crust alone can provide energy for earthquakes to occur in the upper crust. During the interseismic period, the bulk of the upper crust is also affect by the basal drag. As shown in the first row of Figure 23 and the first column of Figure 24, the shear stress is higher at bottom of the elastic upper crust next to the fault. However, in the cases considering the plastic deformation in the upper crust, shear stress is limited by the plastic strength (Figure 29f). In this case, instead of the

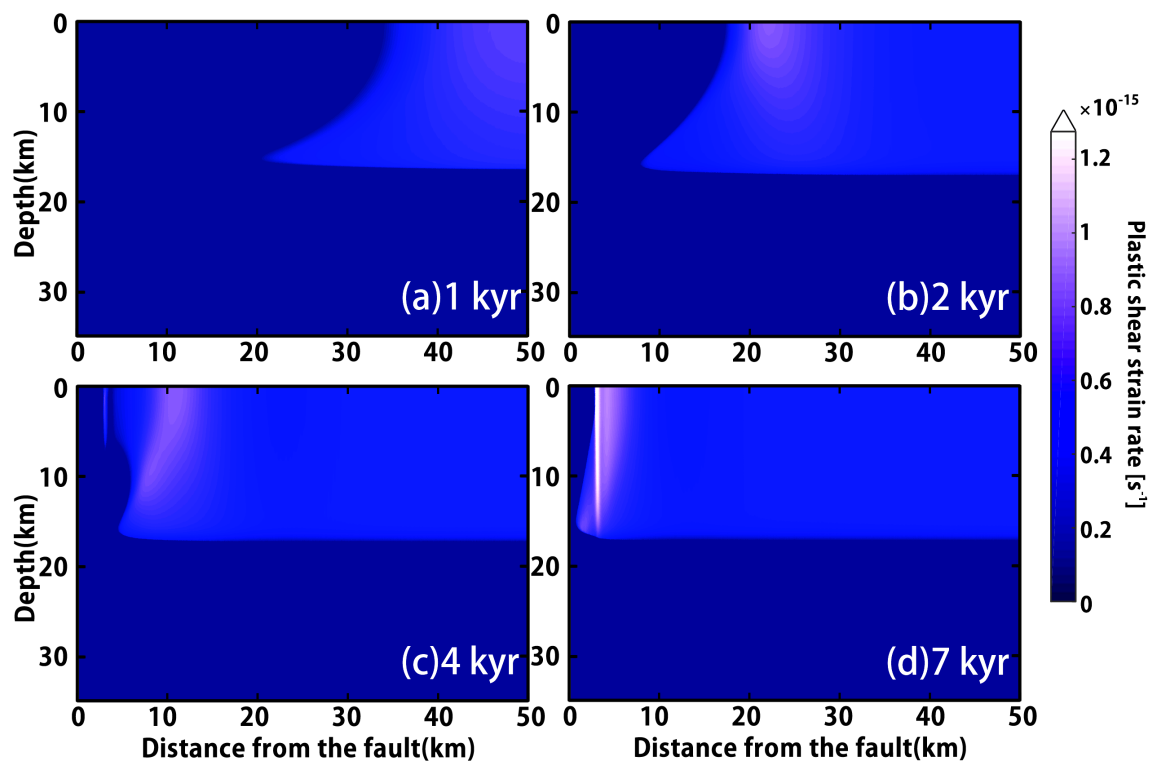


Figure 31: Evolution of the plastic shear strain rate ($\dot{\epsilon}_{yx}^p$) in an earthquake cycle in the case of Q1W_VEP_10 after the regular cycle is reached, the elapsed time in an interseismic period is shown in each figure.

concentrated shear stress, the localized deformation appears near EPT in the upper crust as a result of the basal drag from a localized deformation in the lower crust.

The concentrated deformation near EPT may represent the secondary fault parallel to the main fault. In this study, the plastic strength is only a function of depth. However, in the real world, the shear strength of the crustal materials depends on various properties, such as the roughness of the contact surface, types of fracture and types of rock (e.g. *Barton and Choubey, 1977; Barton, 2013*). Triaxial compression test in the study of *Hallbauer et al. (1973)* shows that the micro fractures in the rock develops under loading. With higher shear strain, more fractures develop in the rock and the strength of rock becomes weaker. By considering the nonlinear relation between shear strain and the strength of rock, the degree of the shear strain concentration in the upper crust near EPT will be higher than the calculation results of this model. If the degree of shear strain concentration is infinitely large, the new strike slip fault parallel to the main fault can be developed. In the current model, the calculation is conducted on a predefined finite element mesh. Because the mesh size in the off-fault area is $\sim 200\text{m}$, the development of a fault in the bulk of the crust cannot be calculated in such a coarse mesh. A new finite element model with adaptive mesh refinement may solve the problems associated with the development of a strike slip fault system.

4.1.4 Effect of the plastic strength on the off-fault plastic deformation

Figure 32 shows the plastic strain ϵ_{yx}^p of all 3 cases at 1.5 Myrs. In the shallow part of the upper crust, plastic strain is larger compared to the that in the deeper part of

the upper crust. Because the positive dependence of plastic strength on depth, plastic deformation starts from the shallow part of the upper crust (Figure 30a- 30c). After the regular cycle has been reached, the plastic strength in the deeper part of the upper crust can be reached by the shear stress, the plastic deformation in an interseismic period after the regular cycle started is uniformly distributed in the far field (Figure 30d and 30e). As a result, difference of plastic strain in the shallower and deeper part of the upper crust becomes less obvious as plastic strain accumulates. Although the plastic deformation concentration can be observed in each earthquake cycle, it is not obvious in the distribution of plastic strain accumulated over multiple earthquake cycle. This is because the localized plastic deformation in each earthquake occurs at the EPT where accumulated plastic deformation is relatively small. In the case of Q1W_VEP_10, Q1W_VEP_15 and Q1W_VEP_20, the maximum plastic strain are 0.013 , 0.01 and 0.007 , respectively. The total plastic strain is larger with smaller plastic strength.

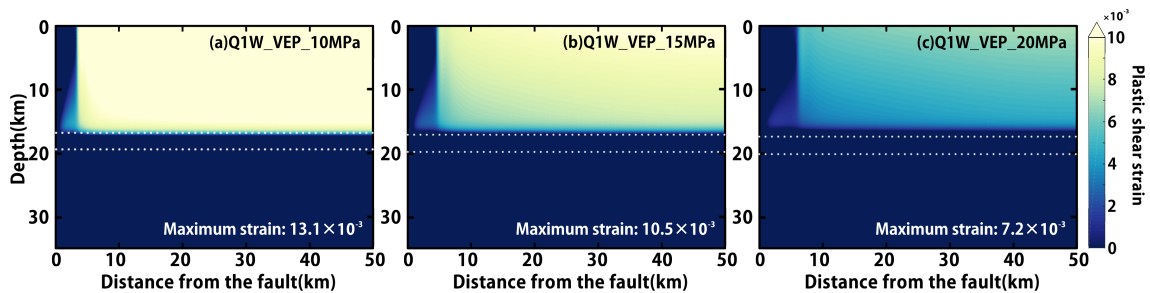


Figure 32: Distribution of plastic strain in the case of Q1W_VEP_10 (a), Q1W_VEP_15 (b) and Q1W_VEP_20 (c) at 1.5 Myrs. The white dot lines indicate the boundaries of the BDTZ.

The width of the elastic deformation region and the thickness of the plastic deformation also depend on the plastic strength. The results are summarized in Table 7. In the case of Q1W_VEP_20, the width of elastic deformation region is more than 2

Table 7: Model properties after regular recurrence starts

Model	Q1W_VEP_10	Q1W_VEP_15	Q1W_VEP_20
Depth of BDTZ [km]	16.7–19.3	17.1–19.8	17.4–20.1
Surface displacement [m]	0.70	0.74	0.76
Recurrence interval [kyr]	7.00	3.55	1.54
Thickness of Plastic deformation zone [km]	17.1	16.8	16.3
Width of elastic deformation zone [km]	2.9	4.3	6.1

times larger than that in the case of Q1W_VEP_10. On the other hand, the thickness of the plastic deformation zone in case Q1W_VEP_20 is only ~ 0.8 km thinner than case Q1W_VEP_10. Because the plastic strength is very sensitive to the depth, The difference is small in the cases with different assumptions of cohesive strength.

4.1.5 Effect of off-fault plastic deformation on fault evolution and recurrence interval

The evolution of the fault behavior in the case of Q1W_VEP_10 is shown in Figure 33. In the first earthquake cycle, the shear stress is lower than the assumed plastic strength. As a result, the model behavior is identical to the case Q1W. The stressing rate in the first earthquake cycle, the coseismic offset of the first earthquake and the shear stress on the fault before the first earthquake (Red lines in Figure 33) are identical to the results in the case Q1W (Red lines in Figure 22). After reaching the plastic strength, the stressing rate on the fault drop from 300 Pa/yr to 115 Pa/yr. After the regular earthquake recurrence starts, due to the basal drag from the plastic deformation of the lower crust, the shear stress accumulation rate in the upper crust is increased to

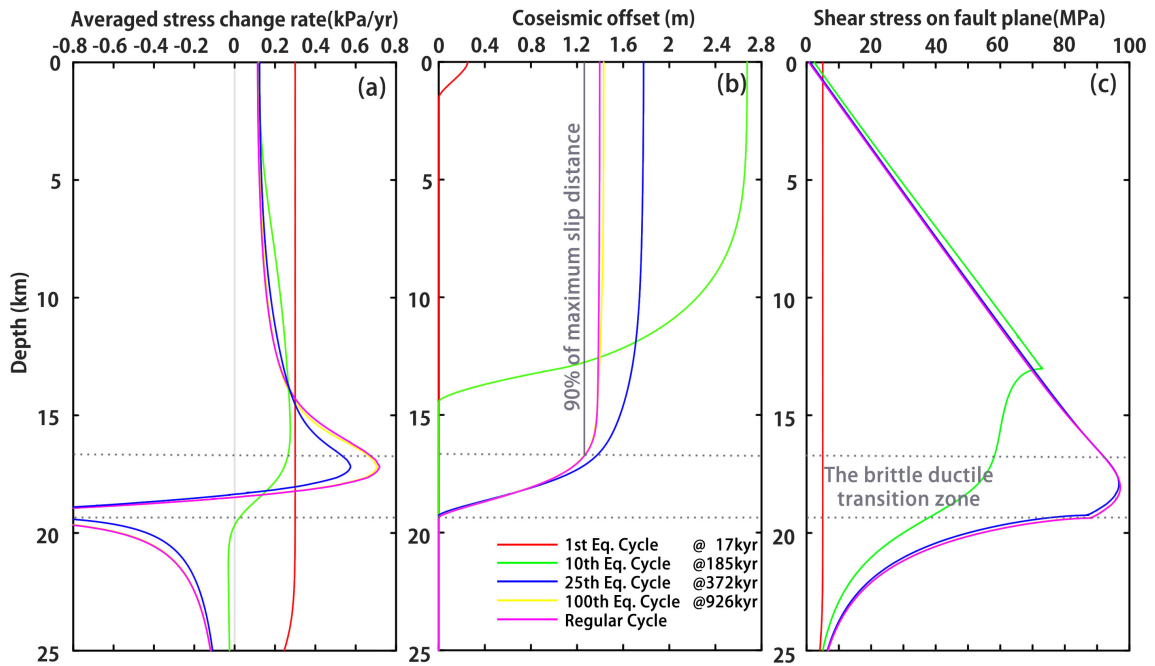


Figure 33: Stress change rate averaged over an earthquake cycle (a), coseismic offset (b) and shear stress on fault plane right before an earthquake. Lines with different colors indicate the result from earthquakes at different time. The gray broken lines indicate the depth of BDTZ.

714 Pa/yr which is significantly smaller than 3000 Pa/yr in the case of Q1W (Figure 22a). Overall, the stressing rate on the fault in the case of Q1W_VEP_10 is smaller than that in the case of Q1W because considerable amount of stress is dissipated by plastic deformation. As a result, the coseismic offsets of earthquake (Figure 33b) are also smaller than that in the case of Q1W (Figure 22b). Figure 33c shows the stress profile on the fault. It is almost identical to the results in Q1W because the stress on the fault is limited by the same assumption of fault strength in case of Q1W and Q1W_VEP_10.

In the simulation of the model with visco-elasto-plastic material, similar to the model with viscoelastic material in the Chapter 3, before the start of regular earth-

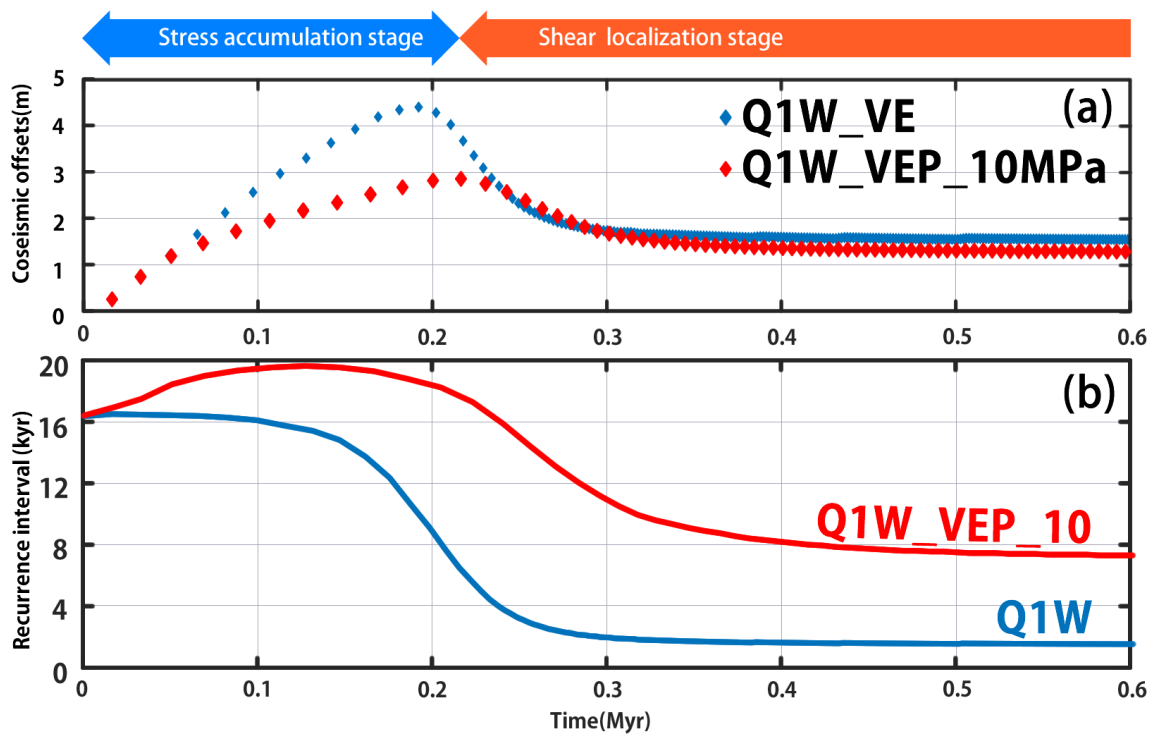


Figure 34: Time evolution of coseismic offset on the surface in each earthquakes (a) and recurrence interval (b) for case Q1W_VEP_10 (Red rhombus dots and lines) and Q1W (Blue rhombus dots and lines). Each rhombus dots in (a) represents an earthquake.

quake cycle, two stages can be defined from the coseismic offsets on the surface (Figure 34a). The stages are defined following the definition in the Chapter 3. In the case of Q1W_VEP_10, the stress accumulation stage starts from the beginning and ends at 0.21 Myr and the shear localization stage starts after the stress accumulation stage and ends at ~ 1 Myr. The time duration of these development stages, especially for the shear localization stage, in case of Q1W_VEP_10 are longer than the case of Q1W. In the case of Q1W_VEP_10, the recurrence interval first increases from 16 kyr to 20 kyr and reduces to 7 kyr due to the basal drag from plastic deformation. Because the fault tip depth increases in the upper crust and localized deformation in the lower crust are earthquake related process, the fault offsets accumulated in each stage are similar in the cases with the same fault strength. Because the recurrence interval is ~ 4 times longer in the case of Q1W_VEP_10 compared to the case of Q1W, the duration of development stage in Q1W_VEP_10 is also 4 times longer than the case of Q1W. For all 3 visco-elastic-plastic cases, the length of the interseismic period after the regular recurrence started are summarized in Table 7.

4.1.6 Effect of off-fault plastic deformation on the geological slip rate

As suggested in previous studies, the off-fault deformation contributes to the discrepancy between geodetic and geological fault slip rates (e.g. *Herbert et al., 2014*). Figure 35 shows the cumulative fault slip of the model with visco-elasto-plastic material compared with the model with viscoelastic material. Similar to the model with viscoelastic material, the geological slip rate in the model with visco-elasto-plastic material

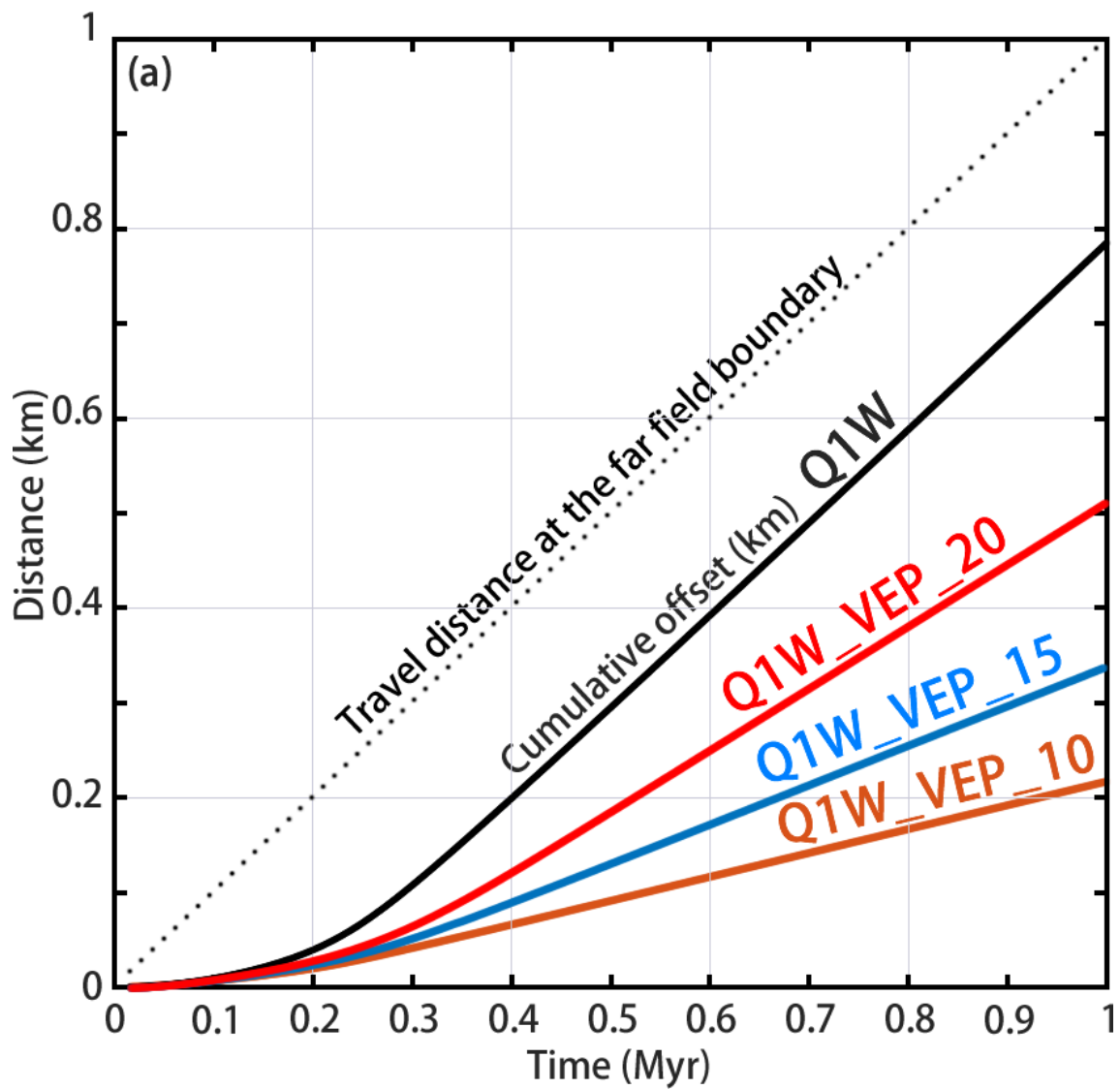


Figure 35: Cumulative fault slip from the case of Q1W (Black line), Q1W_VEP_10 (Orange line), Q1W_VEP_15 (Blue line) and Q1W_VEP_20 (Red line).

increase with time. Because the off-fault plasticity accommodates the relative motion in the far field, the geological slip rate in the model with visco-elasto-plastic material can never catch up with the far field velocity. In the case of Q1W_VEP_10, Q1W_VEP_15 and Q1W_VEP_20, the maximum geological slip rate is 0.23 mm/yr, 0.40 mm/yr and 0.66 mm/yr, respectively. The maximum geological slip rate is very sensitive to the off-fault plastic strength. The geological slip rate can be significantly increased by a few MPa increment of the cohesive strength. In the case when off-fault plastic strength is significantly larger than the fault strength, the difference of the results between the visco-elastic earthquake cycle model and visco-elasto-plastic earthquake cycle will become negligible.

In the model considering no plastic deformation, the discrepancy becomes very small on a strike slip fault with a cumulative offset longer than few hundred meters. On the contrary, in the model considering the plastic deformation in the upper crust, the discrepancy of the geological and geodetic slip rate is a persistent feature. In the intraplate strike slip fault zones whose cumulative offsets larger than few hundred meters, the discrepancy between geodetic and geological fault slip rate is commonly observed (e.g. *Oskin et al., 2008*; *Ohzono et al., 2011*). These observations suggest that the off-fault plastic strength is only slightly stronger than the fault strength. In a strike slip fault system, as suggested by *Herbert et al. (2014)*, off-fault plastic deformation should be considered as an important mechanism to reconcile the observed discrepancy between the geological and geodetic deformation.

4.2 Can the mantle flow load the continental crust ?

In the previous chapters, I assumed that the continental crust is loaded by the far field relative motion. As I have shown in Chapter 4.1, with plastic deformation in the upper crust, the deformation due to the relative motion may be accommodated by the plastic deformation. The efficiency of the stress transfer from the far field boundary is very low in the case when off-fault plastic strength is only slightly larger than the strength of the main fault. In the region far away from the continental crust, it is necessary to consider whether or not the mantle flow alone can load the continental crust.

In this model, the model geometry is the same as the model in Chapter 4.1 (Figure 28). In this calculation, The boundary conditions are assumed as follows: as for the far field boundary, I assume the stress free condition: $\dot{\epsilon}_{yx}^e = 0$. At Moho, I assume a constant shear strain rate: $\dot{\epsilon}_{yx} = 0.01\text{ppm/yr}$.

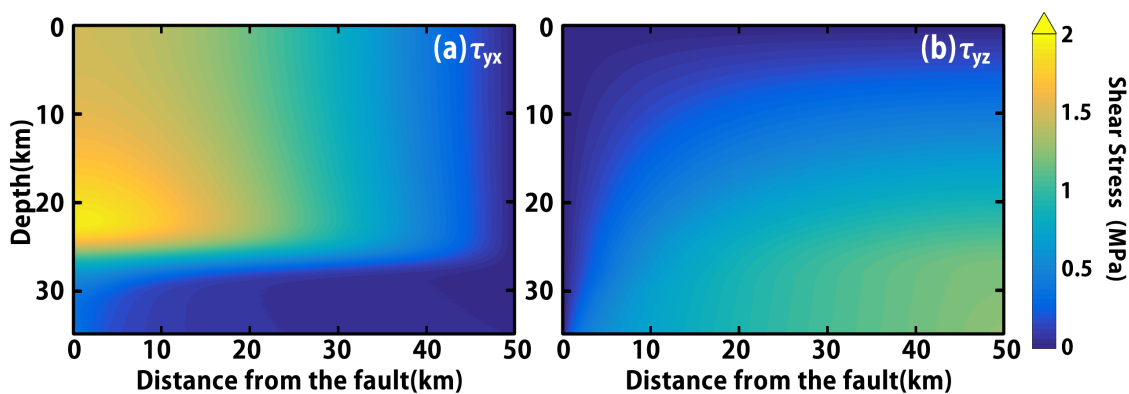


Figure 36: Shear stress (a) τ_{yx} and (b) τ_{yz} in the crust after 20 kyrs of loading from upper mantle. Wet quartz rheology (Table 4) is assumed in this calculation.

The calculation of shear stress starts from a stress free condition. Figure 36 shows the distribution of shear stress τ_{yx} (a) and τ_{yz} (b) component in the crust at 20 kyr. The

rock rheology in this calculation is assumed to be wet quartz (Table 4). The maximum value of the shear stress τ_{yx} (Figure 36a) in the crust is ~ 2 MPa and the shear stress near the surface is about 1.5MPa. The shear stress τ_{yx} in the crust at depth shallower than ~ 25 km increase as a result the plastic flow in the lower crust. Because the velocity at the depth of Moho increases with distance of the fault, the shear stress τ_{yz} increase with the depth and the distance from the fault. The maximum value of the shear stress τ_{yz} is ~ 1 MPa and it is almost zero near the surface. The shear stress dose not increase after ~ 20 kyrs because the elastic upper crust is decoupled from the mantle flow. Figure 37 shows the distribution of the effective viscosity at 20 kyrs. In the deepest part of the crust near Moho, the effective viscosity is less than $\sim 10^{21}$ Pa s. The material with such a small effective viscosity deforms plastically. As a result, the elastic upper crust can not be effectively loaded by the mantle flow.

In order to load the crust effectively from the upper mantle, the effective viscosity in the deeper part of the crust has to be large enough ($> 10^{25}$ Pa s) so that crustal rocks deform elastically. This condition can be achieved by assuming the dry anorthite rheology for the entire crust (Table 2). Figure 38 shows shear stress distribution at 440 kyr in the case of dry anorthite. In the case assuming dry anorthite, the maximum shear stress is ~ 100 times larger than that in the case assuming wet quartz rheology. Because there is no plastic lower crust, the fault tip depth increases with time until it reaches the depth of Moho at 58th earthquake.

The situation described in the case assuming dry anorthite is not likely to exist in the continental crust. In the stable continental regions, large earthquakes do not occur

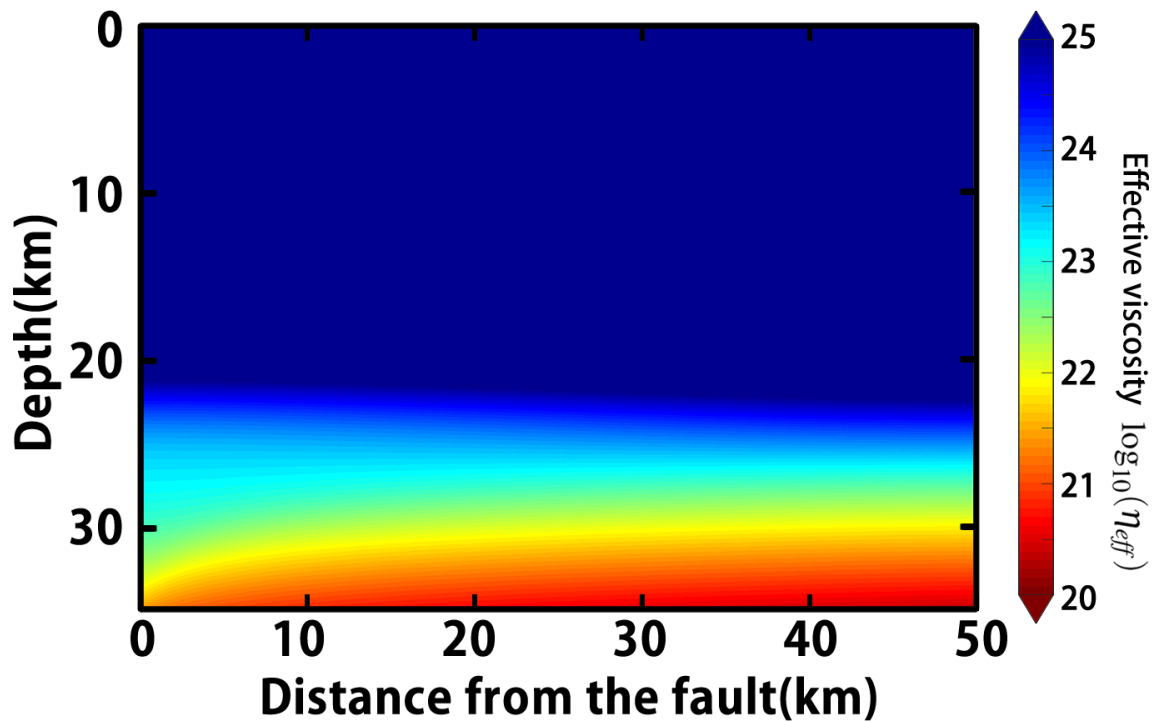


Figure 37: Effective viscosity in the crust after 20 kyr of loading from upper mantle. Wet quartz rheology (Table 4) is assumed in this calculation.

in the interior of the craton where an anhydrous crust overlaying an anhydrous upper mantle which provides the mechanical stability of the entire lithosphere (*Mooney et al., 2012*). In the active continental regions, the focal depth of the earthquakes are shallower than 25 km (*Wright et al., 2013*) which is consistent with the results of the BDTZ depth in Chapter 3. By considering the weakening effect of the water using water fugacity, the depth of the bottom BDTZ can be reduced by 8 km from ~ 27 km to ~ 19 km according to the results in the Chapter 2. These results indicate that the strength of the lower crust is significantly lowered by water. Therefore, the continental crust is unlikely to be loaded by the upper mantle.

On the other hand, the thin (~ 10 km, (*Laske et al., 2013*)) and cold oceanic crust can be effectively driven by the mantle flow (*Lithgow-Bertelloni and Guynn, 2004*). In

the interior of the oceanic plate, mantle flow can be one of the main sources of stress for large intraplate strike slip earthquakes, such as the 2012 Indian Ocean earthquake (Duputel *et al.*, 2012).

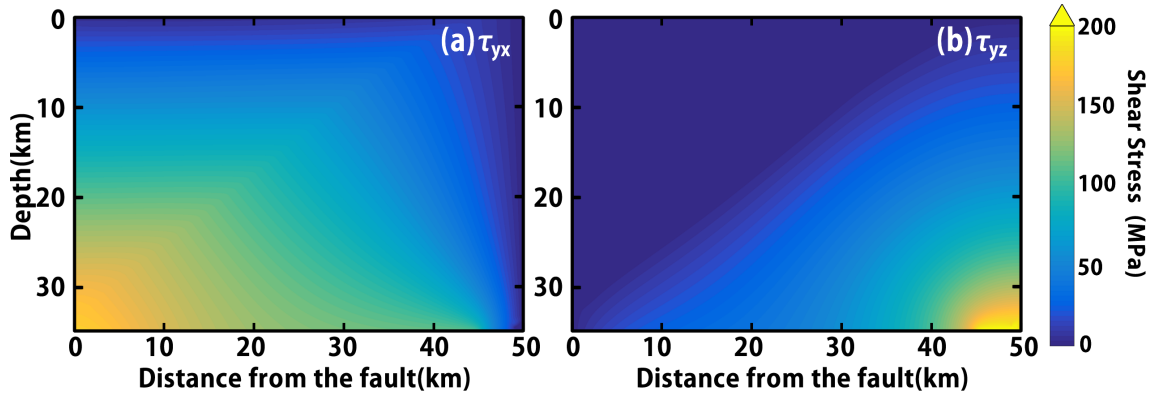


Figure 38: Shear stress (a) τ_{yx} and (b) τ_{yz} in the crust after 440 kyrs of loading from upper mantle. Dry Anorthite rheology (Table 2) is assumed in this calculation.

4.3 Deformation around a small intraplate strike slip fault

The model in the current study assumes an infinitely long strike slip fault and the deformation in the current model is simulated in two dimensional space. For an intraplate strike slip fault whose length is shorter than a few tens of kilometers, it is important to note that the two dimensional anti-plane geometry which is used to approximate a very long strike slip fault may not be appropriate for a short intraplate strike slip fault. For a short strike slip fault who has a length to width (fault tip depth) ratio of ~ 1 , the stress perturbation due to the fault ends has a significant influence on the stress field around the fault (King *et al.*, 1994). Even on a long strike slip fault, whose length is several tens and hundreds of kilometers, the fault ends may also affect fault behavior.

For large intraplate strike slip earthquakes, a linear relation between fault length and the mean coseismic slip distance has been pointed out by *Scholz (1982)*. However, the evolution of the fault length and the role of the earthquakes in developing a strike slip fault in three dimensional space is not well understood. In the mechanical models assuming an elastic upper crust, occurrence of an intraplate strike slip earthquake will result in a large stress concentration at the fault ends (e.g. *Iio and Kobayashi, 2002*). The calculated shear stress at the fault ends after an earthquake is significantly larger than the plastic strength of the crustal rock because the inelastic deformation is not considered in the model.

In the earth's crust, inelastic deformation in the upper crust occurs to ensure that elastic stress does not exceed the strength of the crustal rocks. Near the fault ends, different kind of structures, such as the normal and the reverse faults, develop as a result of the intraplate strike slip faulting (*Storti et al., 2003*). By considering the plastic deformation in the upper crust, the iterative method (Figure 17) in this study can be used to eliminate the stress concentration near the fault ends. To understand the behaviors of a short intraplate strike slip fault, future studies need to include the fault ends in a three-dimensional mechanical model. Using such a model, it is possible to understand the evolution of the geological structures in both elasto-plastic upper crust and viscoelastic lower crust near the fault ends and the role fault related structures play in the evolution of an intraplate strike slip fault.

4.4 Implication for the earthquake activities

Large intraplate strike slip earthquakes are rare compared to the interplate strike slip earthquakes. In the previous studies of intraplate earthquake activities (e.g. *Matsuda, 1977*), the recurrence interval of the earthquakes on these fault has been estimated following the relation proposed by *Wallace (1970)*:

$$R = \frac{d}{S - C}, \quad (4.3)$$

where R is the recurrence interval, d is the displacement of an earthquake, S is the long-term slip rate and C is the tectonic creep rate. Based on the observed geological slip rate, the intraplate faults in Japan island has been classified into class A ($1\text{mm/yr} < v \leq 10\text{mm/yr}$), class B ($0.1\text{mm/yr} < v \leq 1\text{mm/yr}$) or class C ($0.01\text{mm/yr} < v \leq 0.1\text{mm/yr}$) (*Research Group for Active Faults of Japan, 1991*).

According to the relation proposed by *Wallace (1970)*, the earthquake on the C-class active faults, whose geological slip rate are 2 orders smaller than the A-class active faults, should be much less frequent than the earthquake on A-class active faults. More than 100 years of observation on the earthquake activities shows that similar number of large earthquakes occur on the fault in different classes, which suggests that the number of the C-class active faults should be 2 orders of magnitude more than the number of the A-class active faults. However, the identified C-class active faults from geological survey in Japan are much less than the expectation (*Asada, 1996*).

In the models of this study, the coseismic offsets of earthquakes change with time. When the fault slip distance of an earthquake reaches its maximum at the end of stress

accumulation stage (Figure 34), the cumulative offset is ~ 40 meters in the case assuming no plastic deformation in the upper crust and it is even smaller in the cases assuming visco-elasto-plastic materials. The smaller the off-fault plastic strength is, the shorter the cumulative offset on the main strike slip fault. After the localized deformation formed in the lower crust, the coseismic offsets on the surface drops from few meters to ~ 1.5 m. Earthquakes with large coseismic offsets occur only in the period after the fault tip reaches the depth of the BDTZ and before the development of localized deformation in the lower crust. These results suggest that large earthquakes with averaged offsets of few meters are possible on the young faults with small cumulative offsets ranging from 50m to 100m. In the Japanese islands, although large amount of faults have been well documented by geological surveys, many unexpected strike-slip earthquakes, such as the 1927 Kita Tango earthquake and the 1943 Tottori earthquake, occur in the region where there are no surface expressions of faulting before the earthquake (*Kanamori, 1973*). Because of the long recurrence interval ($> 10^4$ years) of the intraplate strike slip earthquakes, the offsets created by earthquakes can be obscured by sedimentation during the interseismic period which makes it very difficult to identify the existence of a fault (e.g. *Kaneda, 2003; Talebian et al., 2004*). In the continental crust, many developing intraplate strike slip faults have not been identified and therefore, the seismic hazard in the regions with no evidence of active faults may be underestimated.

Chapter 5

Conclusions

I studied the evolution of the deformation in the continental crust across an intraplate strike slip fault. First, I developed a thermo-mechanical model to study the evolution of the lower crustal deformation in the geological timescale. In the lower crust under an intraplate strike slip fault, the localized deformation is developed by the intraplate faulting in the upper crust. Several shear strain concentration mechanisms, which include the thermal weakening, grain size reduction and power law rheology, have been considered in the development of the localized deformation in the lower crust under the intraplate strike slip fault. Although the thermal weakening has been considered very important in the development of shear zone under an interplate strike slip fault due to the Arrhenius temperature dependency of the effective viscosity of the rock. However, in the case of the intraplate strike slip fault case, due to the small temperature increase, the effect of thermal weakening is negligible on the degree of the shear localization in the lower crust. On the other hand, the power law rheology has a significant impact on the deformation in the lower crust under an intraplate strike slip fault. The degree of shear strain concentration in the cases considering the power law

rheology is higher than the linear case. The strength of the lower crust in the shear zone is significantly lowered by the power law creep. The grain size can be reduced to a value less than a few hundred micrometers in the process of dynamic recrystallization in dislocation creep regime, and the small recrystallized grains are important for maintaining a shear zone on a geological time scale of $\sim 10^8$ years.

The localized deformation in the lower crust developed by earthquakes can also affect the deformation in the upper crust. In the mechanical model I developed for the evolution of the earthquake cycle, I investigate the stress build-up process in an initially stress-free crust-mantle system in the geological timescale. Due to the tectonic loading in the far field, the stress builds up in the crust and the upper-mantle. At the beginning when shear stress is small (few MPa), the stressing rate in the entire model is a constant. Due to the plastic flow, the stressing rate reduced to zero in the lower crust and the upper mantle. The fault tip depth increase with time and development of the localized deformation starts after the fault tip reaches the depth of the BDTZ. As the concentrated deformation developed in the lower crust, the recurrence interval decreases by an order of magnitude from 16 kyrs to about 1.6 kyrs due to the basal drag from localized deformation in the lower crust. Under a strike slip fault, time to develop a shear zone with large shear strain is much longer than the time for the deformation to concentrates under the fault. Shear zone under a young intraplate strike slip fault whose cumulative offset less than a few hundred meters may not be detectable with geological and geophysical observations.

In the case with visco-elastic material, the shear strain in the lower crustal shear

zone is directly related to the cumulative offsets. Compared to interplate strike slip fault, shear zone under an slowly deforming intraplate strike slip fault needs a much longer time to develop. In the cases with visco-elasto-plastic material, due to the plastic deformation in the upper crust, the stressing rate on the fault is smaller compared to that in the cases with visco-elastic material. Although the time to develop a localized deformation in the cases with visco-elasto-plastic material deformation is longer than that in the case with visco-elastic material, the relation between the cumulative offsets and the degree of shear concentration is not changed. Under the intraplate strike slip fault with more than few hundred meters of cumulative offset, even without any observational evidence for the lower crustal shear zone, localized deformation is likely to occur under the fault. With a localized deformation under the fault, the elastic screw dislocation model (*Savage and Burford, 1973*) can be used to explain the geodetically observed deformation across the fault. Our model provides a physical explanation of the validity of the screw dislocation model.

In this model, the evolution of the intraplate strike slip faulting, the development of the shear zone in the lower crust and the tectonic stress build-up have been successfully reproduced. The results of the model suggest that geological fault slip rate of an intraplate strike slip fault increase with time. This result provides another explanation to the discrepancy between the geodetic and geological fault slip rates. This model demonstrates the importance of considering the whole mechanical system of the crust in which rheological properties, thermal structure, and fault activities are interactive one another for better understanding of crustal seismogenesis.

Bibliography

- Allison, K. L., and E. M. Dunham (2018), Earthquake cycle simulations with rate- and-state friction and power-law viscoelasticity, *Tectonophysics*, 733, 232 – 256, doi:[10.1016/j.tecto.2017.10.021](https://doi.org/10.1016/j.tecto.2017.10.021).
- Asada, T. (1996), Numbers of c class faults on land in Japan:some questions on active faults (2), *Active Fault Research*, 1996(14), 107–107, doi:[10.11462/afr1985.1996.14_107](https://doi.org/10.11462/afr1985.1996.14_107).
- Atwater, T. (1970), Implications of plate tectonics for the cenozoic tectonic evolution of western north America, *Geological Society of America Bulletin*, 81(12), 3513–3536, doi: [10.1130/0016-7606\(1970\)81\[3513:IOPTFT\]2.0.CO;2](https://doi.org/10.1130/0016-7606(1970)81[3513:IOPTFT]2.0.CO;2).
- Atwater, T. (1989), Plate tectonic history of the northeast pacific and western north America, in *The Eastern Pacific Ocean and Hawaii*, The Geological Society of America, Inc., doi:[10.1130/DNAG-GNA-N.21](https://doi.org/10.1130/DNAG-GNA-N.21).
- Barton, N. (1976), The shear strength of rock and rock joints, *International Journal of Rock Mechanics and Mining Sciences & Geomechanics Abstracts*, 13(9), 255 – 279, doi:[10.1016/0148-9062\(76\)90003-6](https://doi.org/10.1016/0148-9062(76)90003-6).

- Barton, N. (2013), Shear strength criteria for rock, rock joints, rockfill and rock masses: Problems and some solutions, *Journal of Rock Mechanics and Geotechnical Engineering*, 5(4), 249 – 261, doi:[10.1016/j.jrmge.2013.05.008](https://doi.org/10.1016/j.jrmge.2013.05.008).
- Barton, N., and V. Choubey (1977), The shear strength of rock joints in theory and practice, *Rock mechanics*, 10(1), 1–54, doi:[10.1007/BF01261801](https://doi.org/10.1007/BF01261801).
- Becken, M., and O. Ritter (2012), Magnetotelluric studies at the San Andreas fault zone: Implications for the role of fluids, *Surveys in Geophysics*, 33(1), 65–105, doi:[10.1007/s10712-011-9144-0](https://doi.org/10.1007/s10712-011-9144-0).
- Boullier, A., and Y. Gueguen (1975), Sp-mylonites: origin of some mylonites by superplastic flow, *Contributions to Mineralogy and Petrology*, 50(2), 93–104, doi:[10.1007/BF00373329](https://doi.org/10.1007/BF00373329).
- Bourne, S., P. England, and B. Parsons (1998), The motion of crustal blocks driven by flow of the lower lithosphere and implications for slip rates of continental strike-slip faults, *Nature*, 391(6668), 655, doi: [10.1038/35556](https://doi.org/10.1038/35556).
- Bürgmann, R., and G. Dresen (2008), Rheology of the lower crust and upper mantle: Evidence from rock mechanics, geodesy, and field observations, *Ann. Rev. Earth Planet. Sci.*, 36(1), 531, doi:[10.1146/annurev.earth.36.031207.124326](https://doi.org/10.1146/annurev.earth.36.031207.124326).
- Buzbee, B. L., G. H. Golub, and C. W. Nielson (1970), On direct methods for solving poisson's equations, *SIAM Journal on Numerical analysis*, 7(4), 627–656, doi:[10.1137/0707049](https://doi.org/10.1137/0707049).

Byerlee, J. D. (1978), Friction of rocks, *Pure Appl. Geophys.*, 116(4-5), 615–626, doi:
[10.1007/BF00876528](https://doi.org/10.1007/BF00876528).

Chester, F. M., J. P. Evans, and R. L. Biegel (1993), Internal structure and weakening mechanisms of the San Andreas fault, *Journal of Geophysical Research: Solid Earth*, 98(B1), 771–786, doi:[10.1029/92JB01866](https://doi.org/10.1029/92JB01866).

Childs, C., T. Manzocchi, J. J. Walsh, C. G. Bonson, A. Nicol, and M. P. Schöpfer (2009), A geometric model of fault zone and fault rock thickness variations, *Journal of Structural Geology*, 31(2), 117 – 127, doi:[10.1016/j.jsg.2008.08.009](https://doi.org/10.1016/j.jsg.2008.08.009).

Cowgill, E., A. Yin, T. M. Harrison, and W. Xiao-Feng (2003), Reconstruction of the altyn tagh fault based on u-pb geochronology: Role of back thrusts, mantle sutures, and heterogeneous crustal strength in forming the tibetan plateau, *Journal of Geophysical Research: Solid Earth*, 108(B7), doi: [10.1029/2002JB002080](https://doi.org/10.1029/2002JB002080).

De Bresser, J., C. Peach, J. Reijs, and C. Spiers (1998), On dynamic recrystallization during solid state flow: Effects of stress and temperature, *Geophysical Research Letters*, 25(18), 3457–3460, doi:[10.1029/98GL02690](https://doi.org/10.1029/98GL02690).

De Bresser, J., J. Ter Heege, and C. Spiers (2001), Grain size reduction by dynamic recrystallization: can it result in major rheological weakening?, *International Journal of Earth Sciences*, 90(1), 28–45, doi:[10.1007/s005310000149](https://doi.org/10.1007/s005310000149).

DeMets, C., and T. H. Dixon (1999), New kinematic models for pacific-north America motion from 3 ma to present, i: Evidence for steady motion and bi-

ases in the nuvel-1a model, *Geophysical Research Letters*, 26(13), 1921–1924, [doi:10.1029/1999GL900405](https://doi.org/10.1029/1999GL900405).

DeMets, C., R. G. Gordon, D. F. Argus, and S. Stein (1994), Effect of recent revisions to the geomagnetic reversal time scale on estimates of current plate motions, *Geophysical research letters*, 21(20), 2191–2194, [doi:10.1029/94GL02118](https://doi.org/10.1029/94GL02118).

DESERT Group, M. Weber, K. Abu-Ayyash, A. Abueladas, A. Agnon, H. Al-Amoush, A. Babeyko, Y. Bartov, M. Baumann, Z. Ben-Avraham, G. Bock, J. Bribach, R. El-Kelani, A. Förster, H.-J. Förster, U. Frieslander, Z. Garfunkel, S. Grunewald, H. J. Götze, V. Haak, C. Haberland, M. Hassouneh, S. Helwig, A. Hofstetter, K.-H. Jäckel, D. Kesten, R. Kind, N. Maercklin, J. Mechie, A. Mohsen, F. M. Neubauer, R. Oberhänsli, I. Qabbani, O. Ritter, G. Rümpker, M. Rybakov, T. Ryberg, F. Scherbaum, J. Schmidt, A. Schulze, S. Sobolev, M. Stiller, H. Thoss, U. Weckmann, and K. Wylegalla (2004), The crustal structure of the dead sea transform, *Geophysical Journal International*, 156(3), 655–681, [doi:10.1111/j.1365-246X.2004.02143.x](https://doi.org/10.1111/j.1365-246X.2004.02143.x).

DeVries, P. M. R., and B. J. Meade (2013), Earthquake cycle deformation in the tibetan plateau with a weak mid-crustal layer, *Journal of Geophysical Research: Solid Earth*, 118(6), 3101–3111, [doi:10.1002/jgrb.50209](https://doi.org/10.1002/jgrb.50209).

Doke, R., S. Tanikawa, K. Yasue, A. Nakayasu, T. Niizato, K. Umeda, and T. Tanaka (2012), Spatial patterns of initiation ages of active faulting in the Japanese islands, *Active Fault Research*, 37, 1–15, [doi: 10.11462/afr.2012.37_1](https://doi.org/10.11462/afr.2012.37_1).

- Dresen, G., Z. Wang, and Q. Bai (1996), Kinetics of grain growth in anorthite, *Tectonophysics*, 258(1-4), 251–262, doi:10.1016/0040-1951(95)00203-0.
- Duputel, Z., H. Kanamori, V. C. Tsai, L. Rivera, L. Meng, J.-P. Ampuero, and J. M. Stock (2012), The 2012 sumatra great earthquake sequence, *Earth and Planetary Science Letters*, 351-352, 247 – 257, doi:10.1016/j.epsl.2012.07.017.
- Elvira, P., C. D. G., and R. Nicholas (2017), Seismic tomography of the North Anatolian Fault: New insights into structural heterogeneity along a continental strike-slip fault, *Geophysical Research Letters*, 44(5), 2186–2193, doi:10.1002/2017GL072726.
- Erickson, B. A., E. M. Dunham, and A. Khosravifar (2017), A finite difference method for off-fault plasticity throughout the earthquake cycle, *Journal of the Mechanics and Physics of Solids*, 109, 50 – 77, doi:10.1016/j.jmps.2017.08.002.
- Fialko, Y., D. Sandwell, M. Simons, and P. Rosen (2005), Three-dimensional deformation caused by the bam, iran, earthquake and the origin of shallow slip deficit, *Nature*, 435(7040), 295, doi: 10.1038/nature03425.
- Fleitout, L., and C. Froidevaux (1980), Thermal and mechanical evolution of shear zones, *Journal of Structural Geology*, 2(1-2), 159–164, doi:10.1016/0191-8141(80)90046-2.
- Freed, A. M., R. Bürgmann, and T. Herring (2007), Far-reaching transient motions after mojave earthquakes require broad mantle flow beneath a strong crust, *Geophysical Research Letters*, 34(19), doi:10.1029/2007GL030959.

- Fusseis, F., M. Handy, and C. Schrank (2006), Networking of shear zones at the brittle-to-viscous transition (cap de creus, ne spain), *Journal of Structural Geology*, 28(7), 1228 – 1243, doi:10.1016/j.jsg.2006.03.022.
- Gourmelen, N., T. H. Dixon, F. Amelung, and G. Schmalzle (2011), Acceleration and evolution of faults: An example from the hunter mountain-panamint valley fault zone, eastern California, *Earth and Planetary Science Letters*, 301(1), 337 – 344, doi:10.1016/j.epsl.2010.11.016.
- Gueydan, F., Y. M. Leroy, and L. Jolivet (2001), Grain-size-sensitive flow and shear-stress enhancement at the brittle–ductile transition of the continental crust, *International Journal of Earth Sciences*, 90(1), 181–196, doi: 10.1007/s005310000.
- Hallbauer, D., H. Wagner, and N. Cook (1973), Some observations concerning the microscopic and mechanical behaviour of quartzite specimens in stiff, triaxial compression tests, *International Journal of Rock Mechanics and Mining Sciences & Geomechanics Abstracts*, 10(6), 713 – 726, doi:10.1016/0148-9062(73)90015-6.
- Henstock, T. J., A. Levander, and J. A. Hole (1997), Deformation in the lower crust of the San Andreas fault system in northern California, *Science*, 278(5338), 650–653, doi:10.1126/science.278.5338.650.
- Herbert, J. W., M. L. Cooke, M. Oskin, and O. Difo (2014), How much can off-fault deformation contribute to the slip rate discrepancy within the eastern California shear zone?, *Geology*, 42(1), 71, doi:10.1130/G34738.1.

- Hillert, M. (1988), Inhibition of grain growth by second-phase particles, *Acta Metallurgica*, 36(12), 3177–3181, doi:10.1016/0001-6160(88)90053-3.
- Hirth, G., and D. Kohlstedt (2013), Rheology of the upper mantle and the mantle wedge: A view from the experimentalists, *Inside the Subduction Factory*, pp. 83–105, doi:10.1029/138GM06.
- Iio, Y. (1997), Frictional coefficient on faults in a seismogenic region inferred from earthquake mechanism solutions, *Journal of Geophysical Research: Solid Earth*, 102(B3), 5403–5412, doi:10.1029/96JB03593.
- Iio, Y., and Y. Kobayashi (2002), A physical understanding of large intraplate earthquakes, *Earth, Planets and Space*, 54(11), 1001–1004, doi:10.1186/BF03353292.
- Johnson, K. M., and P. Segall (2004), Viscoelastic earthquake cycle models with deep stress-driven creep along the San Andreas fault system, *Journal of Geophysical Research: Solid Earth*, 109(B10), doi:10.1029/2004JB003096.
- Kanamori, H. (1973), Mode of strain release associated with major earthquakes in Japan, *Annual Review of Earth and Planetary Sciences*, 1(1), 213–239, doi:10.1146/annurev.ea.01.050173.001241.
- Kaneda, H. (2003), Threshold of geomorphic detectability estimated from geologic observations of active low slip-rate strike-slip faults, *Geophysical Research Letters*, 30(5), doi:10.1029/2002GL016280.

- Karato, S. (2008), *Deformation of earth materials: an introduction to the rheology of solid earth*, Cambridge University Press, doi: [10.1017/CBO9780511804892](https://doi.org/10.1017/CBO9780511804892).
- Kenner, S. J., and P. Segall (2000), A mechanical model for intraplate earthquakes: Application to the new madrid seismic zone, *Science*, 289(5488), 2329–2332, doi: [10.1126/science.289.5488.2329](https://doi.org/10.1126/science.289.5488.2329).
- King, G. C., R. S. Stein, and J. Lin (1994), Static stress changes and the triggering of earthquakes, *Bulletin of the Seismological Society of America*, 84(3), 935–953.
- Kirby, S., and A. Kronenberg (1987), Rheology of the lithosphere: selected topics, *Reviews of Geophysics*, 25(6), 1219–1244, doi:[10.1029/RG025i006p01219](https://doi.org/10.1029/RG025i006p01219).
- Kohlstedt, D. L., B. Evans, and S. J. Mackwell (1995), Strength of the lithosphere: Constraints imposed by laboratory experiments, *Journal of Geophysical Research: Solid Earth*, 100(B9), 17,587–17,602, doi:[10.1029/95JB01460](https://doi.org/10.1029/95JB01460).
- Lachenbruch, A. H., and J. Sass (1980), Heat flow and energetics of the San Andreas fault zone, *Journal of Geophysical Research: Solid Earth (1978–2012)*, 85(B11), 6185–6222, doi: [10.1029/JB085iB11p06185](https://doi.org/10.1029/JB085iB11p06185).
- Lambert, V., and S. Barbot (2016), Contribution of viscoelastic flow in earthquake cycles within the lithosphere-asthenosphere system, *Geophysical Research Letters*, 43(19), 10,142–10,154, doi:[10.1002/2016GL070345](https://doi.org/10.1002/2016GL070345).
- Laske, G., G. Masters, Z. Ma, and M. Pasyanos (2013), Update on CRUST1.0 - A 1-degree Global Model of Earth's Crust, in *EGU General Assembly Conference*

Abstracts, EGU General Assembly Conference Abstracts, vol. 15, pp. EGU2013–2658.

Leloup, P. H., Y. Ricard, J. Battaglia, and R. Lacassin (1999), Shear heating in continental strike-slip shear zones: model and field examples, *Geophysical Journal International*, 136(1), 19–40, doi:[10.1046/j.1365-246X.1999.00683.x](https://doi.org/10.1046/j.1365-246X.1999.00683.x).

Lithgow-Bertelloni, C., and J. Guynn (2004), Origin of the lithospheric stress field, *Journal of Geophysical Research: Solid Earth*, 109(B1), doi:[10.1029/2003JB002467](https://doi.org/10.1029/2003JB002467).

Little, T., R. Holcombe, and B. Ilg (2002), Kinematics of oblique collision and ramping inferred from microstructures and strain in middle crustal rocks, central southern alps, New Zealand, *Journal of Structural Geology*, 24(1), 219–239, doi:[10.1016/S0191-8141\(01\)00060-8](https://doi.org/10.1016/S0191-8141(01)00060-8).

Markl, G. (1998), The eidsfjord anorthosite, vesterålen, norway: field observations and geochemical data, *Norges Geologiske Undersøkelse Bulletin*, 434, 53–75.

Matsuda, T. (1977), Estimation of future destructive earthquakes from active faults on land in Japan, *Journal of Physics of the Earth*, 25(Supplement), S251–S260, doi:[10.4294/jpe1952.25.Supplement_S251](https://doi.org/10.4294/jpe1952.25.Supplement_S251).

Meade, B. J., and B. H. Hager (2005), Block models of crustal motion in southern California constrained by gps measurements, *Journal of Geophysical Research: Solid Earth*, 110(B3), doi:[10.1029/2004JB003209](https://doi.org/10.1029/2004JB003209).

- Meade, B. J., Y. Klinger, and E. A. Hetland (2013), Inference of multiple earthquake-cycle relaxation timescales from irregular geodetic sampling of interseismic deformation, *Bulletin of the Seismological Society of America*, 103(5), 2824, [doi:10.1785/0120130006](https://doi.org/10.1785/0120130006).
- Melosh, H. J. (1976), Nonlinear stress propagation in the earth's upper mantle, *Journal of Geophysical Research*, 81(32), 5621–5632, [doi:10.1029/JB081i032p05621](https://doi.org/10.1029/JB081i032p05621).
- Montési, L. G., and G. Hirth (2003), Grain size evolution and the rheology of ductile shear zones: from laboratory experiments to postseismic creep, *Earth and Planetary Science Letters*, 211(1), 97–110, [doi:10.1016/S0012-821X\(03\)00196-1](https://doi.org/10.1016/S0012-821X(03)00196-1).
- Mooney, W. D., J. Ritsema, and Y. K. Hwang (2012), Crustal seismicity and the earthquake catalog maximum moment magnitude (m_{cmax}) in stable continental regions (scrs): Correlation with the seismic velocity of the lithosphere, *Earth and Planetary Science Letters*, 357-358, 78 – 83, [doi:10.1016/j.epsl.2012.08.032](https://doi.org/10.1016/j.epsl.2012.08.032).
- Moore, J. D., and B. Parsons (2015), Scaling of viscous shear zones with depth-dependent viscosity and power-law stress-strain-rate dependence, *Geophysical Journal International*, 202(1), 242–260, [doi:10.1093/gji/ggv143](https://doi.org/10.1093/gji/ggv143).
- Nakajima, J., and A. Hasegawa (2007), Deep crustal structure along the niigata-kobe tectonic zone, Japan: Its origin and segmentation, *Earth, Planets and Space*, 59(2), e5–e8, [doi:10.1186/BF03352677](https://doi.org/10.1186/BF03352677).
- Nakajima, J., A. Kato, T. Iwasaki, S. Ohmi, T. Okada, and T. Takeda (2010), Deep crustal structure around the atotsugawa fault system, central Japan: A weak zone

- below the seismogenic zone and its role in earthquake generation, *Earth, Planets and Space*, 62(7), 555–566, doi:10.5047/eps.2010.06.007.
- Norris, R. J., and V. G. Toy (2014), Continental transforms: A view from the alpine fault, *Journal of Structural Geology*, 64, 3 – 31, doi:10.1016/j.jsg.2014.03.003.
- Ogawa, Y., and Y. Honkura (2004), Mid-crustal electrical conductors and their correlations to seismicity and deformation at Itoigawa-Shizuoka tectonic line, central Japan, *Earth, Planets and Space*, 56(12), 1285–1291, doi:10.1186/BF03353352.
- Ohzono, M., T. Sagiya, K. Hirahara, M. Hashimoto, A. Takeuchi, Y. Hosono, Y. Wada, K. Onoue, F. Ohya, and R. Doke (2011), Strain accumulation process around the atotsugawa fault system in the niigata-kobe tectonic zone, central Japan, *Geophysical Journal International*, 184(3), 977–990, doi:10.1111/j.1365-246X.2010.04876.x.
- Okudaira, T., P. Jeřábek, H. Stünitz, and F. Füsseis (2015), High-temperature fracturing and subsequent grain-size-sensitive creep in lower crustal gabbros: Evidence for coseismic loading followed by creep during decaying stress in the lower crust?, *Journal of Geophysical Research: Solid Earth*, 120(5), 3119–3141, doi:10.1002/2014JB011708.
- Okudaira, T., N. Shigematsu, Y. Harigane, and K. Yoshida (2017), Grain size reduction due to fracturing and subsequent grain-size-sensitive creep in a lower crustal shear zone in the presence of a co₂-bearing fluid, *Journal of Structural Geology*, 95, 171 – 187, doi:10.1016/j.jsg.2016.11.001.

- Oskin, M., L. Perg, E. Shelef, M. Strane, E. Gurney, B. Singer, and X. Zhang (2008), Elevated shear zone loading rate during an earthquake cluster in eastern California, *Geology*, 36(6), 507, doi:10.1130/G24814A.1.
- Pollitz, F. F. (2001), Viscoelastic shear zone model of a strike-slip earthquake cycle, *Journal of Geophysical Research: Solid Earth*, 106(B11), 26,541–26,560, doi:10.1029/2001JB000342.
- Ranalli, G. (1995), *Rheology of the Earth*, Springer Science & Business Media.
- Reid, H. F. (1910), *The mechanisms of the earthquake*, vol. 2, 192 pp., Carnegie Institution of Washington.
- Research Group for Active Faults of Japan (1991), Active faults in Japan: Sheet maps and inventories.
- Rohrer, G. S. (2010), Introduction to grains, phases, and interfaces—an interpretation of microstructure, *Metallurgical and Materials Transactions A*, 41(5), 1063–1100, doi:10.1007/s11661-010-0215-5.
- Rutter, E. (1999), On the relationship between the formation of shear zones and the form of the flow law for rocks undergoing dynamic recrystallization, *Tectonophysics*, 303(1), 147 – 158, doi:10.1016/S0040-1951(98)00261-3.
- Rutter, E., and K. Brodie (2004), Experimental intracrystalline plastic flow in hot-pressed synthetic quartzite prepared from brazilian quartz crystals, *Journal of Structural Geology*, 26(2), 259 – 270, doi:10.1016/S0191-8141(03)00096-8.

- Rybacki, E., M. Gottschalk, R. Wirth, and G. Dresen (2006), Influence of water fugacity and activation volume on the flow properties of fine-grained anorthite aggregates, *Journal of Geophysical Research: Solid Earth*, 111(B3), [doi:10.1029/2005JB003663](https://doi.org/10.1029/2005JB003663).
- Savage, J. C., and R. O. Burford (1973), Geodetic determination of relative plate motion in central California, *Journal of Geophysical Research*, 78(5), 832–845, [doi:10.1029/JB078i005p00832](https://doi.org/10.1029/JB078i005p00832).
- Savage, J. C., and W. H. Prescott (1978), Asthenosphere readjustment and the earthquake cycle, *Journal of Geophysical Research: Solid Earth*, 83(B7), 3369–3376, [doi:10.1029/JB083iB07p03369](https://doi.org/10.1029/JB083iB07p03369).
- Savage, J. C., J. L. Svarc, and W. H. Prescott (1999), Geodetic estimates of fault slip rates in the san francisco bay area, *Journal of Geophysical Research: Solid Earth*, 104(B3), 4995–5002, [doi:10.1029/1998JB900108](https://doi.org/10.1029/1998JB900108).
- Scholz, C. H. (1982), Scaling laws for large earthquakes: consequences for physical models, *Bulletin of the Seismological Society of America*, 72(1), 1–14.
- Sclater, J. G., C. Jaupart, and D. Galson (1980), The heat flow through oceanic and continental crust and the heat loss of the earth, *Reviews of Geophysics*, 18(1), 269–311, [doi:10.1029/RG018i001p00269](https://doi.org/10.1029/RG018i001p00269).
- Shelef, E., and M. Oskin (2010), Deformation processes adjacent to active faults: Examples from eastern California, *Journal of Geophysical Research: Solid Earth*, 115(B5), [doi:10.1029/2009JB006289](https://doi.org/10.1029/2009JB006289).

- Shimada, K., H. Tanaka, T. Toyoshima, T. Obara, and T. Niizato (2004), Occurrence of mylonite zones and pseudotachylyte veins around the base of the upper crust: An example from the southern Hidaka metamorphic belt, Samani area, Hokkaido, Japan, *Earth Planets Space*, 56(12), 1217–1223, doi: [10.1186/BF03353343](https://doi.org/10.1186/BF03353343).
- Sibson, R. (1980), Transient discontinuities in ductile shear zones, *Journal of Structural Geology*, 2(1), 165 – 171, doi:[10.1016/0191-8141\(80\)90047-4](https://doi.org/10.1016/0191-8141(80)90047-4).
- Sibson, R. H. (1982), Fault zone models, heat flow, and the depth distribution of earthquakes in the continental crust of the United States, *Bulletin of the Seismological Society of America*, 72(1), 151–163.
- Smith, B. R., and D. T. Sandwell (2006), A model of the earthquake cycle along the San Andreas fault system for the past 1000 years, *Journal of Geophysical Research: Solid Earth*, 111(B1), doi:[10.1029/2005JB003703](https://doi.org/10.1029/2005JB003703).
- Stern, T., D. Okaya, S. Kleffmann, M. Scherwath, S. Henrys, and F. Davey (2013), Geophysical exploration and dynamics of the alpine fault zone, in *A Continental Plate Boundary: Tectonics at South Island, New Zealand*, pp. 207–233, American Geophysical Union (AGU), doi:[10.1029/175GM11](https://doi.org/10.1029/175GM11).
- Stirling, M. W., S. G. Wesnousky, and K. Shimazaki (1996), Fault trace complexity, cumulative slip, and the shape of the magnitude-frequency distribution for strike-slip faults: a global survey, *Geophysical Journal International*, 124(3), 833–868, doi:[10.1111/j.1365-246X.1996.tb05641.x](https://doi.org/10.1111/j.1365-246X.1996.tb05641.x).

Storti, F., R. E. Holdsworth, and F. Salvini (2003), Intraplate strike-slip deformation belts, *Geological Society, London, Special Publications*, 210(1), 1–14, [doi:10.1144/GSL.SP.2003.210.01.01](https://doi.org/10.1144/GSL.SP.2003.210.01.01).

Takahashi, Y. (2015), Geotectonic evolution of the nihonkoku mylonite zone of north central Japan based on geology, geochemistry, and radiometric ages of the nihonkoku mylonites, *Ductile Shear Zones: From Micro-to Macro-scales*, pp. 270–292, [doi: 10.1002/9781118844953.ch16](https://doi.org/10.1002/9781118844953.ch16).

Takeuchi, C. S., and Y. Fialko (2012), Dynamic models of interseismic deformation and stress transfer from plate motion to continental transform faults, *Journal of Geophysical Research: Solid Earth*, 117(B5), [doi:10.1029/2011JB009056](https://doi.org/10.1029/2011JB009056).

Takeuchi, C. S., and Y. Fialko (2013), On the effects of thermally weakened ductile shear zones on postseismic deformation, *Journal of Geophysical Research: Solid Earth*, 118(12), 6295–6310, [doi:10.1002/2013JB010215](https://doi.org/10.1002/2013JB010215).

Talebian, M., E. J. Fielding, G. J. Funning, M. Ghorashi, J. Jackson, H. Nazari, B. Parsons, K. Priestley, P. A. Rosen, R. Walker, and T. J. Wright (2004), The 2003 bam (iran) earthquake: Rupture of a blind strike-slip fault, *Geophysical Research Letters*, 31(11), [doi:10.1029/2004GL020058](https://doi.org/10.1029/2004GL020058).

Tanaka, A., M. Yamano, Y. Yano, and M. Sasada (2004), Geothermal gradient and heat flow data in and around Japan (i): Appraisal of heat flow from geothermal gradient data, *Earth, Planets and Space*, 56(12), 1191–1194, [doi:10.1186/BF03353339](https://doi.org/10.1186/BF03353339).

- Thatcher, W., and P. C. England (1998), Ductile shear zones beneath strike-slip faults: Implications for the thermomechanics of the San Andreas fault zone, *Journal of Geophysical Research: Solid Earth*, 103(B1), 891–905, doi:10.1029/97JB02274.
- Tullis, J., and R. A. Yund (1982), Grain growth kinetics of quartz and calcite aggregates, *The Journal of Geology*, 90(3), 301–318, doi:10.1086/628681.
- Tullis, J., and R. A. Yund (1985), Dynamic recrystallization of feldspar: A mechanism for ductile shear zone formation, *Geology*, 13(4), 238, doi:10.1130/0091-7613(1985)13<238:DROFAM>2.0.CO;2.
- Tullis, J., and R. A. Yund (1991), Diffusion creep in feldspar aggregates: experimental evidence, *Journal of Structural Geology*, 13(9), 987 – 1000, doi:10.1016/0191-8141(91)90051-J.
- Turcotte, D., and G. Schubert (2014), *Geodynamics*, Cambridge University Press.
- Urai, J. L., W. D. Means, and G. S. Lister (2013), *Dynamic Recrystallization of Minerals*, pp. 161–199, American Geophysical Union (AGU), doi:10.1029/GM036p0161.
- Wallace, R. E. (1970), Earthquake recurrence intervals on the San Andreas fault, *GSA Bulletin*, 81(10), 2875, doi:10.1130/0016-7606(1970)81[2875:ERIOTS]2.0.CO;2.
- White, S. (1979), Grain and sub-grain size variations across a mylonite zone, *Contributions to Mineralogy and Petrology*, 70(2), 193–202, doi: 10.1007/BF00374448.
- White, S., S. Burrows, J. Carreras, N. Shaw, and F. Humphreys (1980), On my-

- lonites in ductile shear zones, *Journal of Structural Geology*, 2(1), 175 – 187, [doi:10.1016/0191-8141\(80\)90048-6](https://doi.org/10.1016/0191-8141(80)90048-6).
- Wilson, C. K., C. H. Jones, P. Molnar, A. F. Sheehan, and O. S. Boyd (2004), Distributed deformation in the lower crust and upper mantle beneath a continental strike-slip fault zone: Marlborough fault system, south island, New Zealand, *Geology*, 32(10), 837, [doi:10.1130/G20657.1](https://doi.org/10.1130/G20657.1).
- Wittlinger, G., P. Tapponnier, G. Poupinet, J. Mei, S. Danian, G. Herquel, and F. Masson (1998), Tomographic evidence for localized lithospheric shear along the altyn tagh fault, *Science*, 282(5386), 74–76, [doi:10.1126/science.282.5386.74](https://doi.org/10.1126/science.282.5386.74).
- Wright, T. J., J. R. Elliott, H. Wang, and I. Ryder (2013), Earthquake cycle deformation and the moho: Implications for the rheology of continental lithosphere, *Tectonophysics*, 609, 504 – 523, [doi:10.1016/j.tecto.2013.07.029](https://doi.org/10.1016/j.tecto.2013.07.029).
- Yamasaki, T., T. J. Wright, and G. A. Houseman (2014), Weak ductile shear zone beneath a major strike-slip fault: Inferences from earthquake cycle model constrained by geodetic observations of the western North Anatolian Fault Zone, *Journal of Geophysical Research: Solid Earth*, 119(4), 3678–3699, [doi:10.1002/2013JB010347](https://doi.org/10.1002/2013JB010347).
- Yoshimura, R., N. Oshiman, M. Uyeshima, H. Toh, T. Uto, H. Kanazaki, Y. Mochido, K. Aizawa, Y. Ogawa, T. Nishitani, S. Sakanaka, M. Mishina, H. Satoh, T. Goto, T. Kasaya, S. Yamaguchi, H. Murakami, T. Mogi, Y. Yamaya, M. Harada, I. Shiozaki, Y. Honkura, S. Koyama, S. Nakao, Y. Wada, and Y. Fujita (2009), Mag-

netotelluric transect across the niigata-kobe tectonic zone, central Japan: A clear correlation between strain accumulation and resistivity structure, *Geophysical Research Letters*, 36(20), doi:10.1029/2009GL040016.

Yuen, D. A., L. Fleitout, G. Schubert, and C. Froidevaux (1978), Shear deformation zones along major transform faults and subducting slabs, *Geophysical Journal of the Royal Astronomical Society*, 54(1), 93–119, doi:10.1111/j.1365-246X.1978.tb06758.x.

Zhang, X., and T. Sagiya (2017), Shear strain concentration mechanism in the lower crust below an intraplate strike-slip fault based on rheological laws of rocks, *Earth, Planets and Space*, 69(1), 82, doi:10.1186/s40623-017-0668-5.

Zhang, X., and T. Sagiya (2018), Intraplate strike-slip faulting, stress accumulation, and shear localization of a crust-upper mantle system with nonlinear viscoelastic material, *Journal of Geophysical Research: Solid Earth*, 123(10), 9269–9285, doi:10.1029/2018JB016421.

Zhu, L. (2000), Crustal structure across the San Andreas fault, southern California from teleseismic converted waves, *Earth and Planetary Science Letters*, 179(1), 183 – 190, doi:10.1016/S0012-821X(00)00101-1.